DRAFT VERSION MARCH 21, 2017
Preprint typeset using LaTeX style emulateapj v. 3/25/03

arXiv:1703.05281v2 [astro-ph.GA] 18 Mar 2017

"Super-deblended" DUST EMISSION IN GALAXIES: I. THE GOODS-NORTH CATALOG AND THE COSMIC STAR FORMATION RATE DENSITY OUT TO REDSHIFT 6

DAIZHONG LIU[1,2,3,4], EMANUELE DADDI[2], MARK DICKINSON[5], FRAZER OWEN[6], MAURILIO PANNELLA[7], MARK SARGENT[8], MATTHIEU BÉTHERMIN[9,10], GEORGIOS MAGDIS[11], YU GAO[1], XINWEN SHU[2,12], TAO WANG[2], SHUOWEN JIN[2], HANAE INAMI[13]

Draft version March 21, 2017

ABSTRACT

We present a new technique to obtain multi-wavelength *"super-deblended"* photometry in highly confused images, that we apply here in the GOODS-North field to *Herschel* and (sub-)millimeter data sets. The key novelties of the method are two: first, starting from a common large prior database of deep 24 μm and VLA 20 cm detections, an *active* selection of *useful* fitting priors is performed independently at each frequency band and moving from less to more confused bands. Exploiting knowledge of redshift and all available photometry for each source up to the dataset under exam, we identify *hopelessly faint* priors that we remove from the fitting pool. This approach critically reduces blending degeneracies and allows reliable photometry of galaxies in FIR+mm bands. Second, we obtain well-behaved *quasi-Gaussian* flux uncertainties, individually tailored to all fitted priors in each band. This is done exploiting extensive simulations calibrating the conversion of formal fitting uncertainties onto real uncertainties, depending on quantities directly measurable in the observations. Our catalog achieves deeper detection limits with high fidelity measurements and uncertainties at far-infrared to millimeter bands. We identify 71 $z \geq 3$ galaxies with reliable FIR+mm detection and study their location in stellar mass–star formation rate diagrams. We present new constraints on the cosmic star formation rate density at $3 < z < 6$ finding significant contribution from $z \geq 3$ dusty galaxies that are missed by optical to near-infrared color selections. The photometric catalog is released publicly (upon acceptance of the paper).

Subject headings: galaxies: photometry — infrared: galaxies — galaxies: star formation — galaxies: ISM — techniques: photometric

1. INTRODUCTION

Infrared (IR) to millimeter (mm) observations toward blank deep fields have been accumulating in the last decade with the *Spitzer Space Telescope* (hereafter *Spitzer*; Werner et al. 2004), *Herschel Space Observatory* (hereafter *Herschel*; Pilbratt et al. 2010) and many ground-based single-dish telescopes (e.g. IRAM 30m and JCMT 15m telescopes). These observations are indispensable for understanding the evolution of star formation and of the interstellar medium of galaxies since early cosmic time to the present. Dust grains, which can be largely produced from the evolution of massive stars in a short time scale (hence a direct product of star formation activity in young star-forming galaxies[14]), absorb the ultraviolet (UV) to optical wavelength stellar light and re-emit the energy as longer wavelength IR photons. A large amount of dust can exist in galaxies with intense star formation activity, making their rest-frame UV-to-optical light substantially attenuated. Hence with UV to optical observations alone, one can directly measure only the unobscured star formation in galaxies. The dust attenuation can be estimated from the UV to optical photometry, for example from the UV continuum slope or the UV to optical spectral energy distribution (SED), but these estimates are still indirect, can have large uncertainties and might miss large SFRs contribution hiding behind optically thick dust. Far-IR (FIR) observations have thus become key tools towards directly measuring obscured star formation rates (SFRs) in galaxies across cosmic time (e.g. Ciesla et al. 2014; Draine et al. 2007; Magdis et al. 2012; Tan et al. 2014).

Spitzer was the first IR space telescope efficient and sensitive enough to survey large areas to depths probing distant galaxies at cosmological redshifts (e.g. Ashby et al. 2013, 2015; Frayer et al. 2006, 2009; Le Floc'h et al. 2005, 2009; Magnelli et al. 2009, 2011). It has the most sensitive instruments over the near-IR 3.6–8.0 μm (The Infrared Array Camera, IRAC; Fazio et al. 2004) and mid-IR 24 μm (The Multiband Imaging Photometer, MIPS; Rieke et al. 2004) domains, but is much less sensitive at 70 and 160 μm than the later IR space telescope *Herschel*.

Herschel has extended the wavelength coverage from 70 μm all the way to 500 μm, and provides more than 4 times better spatial resolution at 70, 100 and 160 μm than that of

[1] Purple Mountain Observatory/Key Laboratory for Radio Astronomy, Chinese Academy of Sciences, No. 2 West Bejing Road, Nanjing, China (dzliu@mpia.de)
[2] CEA Saclay, Laboratoire AIM-CNRS-Université Paris Diderot, IRFU/SAp, Orme des Merisiers, F-91191 Gif-sur-Yvette, France
[3] University of Chinese Academy of Sciences, 19A Yuquan Road, Shijingshan District, 10049, Beijing, China
[4] Max Planck Institute for Astronomy, Königstuhl 17, D-69117 Heidelberg, Germany
[5] National Optical Astronomy Observatory, Tucson, Arizona 85719, USA
[6] National Radio Astronomy Observatory, Socorro, NM 87801, USA
[7] Universitäts-Sternwarte München, Scheinerstr. 1, D-81679, München, Germany
[8] Astronomy Centre, Department of Physics and Astronomy, University of Sussex, Brighton, BN1 9QH, UK
[9] European Southern Observatory, Karl Schwarzschild Strasse 2, 85748, Garching, Germany
[10] Aix Marseille Univ, CNRS, LAM, Laboratoire d'Astrophysique de Marseille, Marseille, France
[11] Dark Cosmology Centre, Niels Bohr Institute, University of Copenhagen, Juliane Mariesvej 30, DK-2100 Copenhagen, Denmark
[12] Anhui Normal University, Wuhu, Anhui, China
[13] Observatoire de Lyon, 9, avenue Charles André, 69561 Saint Genis Laval, France

[14] Dust grains can also be produced from low- and intermediate- mass stars during their Asymptotic Giant Branch (AGB) stage in a longer time scale. e.g. Draine 2003; Gail et al. 2009; Zhukovska & Henning 2013.

Spitzer with its Photoconductor Array Camera and Spectrometer (PACS) photometer (Poglitsch et al. 2010), and also covers longer wavelengths (250, 350 and 500 μm) that had ever been probed before with comparable mapping speed, with its Spectral and Photometric Imaging Receiver (SPIRE) photometer (Griffin et al. 2010). The direct probing of FIR emission of galaxies has been finally made possible by Herschel for a large number of galaxies across cosmological redshifts (e.g. Béthermin et al. 2015; Gruppioni et al. 2013; Lee et al. 2013; Magnelli et al. 2013; Schreiber et al. 2015; Shu et al. 2016; Wang et al. 2016).

However, source confusion problems can introduce substantial biases in photometric works. *Herschel* SPIRE images have 2–3 times larger (20–38″) point spread functions (PSFs) than the PACS images. The flux of individual galaxy is difficult to measure there, because of non-negligible blending from nearby galaxies. If one considers all possible star forming galaxy contributors to the SPIRE signal and try to simultaneously fit for all of them, no individual measurement can be obtained because of degeneracies (the average number of sources per beam is potentially always $\gg 1$). On the other hand the measured flux will be biased either if we simply ignore a fraction of the potential contributing sources in the *prior-extraction* method [15], or if we treat several blended sources as one source (e.g. the *blind-extraction* method [16]). Therefore, a careful approach considering both the preselection of prior sources (in a way that the final density of sources corresponds in all bands to $\lesssim 1$ sources per beam) and the contributions of faint sources, is needed for the photometry in order to obtain high quality scientific results.

Several solutions have already been explored for prior-extraction of galaxy fluxes inside large PSF, confused FIR/mm images. Béthermin et al. (2010b) used MIPS 24 μm catalog (Béthermin et al. 2010a) as the input, and apply their IDL-based FASTPHOT routine with a linear inversion algorithm to perform prior-extraction photometry for the Extended Chandra Deep Field South field. Roseboom et al. (2010) used MIPS 24 μm-detected sources as their prior list for SPIRE photometry with the cross-identification (XID) tool. XID also uses a linear inversion algorithm as its core fitting function and adopts a "top-down" approach to iteratively jackknife the actual prior list at each band so as to achieve a best model fitting. Elbaz et al. (2011) [17] also use MIPS 24 μm-detected ($S/N > 5$) sources for PACS 160 μm and SPIRE 250 μm photometry in GOODS-North and GOODS-South fields, adopting SPIRE 250 μm $S/N > 2$ sources as the prior list for SPIRE 350 and 500 μm photometry. Béthermin et al. (2012, 2015) used MIPS 24 μm sources as priors as well, but have done more detailed selections: they first perform stacking to derive an average relationship between redshift, stacked flux and SPIRE-to-24 μm color (flux ratio), based on which they predict the SPIRE flux for each prior source. A 24 μm source is selected only if it has the highest predicted SPIRE flux within $0.5 \times$ PSF FWHM, while the remaining fainter sources are ignored. Lee et al. (2013) make use not only of MIPS 24 μm but also VLA 1.4 GHz catalog as the prior list for COSMOS SPIRE photometry. They use the XID algorithm and the iterative jackknife approach for the photometry as also done by Roseboom et al. (2010, 2012). Yan et al. (2014) presented careful deblending work toward a few, specific sources. Their approach is using H band prior sources to form different decomposition schemes, and run iteratively to determine a best fitting scheme. Safarzadeh et al. (2015) developed a novel technique based on the Monte Carlo Markov Chain (MCMC) sampling for prior-extraction photometry. They use *Hubble Space Telescope* (HST) H-band sources as position priors, and adopt UV-to-optical SEDs to predict FIR flux (good within $\pm$ 1 dex). But their approach also considers FIR flux from other catalogs for sources brighter than 3 times the confusion limit. Then, all the prior sources are divided into disjoint confusion-groups based on their FIR flux and positions (so as to save computation resource), and the pixels belonging to each confusion-group (usually irregular 2-dimensional shapes) are fitted in a MCMC way so as to obtain the Bayesian probability distribution function (PDF) of each prior source flux. They tested their technique in a simulated PACS 160 μm image. Hurley et al. (2017) developed a similar MCMC-based prior-extraction tool XID$^+$, which can fit all prior sources to obtain the PDF of the flux of each prior source. Then they measured SPIRE flux for COSMOS 24 μm prior sources (tiling full image into diamond 2-dimension shapes to save computation resource). Such algorithm is efficient in obtaining Bayesian PDFs for all prior sources, thus flux uncertainties can be estimated. However, XID$^+$ does not have priori information on FIR flux, thus might still suffer from some limitations: for example in the case that there are high-z sources not in the prior list contributing substantial flux in SPIRE images, or in cases of sources with close spatial positions but lying at different redshifts (the low redshift ones will often not contribute substantially).

From this brief review of earlier photometric works, it appears that one of the most important steps is choosing the most appropriate prior source list for fitting at each PACS, SPIRE and (sub)mm band. The prior source list should not be redundant (should be about or less than one source per beam, see also Dole et al. 2003; Magnelli et al. 2013), while as complete as possible (not to ignore any non-negligible contributing sources to the total flux).

In this paper we develop an highly optimized method for the prior extraction of sources in highly confused images, and apply in particular to *Herschel* PACS, SPIRE and ground-based single-dish images in GOODS-North. Our method includes choosing an appropriate prior source list for the photometry at each band with the assistance of state-of-the-art SED fitting over all mid-infrared (mid-IR) to radio bands. Benefiting from the latest understanding of the evolution of IR galaxy SEDs with redshift, the high quality catalogs of photometric and spectroscopic redshifts, predicting the flux of galaxies in highly blended FIR bands (once fluxes in less blended images are in hand) becomes possible and also reliable as demonstrated also later in the paper. These flux predictions are only used to determine which sources are hopelessly faint and should be excluded (subtracting their very weak expected fluxes from the data before further measurements), and which ones are to be kept for the prior-extraction photometry. We describe the SED fitting in Section 3.1, and the choosing of fitted/excluded prior sources in Section 3.2. Then the prior-extraction photometry is presented in Section 3.3, and a few examples in Section 4. We emphasize again that this SED flux prediction is only used to flag and remove *hopelessly faint* sources, thus not directly constraining the measurement for the reminder of the priors that are performed on the observed

[15] The prior-extraction method adopts a list of prior source positions as the input to the PSF or other model fitting on image data.

[16] The blind-extraction method adopts auto searching algorithms to identify galaxies out of sky background in deep field images.

[17] Their catalogs are published as Elbaz et al. (2013).

data.

In addition, we blindly extract sources from the residual image after each photometry step in each band. These additional sources (when detected) have a high likelihood of being high redshift galaxies that are too faint at near-IR and mid-IR 24 μm and thus are not in our initial prior catalog (although they might also be blends of several low-luminosity lower-z sources, or spurious noise peaks). After extracting the additional sources, we re-run the prior-extraction photometry including them, at each band. The details of the procedure are given in Section 3.4.

Meanwhile, to verify the performance of the photometry and to provide statistically sound estimations of uncertainties, we run Monte-Carlo simulations at each band from 24 μm all the way to 1.16 mm and radio 20 cm. We propose a recipe for correcting formal flux uncertainties for each individual source in each band, based on a number of directly measurable parameters, calibrated by simulations. The details of the relevant procedures are given in Section 5.

We apply these SED fitting, photometry, simulation and corrections to the GOODS-North field (hereafter GOODS-N), which is one of the blank deep fields that have deepest and richest multi-wavelength data sets. We compare our final GOODS-N catalog with several literature catalogs in Section 7.2, finding that the flux measurements are generally consistent, while we have often better deblending performance for individual cases. This work also leads to somewhat deeper detection limit in SPIRE bands. We emphasize though that the main advantage of our work is that uncertainties are well-behaved (quasi-Gaussian) and the measurement strategy is in our opinion nearly ideal (while still manageable and reproducible) and highly optimized. We believe that the approach described in this paper should be portable to other fields, of course while keeping into account the relative depths of the data sets for prior selection and FIR measurements. A future work (Jin, Daddi et al. 2017, in preparation) will present the application of this technique to the 2-square degree COSMOS field.

We present the final sample (including photometry measurements, uncertainties, and IR SED photometric redshifts) of GOODS-N $z \geq 2.5$ FIR-to-mm (FIR+mm) detected galaxies in Section 8. We derive the dust and star formation properties from SEDs for this deepest FIR+mm high-z sample, and constrain the cosmic star formation rate (SFR) density (CSFRD) up to redshift 6 in Section 8.5 from directly observed galaxies. Using stellar mass functions (SMFs) from the literature, and assuming the star-forming main-sequence (MS; e.g. Daddi et al. 2007; Elbaz et al. 2007; Karim et al. 2011; Noeske et al. 2007; Pannella et al. 2009; Rodighiero et al. 2010) correlations at each redshift, we estimated completeness correction to the SFR densities. Although the FIR+mm high-z ($z > 3$) samples have a high incompleteness in stellar mass, they already appear to contribute a substantial fraction to the total SFR, sometimes even exceeding the empirical SFR when binning by stellar mass. We further compare rest-frame UV (obs-frame optical to near-infrared) color selections with our sample and discuss how optical to near-infrared studies could miss the dusty galaxies in this work.

Our imaging data sets are obtained from various surveys: MIPS 24 μm data are from the GOODS-*Spitzer* program (PI: M. Dickinson), PACS data are the coadded data (Magnelli et al. 2013) of PEP program (PI: D. Lutz) and GOODS-*Herschel* program (PI: D. Elbaz; which is deeper than PEP), and SPIRE data are from the GOODS-*Herschel* program. Our SCUBA-2 data are from the S2CLS program (Cowie et al. 2017; Geach et al. 2017), and AzTEC+MAMBO coadded data from Penner et al. (2011). Our deep radio imaging is from Owen (2017). Appendix A contains the details. In Appendix C, we present the overall flow chart of our methodology, and the detailed performance figures of the simulation-based correction recipes at all bands.

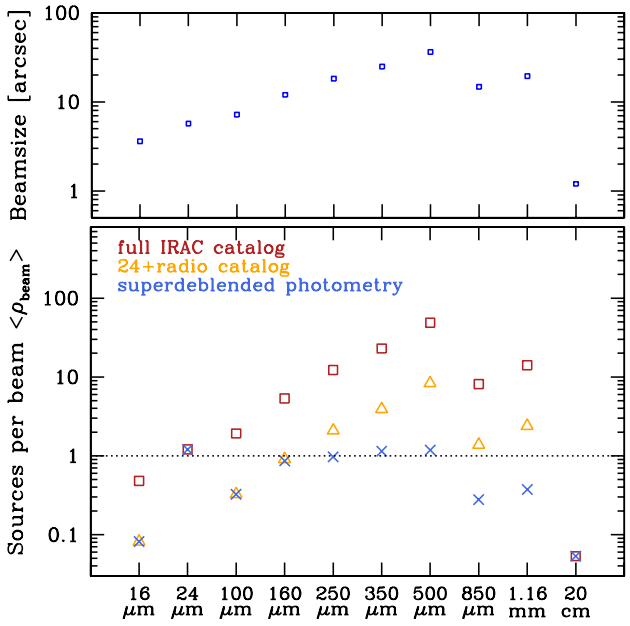

FIG. 1.—: The lower panel shows how our prior source selection as described in Section 3 can reduce the number of sources per beam $\langle\rho_{\rm beam}\rangle$ to about 1 at FIR and mm bands, yielding a balance between source confusion and detection depth. The source densities of the full IRAC catalog are shown as the red squares, the 24 μm- and radio-detected sources are orange triangles, while the *"super-deblended"* prior sources that we selected and actually fitted are blue crosses. We compute the source density by $\langle\rho_{\rm beam}\rangle \equiv N_{prior}/A_{\rm GOODS-N} \times \left(\pi/(4\ln 2) \times \theta^2_{\rm beam}\right)$, where N_{prior} is the number of prior sources in GOODS-N, $A_{\rm GOODS-N}$ is the GOODS-N area ($10.0 \times 16.5\,{\rm arcmin}^2$) and $\theta_{\rm beam}$ is the beamsize (FWHM). The upper panel shows the beamsizes of the GOODS-N image data (Table 1).

We adopt $H_0 = 73$, $\Omega_M = 0.27$, $\Lambda_0 = 0.73$, and a Chabrier IMF (Chabrier 2003) unless specified in text for specific comparisons to other works. We add a constant of -0.04 dex to quantities in logarithm space with Kroupa IMF (Kroupa 2002) to convert into Chabrier IMF, and -0.238 dex to quantities in Salpeter IMF (Salpeter 1955).

2. SETTING THE GENERAL PRIOR SOURCE LIST

In this section we describe how we set up a prior source list that has enough data points to include, in principle, all possible contributors to the flux in FIR to (sub)mm images that we aim to analyze further. Experience has shown that virtually all distant star forming galaxies with detectable IR emission have a counterpart in IRAC images. This is the natural outcome of the close connection between stellar mass and star formation, i.e. the Main Sequence paradigm, coupled with the effective depth of *Spitzer* IRAC imaging in GOODS. We therefore start

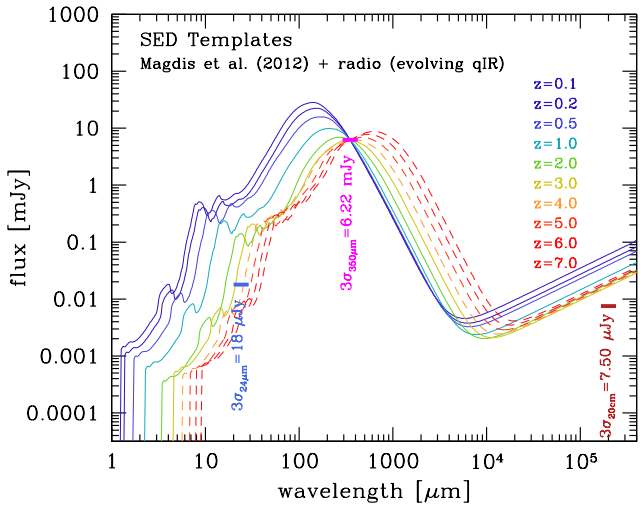

FIG. 2.—: In order to exemplify prior completeness and depth issues, we show SED templates from the Magdis et al. (2012) library (see Section 3.1; color coded by their redshifts) shifted to different redshifts, which have been normalized to the $3\,\sigma$ detection limit at $350\,\mu$m we derive in our analysis: $f_{350\,\mu\rm m} = 6.22$ mJy (see Table 1). Comparing to the prior selection depth ($3\,\sigma$ detection limits at 24 μm, 350 μm and radio 20 cm are indicated by the vertical text and the short solid bar from left to right respectively) it appears that our prior catalog provides a complete list of priors (24 μm and radio sources) required to fit all 350 μm galaxies at z<2-3 (arguably largely independently of their detailed SED shape) , but we are just barely sensitive enough in the radio to include appropriate priors all the way to $z\sim$3–6, where we could have in principle some incompleteness for the faintest SPIRE sources.

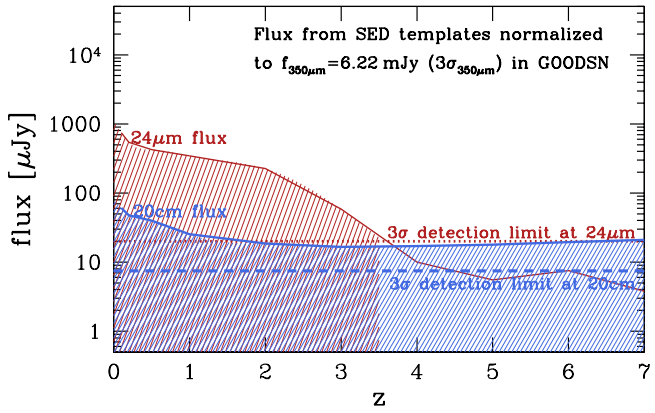

FIG. 3.—: Equivalent to Fig. 2, but showing here the flux expected at 24 μm (red) and 20 cm (blue). The shaded region indicates the redshift range in which 24 μm or 20 cm can be detected, i.e. the flux is above the detection limit. The flux at 24 μm fluctuates somewhat with increasing redshift, which is mainly caused by rest-frame mid-infrared features (e.g. the Polycyclic Aromatic Hydrocarbons; PAHs), while getting below detection threshold for our templates at $z > 3.5$ (adding a stellar component could slightly improve its performance). The flux at 20 cm slowly decreases with redshift and then becomes flat, and is in principle always detectable for these SPIRE-normalized SED templates that assume the FIR-radio correlation.

with a list of IRAC detected galaxies. Most of these galaxies are nevertheless going to be very faint in FIR+mm bands, and we define our general prior list as the subset of them that are detected in either 24 μm or 20 cm images, as described below.

The IRAC catalog from the GOODS-*Spitzer* project (PI: M. Dickinson) contains 19437 sources detected in deep IRAC 3.6 and 4.5 μm images. We cross-matched the optical/near-IR catalogs from Pannella et al. (2015) and 3D-HST project (PI: G. Brammer, Skelton et al. 2014) to associate to each IRAC source a K_s-band flux[18], stellar mass and optical/near-IR photometric redshift[19]. Of the IRAC sources, 16862 have photometric redshifts and stellar masses. We have also cross-matched spectroscopic redshift catalogs from the literature (e.g. Barger et al. 2002, 2008; Casey et al. 2012a; Cohen et al. 2000; Kriek et al. 2015; Reddy et al. 2006; Wirth et al. 2015, etc.) and include some private redshifts from our team (Inami et al. in prep.). 16.2% of the IRAC sources have secure spectroscopic redshifts.

In Fig. 1, we present the mean prior source number per PSF beam area $\langle\rho_{\rm beam}\rangle$ for the catalogs used in this work. The IRAC catalog, represented by brown squares, is clearly too crowded to be used in its entirety for PSF fitting at PACS and SPIRE bands, resulting in a $\langle\rho_{\rm beam}\rangle$ reaching over 10 and approaching 100, making deblending virtually impossible. We note in passing that the drop in prior density (which is larger than the drop in beam size) from SPIRE to (sub)mm is due to the fact that 850 μm and 1.16 mm images are effectively less deeper than SPIRE for typical redshift of the priors. However, $\langle\rho_{\rm beam}\rangle$ is low enough $\lesssim 1$ for 16 μm, 24 μm and 20 cm, so that we can proceed directly to fitting these bands as detailed below.

We do not attempt distinguishing passive versus star forming sources (e.g., using UVJ colors) among IRAC detections, given that passive sources that could be discarded in this way represent only a small fraction of order 10-15%, so that we could erroneously miss some emitting source in trade for a fairly small benefit.

2.1. *PSF fitting methodology*

In this paper we run PSF fitting photometry with the *galfit* (Peng et al. 2002, 2010) software. We use PSF fitting (neglecting the intrinsic size of the emitting sources) given that the highest spatial resolution[20] of the IR images is that of Spitzer 24 μm and 16 μm of 4–6″, a scale at which the intrinsic sizes of most distant galaxies can be neglected (this might not be true for some low-z sources in the images, which are not the main focus of our efforts).

Since it is not practical to use *galfit* to simultaneously fit a large number of prior sources in a large image, our code will first divide the image under examination into small regions (boxes). When fitting prior sources in each box we also consider prior sources from a buffer region of surrounding boxes to avoid edge effects. The buffer size is at least 2–3×

[18] Based on CFHT WIRCAM K_s-band data, see Pannella et al. (2015). We cross-matched with 1″ separation limit.

[19] We obtain in the following additional redshift constraints from IR SED fitting.

[20] The PSF of the VLA data is 2″ and whenever possible we use flux measurements from Owen (2017) that carefully account for possible extended emission, see next sections.

the PSF FHWM of the image. We run *galfit* PSF fitting in each box and then combine all boxes to make the full source model images and residual images. All our PSF fitting is performed at fixed RA-DEC positions as determined from the IRAC catalog, after checking and correcting astrometric differences with each data set under consideration. However, for improving the fitting of bright sources, we perform a second-pass fit (using first-pass results as first guesses) allowing high S/N (e.g. $\gtrsim 10$) sources to vary their positions. This second-pass exercise also allows us to evaluate the extra photometric noise (and possible flux biases) introduced by residual (non corrected) astrometric distortions between IRAC and the examined dataset. These terms are generally small but we correct for them in the analysis.

2.2. *Photometry at MIPS 24 μm*

We fit simple PSFs at 24 μm rather than extended source models because the PSF at this band is about 5.7″, much larger than the typical sizes of $z \geq 0.2$ star-forming galaxies, which are $\sim$8 kpc or 2.5″ at $z = 0.2$ (e.g., Conselice 2014). For lower redshift galaxies in the image, we caution that this approach will lead to underestimated flux measurements, for example, ID 11828, which is the largest spiral galaxy at $z_{spec} = 0.106$ in GOODS-N, and 30 more $z < 0.2$ FIR-to-mm detected galaxies in our final catalog. To properly remove the background in the 24 μm image, we run a first-pass PSF fitting and run a 30×30-pixel median smoothing to the residual image, then subtract the smoothed background image from the original image. We run a second-pass PSF fitting with fixed prior source positions, and a third-pass PSF fitting with varied prior source positions for those high S/N sources in the second-pass fitting. Then we obtain the 24 μm fluxes and formal *galfit* errors.

2.3. *Photometry at VLA 20cm*

The GOODS-N field has very deep VLA $\sim$20 cm observations[21] from Owen (2017) and shallower observations from Morrison et al. (2010). The Morrison et al. (2010) catalog covers more than twice large rectangle area than the circular area covered by the Owen (2017) catalog. In this work, we use the radio data sets for two key purposes: completing the list of prior sources at high redshifts, where galaxies might become too faint to be detected at 24 μm, and as useful constraint for the overall IR luminosity of each prior source based on the FIR-radio correlation.

The importance of including radio prior sources is illustrated in Fig. 2, where we present a series of redshifted SEDs based on the SED templates that we used in this work (see Section 3.1). All SEDs in the figure are normalized to a common $f_{350\,\mu\mathrm{m}} = 6.22\,mJy$, which is the $3\,\sigma_{350\,\mu\mathrm{m}}$ detection limit derived from our simulation (see the following sections). Normalizing to other SPIRE bands will lead to a similar conclusion: the expected $f_{20\,\mathrm{cm}}$ flux is always somewhat higher than the empirical detection limit at 20 cm ($3\,\sigma_{20\,\mathrm{cm}} \approx 7.5\,\mu$Jy) whereas we do not expect to detect the faintest SPIRE sources at 24 μm for $z \gtrsim 3$. This is also illustrated in Fig. 3, where we plot the predicted flux at 24 μm and 20 cm as a function of redshift, for the same normalization at 350 μm. The radio data are clearly effectively deeper than the MIPS 24 μm data in selecting sources at $z \gtrsim 3$, by roughly a factor of $\gtrsim 4$ (being twice brighter than our limit at any redshift, while 24 μm is twice fainter). Therefore, by including the VLA 20 cm data from Morrison et al. (2010) and Owen (2017), we can have a more complete prior source catalog especially for $z \gtrsim 3$ sources, improving our completeness for fitting PACS and SPIRE photometry, and also in the (sub)mm.

We use the radio catalog from Owen (2017) as the main source of 20cm photometry in this study, presenting detections down to a $5\,\sigma$ level of significance. Owen (2017) carefully derived best estimates for the fluxes, accounting for possible spatial extension of the sources by comparing fluxes in radio images of different resolution from 1″ to 3″. In order to match our prior catalog with IRAC-based positions to the radio we adopt the same matching scheme of Owen 2017 (their Eq. 1), with a tolerance depending on the radio S/N and size of the sources, and including also a 0.2″ term in quadrature to account for typical IRAC astrometry accuracy.

In order to supply a radio measurement for sources weaker than the $5\,\sigma$ detection limit (and/or upper limit) we also performed prior-extraction photometry and Monte-Carlo simulations independently on the imaging data of both Morrison+ and Owen+. Small astrometric misalignments between the two images and IRAC catalog have been corrected in our photometry by adjusting the prior source positions. We first run *galfit* to fit PSF models at fixed positions, then we run *galfit* again allowing high S/N source positions to vary by a small amount (maximum offset less than 1 pixel). We fit on the images without primary beam correction, then calculate the primary beam correction according to each prior source position and apply it to each photometry measurement [22].

Note that the PSF of Owen's radio image is about $\sim$2″ (provided by F. Owen especially for this work), and $\sim$1.7″ for Morrison's radio image. So some sources might be resolved by the beam, more typically at low redshift. In order to verify the performance of our photometry we compare the measurements derived with our procedure to the objects listed in the Owen 2017 catalog. We find that there is a good agreement in general: the median of the ratio between the different measurements is very close to 1, while the semi-interquartile range is about 6% for bright sources above 80 μJy, and reaching 10% for fainter fluxes down to the $5\,\sigma$ limit. This includes effects of flux losses due to over-resolution of the sources, and is accurate enough for a statistical use of the fluxes from our procedure below the $5\,\sigma$ limit, despite its simplicity in assuming a non-resolved emission and fitting at fixed positions.

As a results of these measurements, we find 1334 IRAC sources with $\mathrm{S/N}_{20\,\mathrm{cm}} > 3$ (554 from the Owen 2017 catalog), and 112 of which are not detected with S/N of 3 at MIPS 24 μm. The 24 μm undetected radio sources could be either lower-z radio-loud Active Galactic Nuclei (AGNs), moderate redshift (e.g. $z \sim$1.5) galaxies with strong rest-frame 9.7 μm Silicate absorption feature (e.g. Magdis et al. 2011) or higher-z star-forming galaxies. In Fig. 4, we plot the histogram of the photometric redshift of these sources. Indeed two peaks can be found, and the $z \sim 3$ peak likely represents the high-z star-forming galaxies missed by the MIPS 24 μm selection. We also note that lowering the radio S/N threshold to 2.5 for the high-z (e.g. $z > 2$ in the figure) IRAC sources will almost double their number, while making the gap at $z \sim 2$ shallower

[21] The VLA data from Owen (2017) were obtained with an average frequency of 1.525 GHz, higher than that of Morrison et al. (2010) of 1.4 GHz. We convert to 1.4 GHz assuming a canonical radio slope of -0.8 for the comparison and analysis. (Although we note that a radio slope of -0.8 is not applicable to all sources, e.g. Kimball & Ivezić 2008; Marvil et al. 2015)

[22] We used the primary beam correction equations on https://www.cv.nrao.edu/vla/hhg2vla/node41.html. Most of our correction factors are below ×1.5.

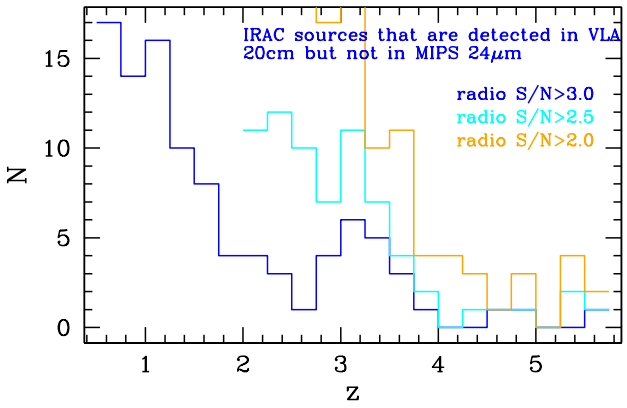

FIG. 4.—: Histogram of the optical/near-infrared photometric redshift of the initial IRAC catalog sources that are detected in VLA 20 cm but not in MIPS 24 μm (with 24 μm S/N <3). These sources could be either lower-z radio-loud AGNs, or high-z ($z \sim 3$) dusty galaxies (See Section 2.3). The blue histogram is 20 cm S/N > 3, while cyan and yellow histograms show the effects of lowering 20 cm S/N to 2.5 and 2.0 respectively for $z > 2$ sources.

(indicated by the cyan histogram). Thus in the next section we use 2.5 as the radio S/N threshold for $z > 2$ sources.

2.4. *The 24+radio prior source catalog*

By combining detections at 24 μm and 20 cm we produce our 24+radio based prior source catalog, which will be used for the analysis in the next steps: SED fitting (Section 3.1) and photometry over the FIR-mm bands. There are 2983 sources in the IRAC catalog with $S/N_{24\,\mu m} \geq 3$, and in addition there are 112 sources with $S/N_{24\,\mu m} < 3$ but with $S/N_{20\,cm} \geq 3$.

For improving coverage of potential high-z prior sources in PACS, SPIRE and mm images, which could contribute more to these long wavelengths due their redshifted SED peak, we also include lower S/N sources (down to S/N= 2.5) with photometric redshift above 2.0 into the 24+radio prior source list. In this way, we selected 3306 sources in the 24+radio prior source catalog, with these criteria: $S/N_{24\,\mu m} \geq 3$, or $S/N_{20\,cm} \geq 3$, or $S/N_{24\,\mu m} \geq 2.5$ when $z_{phot} > 2.0$, or $S/N_{20\,cm} \geq 2.5$ when $z_{phot} > 2.0$. For the 24+radio selected catalog (3306 in total), the fraction of spectroscopic redshift sources is 47.9% (but only 4.66% for $z > 2$).

Although the flux error measurements at 24 μm and radio are fairly close to Gaussian (see next Sections and the Appendixes), starting from a large number of 19437 IRAC sources would inevitably result in a number of noise-dominated spurious detections. We expect a total of ~ 50 spurious above $3\,\sigma$ combining the two bands. Given that only ~ 4000 IRAC priors have $z_{phot} > 2$, they would also produce some additional ~ 50 spurious sources at $z_{phot} > 2$ and above $2.5\,\sigma$. These ≈ 100 objects would get included among our 3306 priors spuriously, lacking any actual 24 μm or radio detections. This is a small enough number not to affect adversely the detectability of IR galaxies, as the resulting increase of galaxy priors sky densities is small at all bands. In most cases we expect these spurious priors just to remain undetected following the IR analysis.

For the remaining 16131 IRAC sources not included in our prior list, we assume that their flux contribution to the PACS, SPIRE and mm image data are negligible and do not consider them in the rest of this work. Even though their flux won't be exactly zero, their presence will act as a background whose average level will be accounted consistently by our procedure, while their possibly inhomogeneous distribution will act as additional confusion noise, which will also be accounted for by our procedure.

Figures 2 and 3 suggest that our prior source list is fairly complete and will include in principle any FIR-mm detectable star-forming galaxy, even at the highest redshifts thanks notably to our 20 cm detection limit. This of course is no longer true when the scatter in the FIR-radio correlation, SED shape variations and the effect of noise in the data are considered. Despite using the deepest 24 μm and radio catalogs, we do expect some incompleteness in our prior list for $z > 3$ galaxies at the faintest (but detectable) flux levels, especially over the SPIRE bands and in the (sub)mm. This motivates *a posteriori* addition of sources found in the residual map (mainly) in these bands, as discussed later (Section 3.4).

The combined use of 24 μm and radio is also useful to overcome limitations at 24 μm where we fit all IRAC priors with a density of about 1 source per beam. This will imply that our catalog effective depth at 24 μm will depend on local crowding (see further discussions about *crowdedness* in the paper). However, the beam at 20cm is small enough that crowding is irrelevant. Using the radio should prevent the possibility that we are missing useful priors in regions where 24 μm is most crowded.

A more sophisticated way to complete the prior sample for high-z would be to cull more sources in the IRAC catalog and using stellar mass and SFR-mass correlation to single out appropriate additional high-z priors. We have preliminarily investigated this idea in GOODS-N, finding that this does not provide an obvious improvement to what has been achieved in this work. The stellar mass selection will be explored in more detail in future work in COSMOS (Jin, Daddi et al. in preparation) where primary prior catalogs at 24 μm and radio are shallower than here in GOODS-N, and this work will provide a good comparison.

2.5. *Photometry at 16 μm*

Despite its fairly good PSF ($\sim 4.5''$; hence low number of IRAC sources per beam), the GOODS-N 16 μm imaging data observed by the *Spitzer* IRS Peak-Up Imaging (PUI) are much shallower than the MIPS 24 μm image data, therefore in this work we directly fit the 16 μm image data at all 24+radio prior positions to obtain their 16 μm photometry. Only 40% of our 3306 24+radio prior sources have $S/N_{16\,\mu m} \geq 3$.

3. *"Super-deblended"* PHOTOMETRY FOR BLENDED FIR/MM IMAGES

In this section we describe the core of our photometric method to obtain *"super-deblended"* photometry in confused FIR/mm images.

We proceed one band at a time: for example, at this stage, we have obtained 16 μm, 24 μm and 20 cm coverage for the 3306 24+radio sources in our full prior list derived from a parent IRAC catalog. We use this information to optimize photometry in the next band, PACS 100 μm, and continue similarly for other bands once also PACS 100 μm is in hand.

We use SED fitting of all available photometry at each stage to predict the flux at the next FIR/mm band, with the aim of optimizing the pool of prior sources to be fitted at each FIR/mm band. Once we have predicted fluxes and uncertainties for all sources in a given band, we decide a criterion to distinguish faint sources (whose fluxes are then subtracted from the original images), from those that are retained and eventually used as prior positions for flux measurement by PSF fitting.

Finally, we inspect the residual images to perform blind extraction of sources that might still be present in them. We later provide (in following sections) a detailed example of the procedure for galaxies in the area of GN20 (Daddi et al. 2009), and some comparison of our measurements to published catalogs.

Note that we have applied a factor of 1.12× to the final PACS fluxes and uncertainties to account for the flux losses from the high-pass filtering processing of PACS images (e.g. Magnelli et al. 2013; Popesso et al. 2012).

3.1. *SED Fitting Algorithm*

We consider four distinct components in our SED fitting (from shorter to longer wavelengths): 1) a stellar component from Bruzual & Charlot (2003, hereafter BC03) with Small Magellanic Cloud (SMC) attenuation law; 2) a mid-infrared AGN torus component from Mullaney et al. (2011); 3) dust continuum emission as described in the Magdis et al. (2012) library; and 4) a power-law radio component (see text below).

The Magdis et al. (2012) library is based on Draine & Li (2007) (hereafter DL07) templates fitted to the average SEDs of MS and SB galaxies as a function of redshifts. DL07 templates are parametrized by a number of physical properties: the minimum interstellar radiation field (ISRF) intensity $U_{\rm min}$, the maximum ISRF intensity $U_{\rm max}$, the dust mass $M_{\rm dust}$, the mass fraction of PAH to total dust mass $q_{\rm PAH}$, and the mass fraction of dust grains located in Photo-Dissociation Regions (PDR) γ, etc., hence they provide quite wide ranges of SED shapes. However, Magdis et al. (2012) simplified the parametrization of DL07 templates for galaxies at various redshifts with only two parameters: the IR luminosity per dust mass $L_{\rm IR}/M_{\rm dust}$ or the mean ISRF intensity $\langle U\rangle$[23], and whether the source is on the MS or not. Magdis et al. (2012) find that the shapes of the dust SEDs of MS galaxies at a given redshift, as traced by $L_{\rm IR}/M_{\rm dust}$, is not expected to vary significantly with increasing $L_{\rm IR}$ or SFR. Meanwhile at different redshifts, $L_{\rm IR}/M_{\rm dust}$ changes as a function of z, therefore the changing of SED shape among MS galaxies is expected to be only dependent on $L_{\rm IR}/M_{\rm dust}$ or $\langle U\rangle$. Magdis et al. (2012) constructed a series of dust SED templates for MS galaxies only parametrized by $\langle U\rangle$, as shown in their Fig. 16. These templates assumed an evolution of $\langle U\rangle \propto (1+z)^{1.15}$, no evolution in PDR fraction and a small evolution of $q_{\rm PAH}$ beyond $z=2$ as indicated by their data. Béthermin et al. (2015) updated the evolution of $\langle U\rangle \propto (1+z)^{1.8}$ with latest data in the COSMOS field. Therefore, in this work, we use the Magdis et al. (2012) dust SED templates (which is depending on $\langle U\rangle$) with Béthermin et al. (2015) redshift evolution (determining $\langle U\rangle$ at each redshift) to fit galaxy SEDs and predict photometric redshift and FIR/mm fluxes. Examples of our SED templates are shown in Fig. 2.

Meanwhile, there is a small fraction of galaxies at all redshifts with SFRs above MS, which are known as starburst (SB) galaxies. Their $L_{\rm IR}/M_{\rm dust}$ ratio or $\langle U\rangle$ is found to be higher than MS galaxies (at least at $z<1.5$) and likely does not vary with redshift (Béthermin et al. 2015; Magdis et al. 2012; Tan et al. 2014). So their SEDs can be also parametrized in the same way, by a constant $\langle U\rangle$. When fitting MS galaxies at a given redshift we allow for a range of $\langle U\rangle$ values spanning ±0.2dex around the expected value, to allow for the observed scatter of dust temperature among MS galaxies (defined by $z=0$ results, see Magdis et al. 2012).

A power-law radio SED has been added to describe the radio continuum as ($S_\nu \propto \nu^{-0.8}$)[24] and tied to $L_{\rm IR}$ by the FIR-radio logarithmic ratio $q_{\rm IR} \equiv \log_{10}(S_{\rm IR,8-1000\,\mu m}/3.75\times 10^{12}\,{\rm W\,m^{-2}}) - \log_{10}(S_{1.4\,\rm GHz}/{\rm W\,m^{-2}\,Hz^{-1}})$ (e.g. Condon 1992; Helou et al. 1985; Ivison et al. 2010; Sargent et al. 2010; Tan et al. 2014), so that the radio data point can be used in the fit together with FIR/mm to constrain $L_{\rm IR}$. Here we adopt the latest results in the field that suggest a slowly evolving $q_{\rm IR} = 2.35\times(1+z)^{-0.12} + \log(1.91)$, following Magnelli et al. (2015)[25] and Delhaize et al. (2017, in prep.). We find that such small evolution is also generally warranted by our global SEDs. We verified that adopting a constant $q_{\rm IR}$ would have negligible impact on the entire photometric analysis carried out in this paper.

3.1.1. *SED fitting parameters*

In the case of radio-excess sources or radio-loud AGNs, which are outliers of the FIR-radio correlation, the radio emission does not predominantly arise from star formation. In these cases their radio photometry should not be used in SED fitting. For this and other analogous situations in the following we introduce three parameters which summarize the SED fitting approach and which are included in our final catalog: 1) a flag to distinguish between MS and SB galaxies, 2) a flag to identify radio-excess, and 3) a flag for high-quality FIR photometry (in which case radio fluxes are not used in the SED fit).

The first parameter is the MS/SB classification (noted as "*Type_SED*"), corresponding to the use of MS/SB types of SED templates. It is determined by running SED fitting twice (as we need a first estimate of SFR to decide if the galaxy is MS or SB). In the first run, we fit all SED templates for each source. We fit model grids and obtain the χ^2 distributions, then derive the best fitting values and uncertainties for $z_{\rm phot}$, $\langle U\rangle$, $M_{\rm dust}$ and $L_{\rm IR}$, based on the equations in Avni (1976); Avni et al. (1980); Lampton et al. (1976); Press et al. (1992). SFRs are computed from the integrated $L_{\rm IR}$ by assuming a Chabrier IMF (Chabrier 2003), which is ${\rm SFR} = L_{\rm IR}/\left(1\times10^{10}L_\odot\right)\,{\rm M_\odot\,yr^{-1}}$ (Daddi et al. 2010). We then compare the SFR and its uncertainty $\sigma_{\rm SFR}$ with the MS-based SFR ($\rm SFR_{MS}$) according to Eq. (A1) of Sargent et al. (2014): $\rm SFR_{MS} = M_*\times N(M_*)\times\exp\left(\frac{A\cdot z}{1+B\cdot z^C}\right)$, where the redshift z is from SED fitting and the stellar mass M_* is from Pannella et al. (2015) as described in Section 2 when available. Sources are set to pure SB (*Type_SED* = 1) if

[23] $\langle U\rangle$ is proportional to $L_{\rm IR}/M_{\rm dust}$.

[24] We choose a slope of -0.8 in this work, e.g. Kellermann & Owen 1988; Kimball & Ivezić 2008. But we also note that a single slope can not apply to each galaxy, e.g. Marvil et al. 2015. Since we use radio data mainly for optimizing the fitted prior sources at FIR/mm band, then focus on the FIR/mm properties of the sources, we do not implement a galaxy-dependent radio slope for the SED fitting.

[25] log(1.91) accounts for the conversion between FIR (rest-frame 42 to 122 μm) and IR (rest-frame 8 to 1000 μm) according to Magnelli et al. (2015).

$\log(\mathrm{SFR}/\mathrm{SFR_{MS}}) > 0.6$ dex and $\mathrm{SFR}/\sigma_{\mathrm{SFR}} > 3$, and to pure MS (*Type_SED* $= -1$) if $\log(\mathrm{SFR}/\mathrm{SFR_{MS}}) < 0.4$ dex and $\mathrm{SFR}/\sigma_{\mathrm{SFR}} > 3$. For all other sources, e.g., those without M* estimate or those for which the SFR does not meet the criteria above, we set *Type_SED* $= 0$ and fit all MS+SB templates to their SEDs without distinguishing MS or SB templates.

The second parameter is the classification of radio-excess sources or radio-loud AGNs (noted as "*Type_20cm*"). It is also determined using a two-pass SED fitting approach. In the first-pass, we do not use the observed radio data point ($f_{\mathrm{OBS,radio}}$). Since the radio SED component is tied to the L_{IR} by the FIR-radio correlation, we can derive an expected radio flux and associated uncertainty from the IR SED fit. Then, the (dis)agreement between the observed radio flux and the flux predicted from the best-fit IR SED determines our choice of the parameter *Type_20cm*: if $(f_{\mathrm{OBS,radio}} - f_{\mathrm{SED,radio}})/\sqrt{\sigma^2_{\mathrm{OBS,radio}} + \sigma^2_{\mathrm{SED,radio}}} > 3$ and $f_{\mathrm{OBS,radio}} > 2\times f_{\mathrm{SED,radio}}$, then we set *Type_20cm* $= 1$, otherwise *Type_20cm* $= 0$. Then, in the second-pass SED fitting, if a source has *Type_20cm* $= 1$, we do not use its radio data, while for the remaining sources we use the radio data to provide tighter constraints on the physical properties. Overall, we have flagged 10.3% of the 24+radio source as radio-excess/radio-loud candidates. Notice that our approach is very conservative in flagging a source as a possible radio AGN when both the bolometric L_{IR} and radio are well measured and the radio exceeds by two times the expected value based on the bolometric IR, which is comparable to the scatter of the radio-IR correlation. Some of these sources will not actually be AGNs but we refrain using their radio fluxes for SED fitting, as soon as we have a well determined IR SED.

The third parameter is the combined S/N over FIR/mm bands (noted as "*Type_FIR*"). For sources with FIR/mm combined S/N ≥ 5 [26], we set *Type_FIR* $= 1$ and do not fit the 24 μm and radio data points anymore. In this way our SED fitting procedure will not be affected by the scatter of the FIR-radio relation, or by galaxy-galaxy variations of the mid-IR dust SED features (e.g. variations of the IR to rest-frame 8 μm ratio, IR8, Elbaz et al. 2011). This optimization improves the FIR/mm part SED fitting of individual sources, but does not lead to obvious difference in the statistical results in Section 8.

As briefly mentioned already, the SED fitting is (re)run for each FIR/mm band, prior to extracting photometry for the band. For example, before we measure PACS 100 μm fluxes, we run SED fitting with K_s, IRAC, 16 μm, 24 μm, and 20 cm (if not radio-excess or radio-loud) data points for each 24+radio prior source. Similarly, prior to extracting SPIRE 350 μm photometry, we run SED fitting with the aforementioned bands, plus the newly measured 100 μm, 160 μm and 250 μm data points. The purpose of this SED fitting is to provide the best possible prediction for choosing actual prior sources for fitting, a crucial step towards obtaining *"super-deblended"* photometry.

For sources which have optical/near-IR photometric redshifts we perform SED fitting allowing the redshift to span a range of $\pm 10\%$ in $(1+z)$, corresponding to about ± 2-σ range

[26] For example at 350 μm, we calculate the combined S/N from 100 μm to 250 μm as $\sqrt{\mathrm{S/N}^2_{100\,\mu\mathrm{m}} + \mathrm{S/N}^2_{160\,\mu\mathrm{m}} + \mathrm{S/N}^2_{250\,\mu\mathrm{m}}}$, and similarly at other bands.

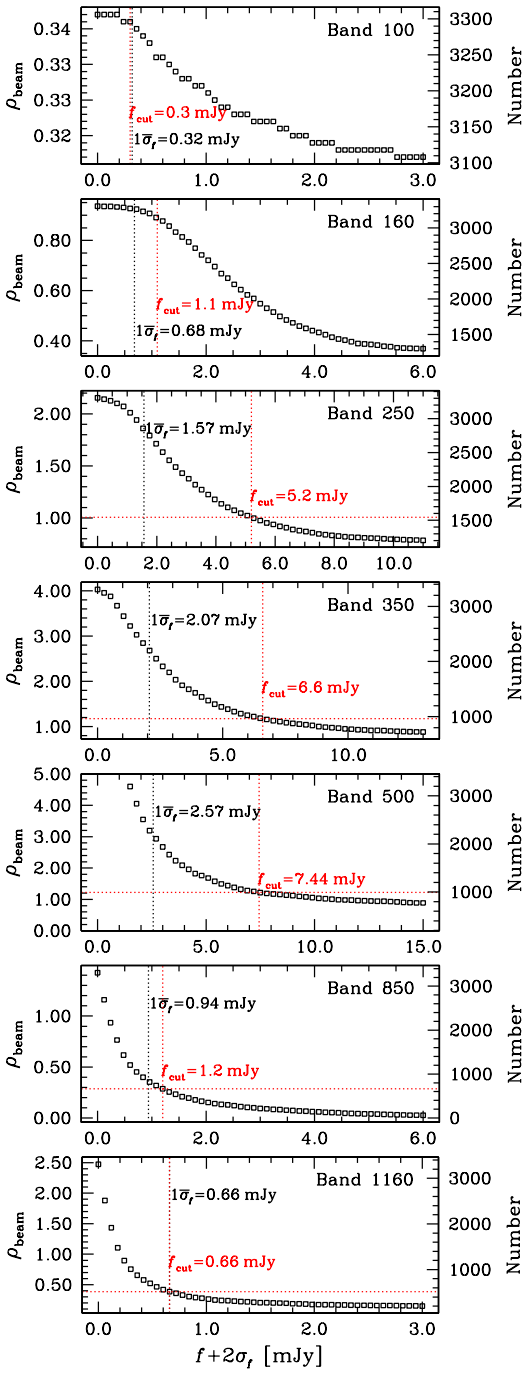

FIG. 5.—: The cumulative number density ρ_{beam} of prior sources versus their expected flux, *conservatively* augmented by twice the flux uncertainty. We select for *galfit* PSF fitting photometry sources with fluxes larger than some cutting value: $f_{\mathrm{SED}} + 2\,\sigma_{\mathrm{SED}} \geq f_{\mathrm{cut}}$, where f_{SED} is the SED best fitting flux and σ_{SED} is the SED flux uncertainty derived from χ^2 distribution statistics (Section 3.1). The left Y axis ρ_{beam} has the same definition as Fig. 1. The right Y axis in each panel is the total number of sources for fitting at each band. The posterior detection limit 1σ at each band is labelled as the black color text in each panel. The flux cutting value f_{cut} labelled in red color in each panel. We determine f_{cut} satisfying $\rho_{\mathrm{beam}} \lesssim 1$ and $1\sigma \lesssim f_{\mathrm{cut}} \lesssim 3\sigma$, so that the photometry will fit the most possibly detectable sources without significant blending problems.

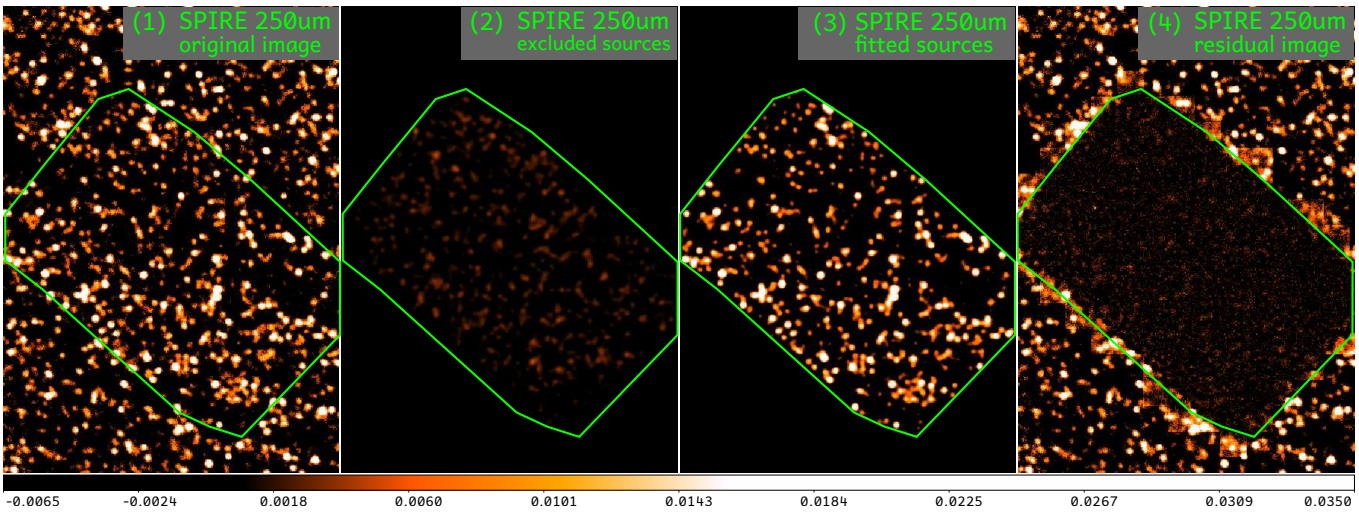

FIG. 6.—: SPIRE 250 μm photometry images as an example of our photometry method. Panel (1) is the original image of SPIRE 250 μm. The green boundary indicates the sky coverage of our 24+radio catalog (Section 2.4). Panel (2) is the modeled image of those excluded sources using their SED best fitting fluxes. These sources are excluded from fitting in our *"super-deblended"* prior source list (Section 3.2), while all other sources are fitted as prior sources because of their higher likelihood of being detected at 250 μm. Panel (3) is the best fitting model image of these prior sources after running *galfit* photometry (e.g. Section 2.2), and panel (4) is the resulting residual image. The image in panel (1) is the sum of panels (2), (3) and (4). Scales are the same for all panels as indicated by the bottom color bar. The flux unit is Jy/beam.

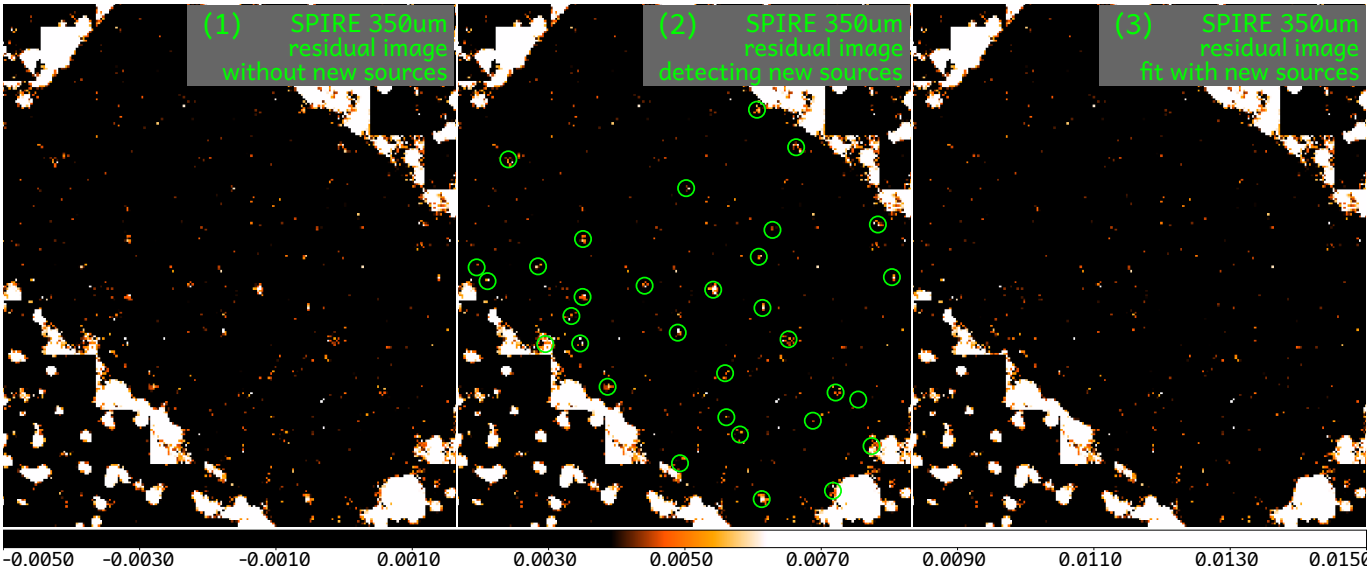

FIG. 7.—: We show the extraction of additional sources from residual image. Panel (1) and (2) are the residual image after fitting prior sources in prior catalog. The two images are identical, but panel (2) shows the new sources extracted by SExtractor. Panel (3) is the new residual image after re-running the photometry with the additional sources. All panels have the same intensity scale and the flux unit is Jy/beam.

of uncertainty (Pannella et al. 2015; Skelton et al. 2014) – we do not allow fitting beyond this boundary even if the minimum χ^2 were to be found at the edge of the interval, to avoid getting solutions too inconsistent with the optical constraints. For IRAC sources without any available optical/near-IR photometric redshift ($\sim$ 10% of the total IRAC catalog, but only 2.3% of the 3306 24+radio priors [27]) we allow the full range $0 < z < 8$ for the SED fitting.

For each band the SED fitting procedure returns a most likely expected flux ($f_{\rm SED}$), as well as its uncertainty ($\sigma_{\rm SED}$) based on the χ^2 statistics. Of course, this procedure requires that we can associate a well-behaved, (quasi-)Gaussian error to the fluxes measured in all shorter-wavelength bands. The

[27] They could be real extremely red galaxies, or perhaps blends or other problems that might affect cross-matching. Further exploration on this is beyond the scope of this paper.

description of the derivation of reliable flux uncertainty will be presented in Section 5.

3.2. *Optimized prior source lists for each FIR/mm band*

Fig. 5 shows the number of prior sources per beam plotted as a function of $f_{\rm SED}+2\,\sigma_{\rm SED}$. We add twice the flux uncertainty to the best-fit flux in order to conservatively estimate a plausibly maximum flux for each source. For each band we show a black vertical line reporting the median $1\,\sigma$ flux uncertainty that we finally obtain from our procedure (see Table 1).

Using these figures we would like to determine a $f_{\rm cut}$ value for further selection: sources with $f_{\rm SED}+2\,\sigma_{\rm SED}$ larger than $f_{\rm cut}$ are maintained and fitted as prior sources (hereafter *selected* sources), while those fainter than this limit are excluded from the fit (hereafter *excluded* sources, whose best fitting flux will be subtracted from the image in the next section). A larger $f_{\rm cut}$ will lead to less confusion in fitting (i.e. a smaller number density of fitted sources, $\rho_{\rm beam}$) but a larger number of fainter sources to be subtracted, and vice versa. Thus we set $f_{\rm cut}$ by considering both $\rho_{\rm beam}\lesssim 1$ and $1\,\sigma\lesssim f_{\rm cut}\lesssim 3\,\sigma$ at each band, where σ is the empirical median noise at this band (from simulation). The the upper boundary $3\,\sigma$ corresponds to a flux already fainter than $3\,\sigma$ detection limit (since it contains a $2\,\sigma_{\rm SED}$ contribution). And the lower boundary is set to $1\,\sigma$ to avoid fitting sources that are too faint for the data.

Regardless of these criteria, we also always keep as priors and fit any source that was significantly detected in the previous (shorter wavelength) band with S/N >3. In this way, for sources that have high S/N in the preceding band but are predicted to be too faint at the current band, we can still obtain an upper limit which is useful in SED fitting.

In Fig. 5, the 24+radio sources are tested with various $f_{\rm cut}$. The absolute number of the selected sources (shown in the right Y axis) is largely reduced to only $\sim$30% of the total number (3306) at 350 μm and 500 μm bands (overcoming blending), and to $\sim$15% at 1.16 mm (avoiding fitting too faint sources).

3.3. *Subtract excluded sources and fit selected sources*

The excluded sources with $f_{\rm SED}$ lower than $f_{\rm cut}$ do still contribute some weak flux in the observed images, and could thus boost the photometry for sources retained for fitting. Therefore we first make a model image of those excluded sources with *galfit* by fixing their fluxes to the predicted values, then subtract the faint-source-model-image from the observed original image and obtain a faint-source-subtracted image. The *galfit* photometry is then performed on the faint-source-subtracted image for the selected prior sources in a similar way as described in Section 2.2. In Fig. 6, we present the images at SPIRE 250 μm as an example of this procedure. Panel (1) is the original image, panel (2) is the faint-source-model-image, panel (3) is the best fitting model of the selected prior sources obtained from *galfit* photometry on the faint-source-subtracted image, and panel (4) is the final residual image. Thus panel (1) image is the sum of panel (2), (3) and (4) images. In Appendix we show for each band all the images produced during these steps. It is interesting to compare the total flux subtracted from the original images (for faint excluded sources) with that actually extracted from the fitted sources. This reach up to 30% of the total flux in the worst cases for longer wavelength SPIRE bands, where only 15-20% of the original priors are actually fitted, and is generally much smaller for other bands.

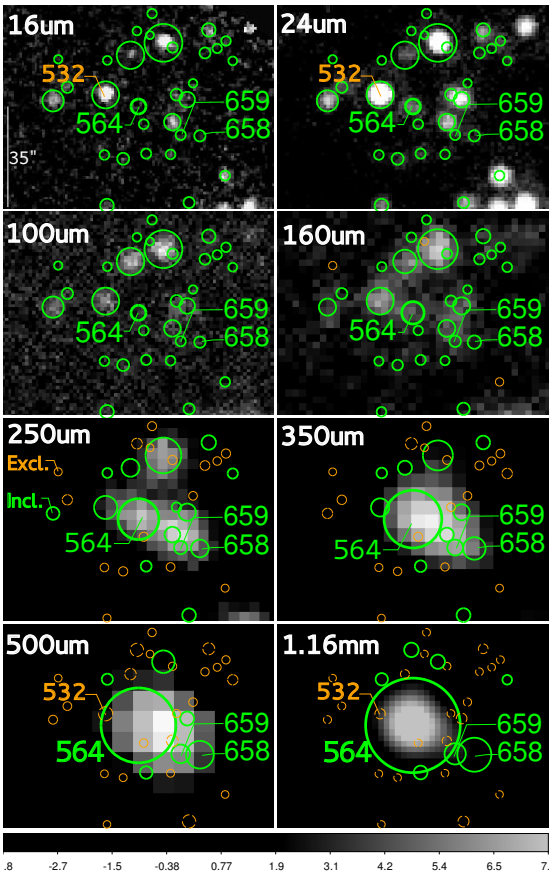

FIG. 8.—: Multi-wavelength cutouts around GN20 (Daddi et al. 2009, ID 564 in this work). Each circle represents a 24+radio prior source (Section 2). Green circles are selected for fitting (marked "Incl." in the 250 μm panel) while orange circles are excluded (marked "Excl."). Circles have sizes proportional to their flux at each band (i.e. measured flux for fitted sources or SED-predicted flux for excluded sources, but with a minimum value of 0.5″ and a maximum value of the PSF FWHM). The SEDs of the four marked sources, ID 564 (GN20), 658 (GN20.2a), 659 (GN20.2b) and 532 are shown in Fig. 9. ID 532 starts to have too faint SED-predicted flux (even when augmented by twice the uncertainty) at 500 μm (indicated by the vertical dashed line) hence is excluded from the fitting list at this band.

The selected prior source list for fitting extends to sufficiently faint (i.e. $<3\sigma$) sources in each band, that we do not expect all sources used for the PSF fitting to actually be detected with S/N>3 in the extraction process. The number of S/N>3 detections ($N_{\rm S/N>3}$) are generally of order of $1/3$ of all fitted sources ($N_{\rm fit}$). $N_{\rm fit}$ and $N_{\rm S/N>3}$ of all bands are listed in Table 1.

3.4. *Additional sources in the residual image*

Although the combination of 24+radio provides a very deep prior source catalog for FIR/mm bands, some less massive, radio-quiet high-z galaxies could still be missed. For example, in Fig. 2 and 3, the $z\sim$3–5 SEDs have 24 μm and 20 cm flux just about or even below the detection limits. Due to the diversity of galaxy properties, i.e. PAH fraction or FIR-radio correlation scatter, some of these sources will be missed in

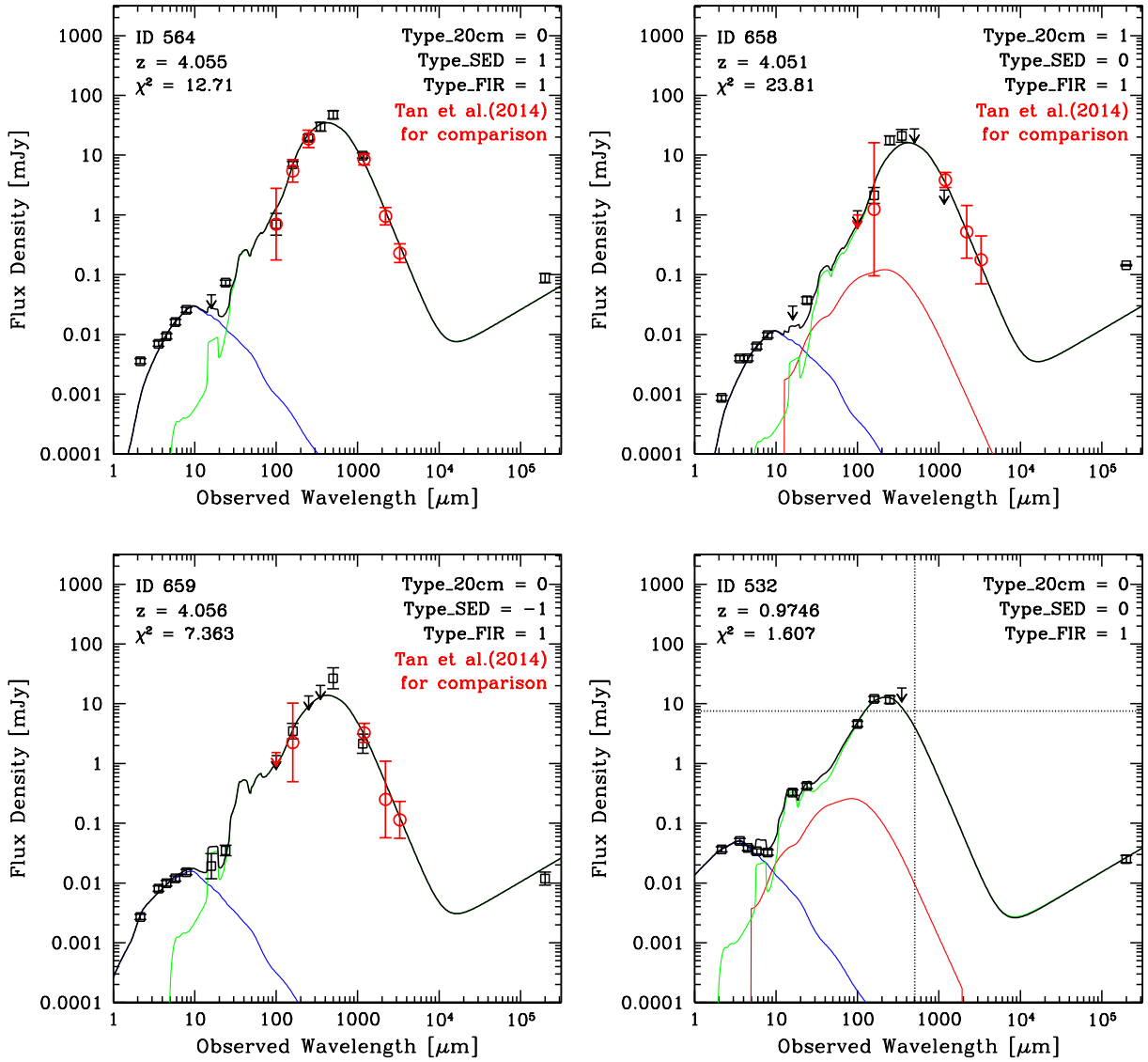

FIG. 9.—: The SEDs of the four marked sources in Fig. 8. In the ID 564 (GN20), 658 (GN20.2a) and 659 (GN20.2b) panels, we show the red data points from Tan et al. (2014) for comparison, which are not used in SED fitting but show very good consistency. In the ID 532 panel, the 500 μm SED-predicted flux (indicated by the vertical dashed line) becomes fainter than the horizontal dashed line even when raised by twice the uncertainty, hence it is not fitted at this band. The redshift and SED fitting best χ^2 are shown in the upper left corner of each panel. The three SED tuning parameters are shown in the upper right corner. See Section 3.1 for details.

our 24+radio prior list, but might have detectable SPIRE or (sub)mm fluxes.

We search for additional sources in our data by running blind-extraction with SExtractor (Bertin & Arnouts 1996) in the residual images, then re-run *galfit* together with catalog sources to see if they can be detected. We limit our blind-extraction region to be only within the 24+radio catalog coverage. This is done by measuring the perimeter of 24+radio sources and setting pixels outside of the perimeter to NaN (Not-a-Number) values. Then we run SExtractor on the masked residual image with a detection threshold of about 3.0 to detect all obvious sources (by also checking by eye).

We re-run the *galfit* fitting once including prior sources and additional sources, and do simulation-based flux and uncertainties corrections (see Section 5), then check the S/N of the additional sources to decide whether we keep it or not. About 3/4 of the additional sources will not be kept because their final S/N is below 3. We run again the *galfit* fitting including prior sources and only those kept additional sources.

In Fig. 7, we show the SPIRE 350 μm as an example. Panel (1) and panel (2) show the same residual image before extracting additional sources, and the green circles in panel (2) highlight the additional sources which are extracted by SExtractor then fitted with *galfit* and got S/N $>$ 3. Panel (3) shows the new residual image after we run the final *galfit* fitting including prior sources and the kept additional sources. We list

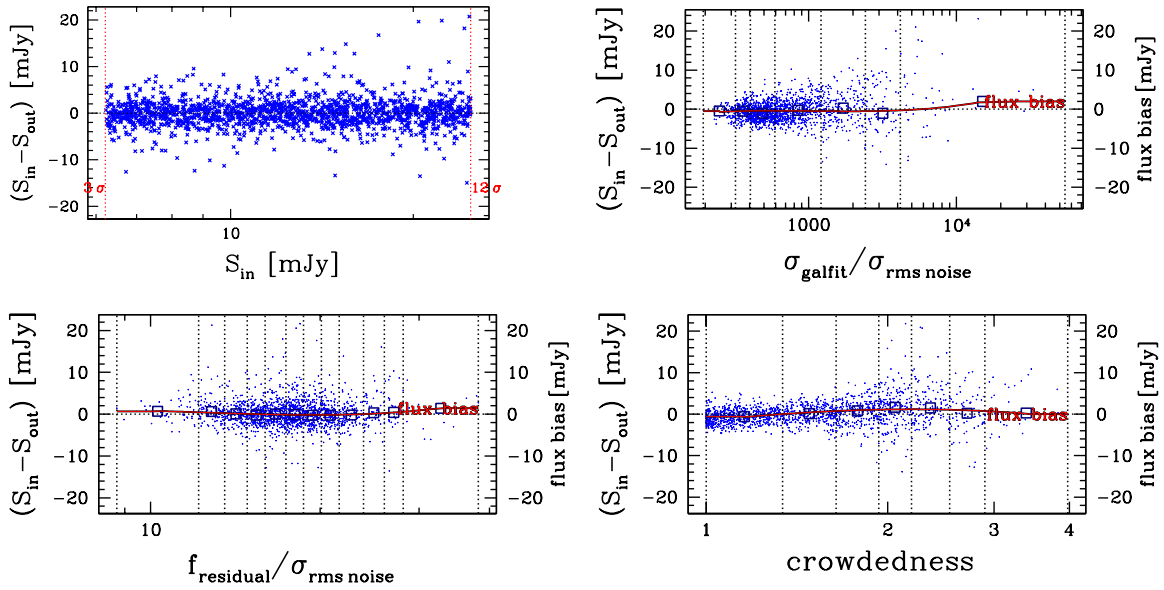

FIG. 10.—: Panel (1) shows the difference between input and output flux of simulated sources ($S_{in}-S_{out}$) versus the input flux (i.e. true flux). In panel (2) to (4), we bin simulated sources by three measurable parameters: the *galfit* flux uncertainty normalized by the local rms noise, the flux on residual image also normalized by the local rms noise, and the *crowdedness* parameter which measures the blending situation at each source position (see text in Section 5.2). Dashed vertical lines indicate the bins. We measure the mean of $S_{in}-S_{out}$ (blue square data points), which is just flux bias, then fit a polynomial function to link flux bias to each parameter (red curves). In this way, flux bias can be better corrected for different sources. Similar figures for all other bands are shown in Appendix.

the number of final detected additional sources at each band in Table 1.

Also note that we do not include these additional sources in the scientific analysis presented in the final sections of this paper, because their positions are uncertain and about half of them lack optical/near-IR counterparts within 3″ (90% if within 1″). Most of them are also not detected in two continuous SPIRE/mm bands. There should still be a certain fraction of these sources that are false detections, even though we have adopted the approach of doing twice the *galfit* fitting (but meanwhile in this way we could not simply use negative image extraction method to estimate the false detection rate). Currently we just focus on all 24+radio catalog sources, although there are likely genuine $z>3$ sources among these objects that we include in our final catalog for completeness (e.g. HDF850.1, Walter et al. 2012, which is the additional source ID 850011 in our catalog).

4. AN EXAMPLE OF OPTIMIZING PHOTOMETRY PRIOR SOURCE LIST AROUND GN20

We illustrate how we choose prior sources according to their SED predicted flux in Fig. 8, the multi-wavelength cutouts around the luminous $z=4.055$ starburst GN20 (Daddi et al. 2009), which corresponds to ID 564 in our catalog. The circles in the figure represent all 24+radio prior sources (Section 2). Green circles are the prior sources selected for fitting, while orange circles are the excluded sources.

The circle sizes in each panel are proportional to the source flux at each band: for fitted sources (green circles) we use for this the actual measured flux, while for the excluded sources (orange circles), we use the SED-predicted flux. The circles have a minimum size for plotting for $\leq 1\sigma$ flux and a maximum size for $\geq 10\sigma$ flux, where 1σ is the mean flux uncertainty of all detected sources at each band (i.e. detection limit, see Table 1).

At each step, as described in the previous sections, we first construct the SED for each 24+radio prior source with available bands, then choose which to fit and which not. Here we consider 4 marked sources in Fig. 8 as examples: ID 532, 564, 658 and 659. ID 532 is one of the brightest sources at 16 μm and 24 μm bands, but becomes relatively fainter sources at SPIRE bands. It has a spectroscopic redshift of 0.9746 thus its SED drops quickly at SPIRE bands. Its final SED is shown in the last panel of Fig. 9. Using the SED fitting before the 500 μm photometry, ID 532 starts to have a too low SED-predicted flux ($f_{\rm SED}$) even augmented by twice the error ($2\sigma_{\rm SED}$): $f_{\rm SED}+2\sigma_{\rm SED}<f_{cut,500\,\mu{\rm m}}$, where the $f_{cut,500\,\mu{\rm m}}$ is the critical value we chose as shown in the 5th panel of Fig. 5. Thus we do not fit ID 532 at 500 μm. Meanwhile, its predicted flux contribution to the observed 500 μm image is subtracted as described in Section 3.3, so that we can measure the real, deboosted flux for the remaining prior sources.

ID 658 and ID 659 are two sources around GN20 that have the same spectroscopic redshift of 4.055 (naming GN20.2a, GN20.2b respectively, they are part of a proto-cluster at that redshift) but are fainter. Tan et al. (2014) presented their photometry and SEDs, as well as mm continuum and spectral line observations. Their mm photometry provides tight constraints on the tail of the dust SED. In Fig. 9, we compare our deblended photometry and SEDs with the photometry of Tan et al. (2014). Their data points are shown in red color. For GN20, they did not measure the SPIRE fluxes, and the flux uncertainties at PACS 100 μm and 160 μm are larger than ours. Their mm photometry agrees very well with our SEDs,

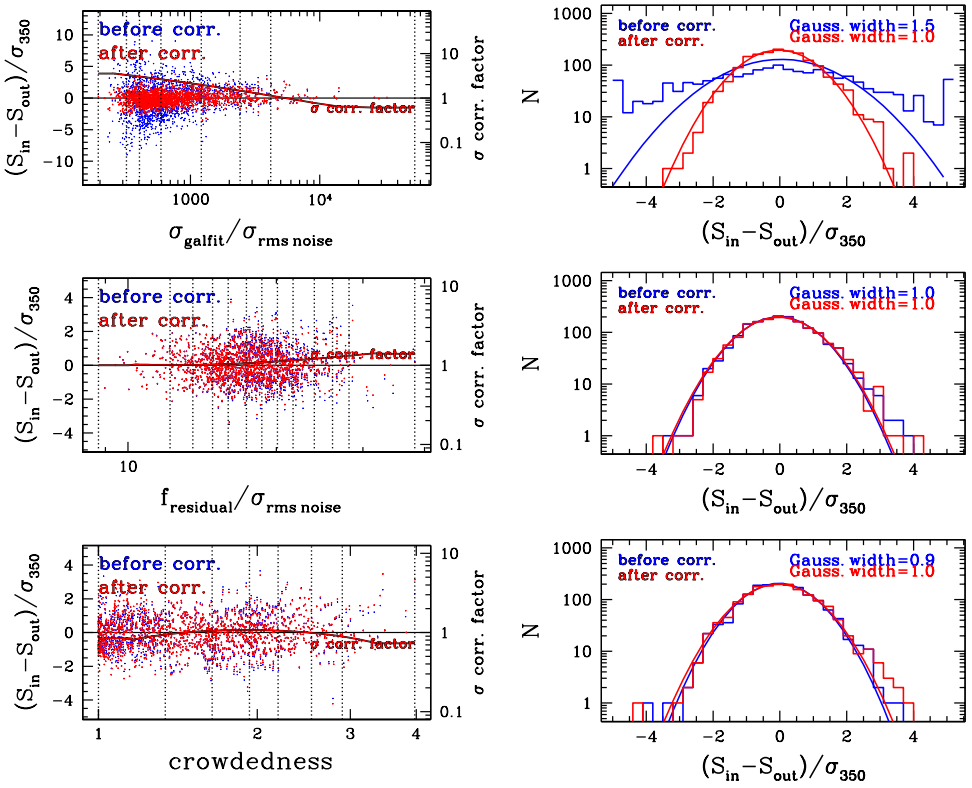

FIG. 11.—: **(Left panels)** For simulated objects (at 350 μm as an example), we show the difference between input (real) and output (measured) flux divided by flux uncertainty in Y axis, i.e. $(S_{in}-S_{out})/\sigma$. From top to bottom, we analyze this quantity against three parameters as indicated by the X axis label. We bin objects as indicated by the vertical dashed lines and compute the rms in each bin for deriving the correction factors as described in Section 5.3 (i.e. imposing that, in bins defined for quantities in the X axes, the rms dispersion of $(S_{in}-S_{out})/\sigma$ is equal to 1.0). We show the data points before and after correction (i.e. $(S_{in}-S_{out})/(\sigma$, uncorrected) and $(S_{in}-S_{out})/(\sigma$, corrected)) in blue and red respectively. **(Right panels)** The histograms of the $(S_{in}-S_{out})/\sigma$ in logarithm space, and with a solid line representing a best fitting Gaussian profile to the inner part of each histogram. After the three-step corrections the histograms are well-behaved and generally well consistent with a Gaussian distribution. Similar figures for all other bands are shown in Appendix C.

noting that the SEDs are fitted only with the black data points in this work. For the fainter GN20 proto-cluster members, ID 658 and ID 659, Tan et al. (2014) provided only PACS fluxes, which are all with S/N < 3. Our photometry provides more data points across PACS to SPIRE bands, and our SEDs are in very good consistency with their mm continuum observations.

5. SIMULATION-BASED FLUX AND UNCERTAINTY CORRECTION

Extensive Monte Carlo simulations are used in our *"super-deblended"* photometry for two main purposes. Firstly, the simulation can verify potential flux biases, so that we can correct for any imperfect sky background or other subtle systematic effects. Secondly, it helps us to understand and calibrate the uncertainties of photometric measurements.

In fact, the flux uncertainties estimated by *galfit* are based on the diagonalizing and projecting of the covariance matrix hence do not properly reflect real errors (Peng et al. 2002). In simulations, we have not only the *galfit* output but also the simulated input information, therefore we can link the real uncertainty to the *galfit* output with measurable source properties. We will present the Monte Carlo simulation method in Section 5.1, the flux bias analysis in Section 5.2, and the flux uncertainty analysis in Section 5.3.

5.1. *Monte Carlo simulation*

We simulate one source at a time in the faint-source-subtracted image[28]. The positions of the simulated sources are fully randomly generated within the surveyed area, not avoiding bright sources. Their input fluxes, S_{in}, are uniformly distributed in log space within the range of $\sim 1\sigma$ to $\sim 30\sigma$, where σ is the mean flux uncertainty at each band (see Table 1).

We add each extra simulated source to the 24+radio prior sources list which has already been filtered for that band (i.e. included sources, as well as additional sources from residual images, see Section 3.3), then perform the PSF fitting photometry including all active priors and an extra prior at the position of the simulated source. We also perform two-pass *galfit* fitting as in Section 2.2 to allow varying the position of priors in the second-pass if they have high S/N from the

[28] The faint-source-subtracted image is the image with excluded source models subtracted from the originally observed image, see Section 3.3.

TABLE 1: GOODS-N *"Super-deblended"* Photometry Results

Band	Instrument	Beam FWHM [a]	$\rho_{\rm fit}$ [b]	$N_{\rm fit}$ [c]	$N_{\rm excl.}$ [d]	$N_{\rm S/N>3}$ [e]	$N_{\rm add.}$ [f]	$1\,\bar{\sigma}$ [g]
		arcsec	beam^{-1}					mJy
24μm	Spitzer/MIPS	5.7	1.205	19437	0	3056	0	5.165×10^{-3}
20cm	VLA	1.7/2.0	0.107	19437	0	1328	0	2.744×10^{-3}
16μm	Spitzer/IRS/PUI	3.6	0.082	3306	0	1335	0	7.681×10^{-3}
100μm	Herschel/PACS	7.2	0.326	3294	12	1178	0	0.315
160μm	Herschel/PACS	12.0	0.862	3137	169	1153	18	0.681
250μm	Herschel/SPIRE	18.2	0.973	1540	1766	668	13	1.571
350μm	Herschel/SPIRE	24.9	1.142	966	2340	292	10	2.072
500μm	Herschel/SPIRE	36.3	1.181	470	2836	125	17	2.570
850μm	JCMT/SCUBA2	14.8	0.160	667	2639	75	19	0.942
1160μm	AzTEC+MAMBO	19.5	0.374	515	2791	43	11	0.661

[a] Beam FWHM is the full width at half maximum of the circular-Gaussian-approximation point spread function of each image data.
[b] $\rho_{\rm fit}$ is the number density of prior sources fitted at each band, normalized by the Gaussian-approximation beam area.
[c] $N_{\rm fit}$ is the number of prior sources fitted at each band.
[d] $N_{\rm excl.}$ is the number of prior sources excluded from fitting at each band. These sources are subtracted from original image with their spectral energy distribution predicted flux at each band.
[e] $N_{\rm S/N>3}$ is the number of prior sources with S/N ≥ 3 (i.e. detected) at each band.
[f] $N_{\rm add.}$ is the number of S/N ≥ 3 additional sources that are not in the prior source catalog but blindly-extracted from the intermediate residual image product at each band (see Section 3.4).
[g] $1\,\bar{\sigma}$ is the detection limit computed as the median of the flux error of all detected sources at each band.

return of first-pass. At the end of each pass, we run the following Sections 5.2 and 5.3 corrections. The *galfit* output flux of the simulated source is S_{out}, and the flux uncertainty given by *galfit* is σ_{galfit}.

Finally, this process is repeated ∼3000 times. Therefore, at each band, we have ∼3000 S_{in}, S_{out} and σ_{galfit}. In addition, we measured several additional properties for each simulated source: for example the local rms noise value $\sigma_{rms\,noise}$ for each source, measured in the instrument noise image data; the local absolute flux in the residual image (hereafter $f_{\rm residual}$), measured by computing the total absolute pixel values in the PSF aperture for each fitted prior source; the local scatter in the residual image, measured also in the PSF circle; and the *crowdedness* parameter, computed by summing up the Gaussian weighting of all sources at current source i position:

$$\sum_{j=1}^{N} e^{\left(-d_{j,i}^2/d_{\rm PSF}^2\right)} \quad (1)$$

where $d_{j,i}$ is the angular distance in arcsec from source j to current source i and $d_{\rm PSF}$ is the FWHM in arcsec of current band PSF. Defined in this way, the *crowdedness* is a weighted measure of the number of sources present within the beam, including the specific source under consideration.

These measurable parameters are aimed to reflect key information about the quality of fitting and the actual local crowding (hence blending) of prior sources. We will make use of them with the simulation results in order to calibrate the best possible flux bias and flux uncertainty corrections.

In addition to the uncertainties estimated in this way, we add in quadrature to each object's flux uncertainty the appropriate contribution (when relevant) to account for astrometry dispersion when fitting at fixed spatial positions.

5.2. *Flux bias correction*

The statistics of the differences between input flux and output flux $S_{in}-S_{out}$ can be used to verify and correct the bias of the *galfit* flux measurements. In Fig. 10 we present the analyses of $S_{in}-S_{out}$ based on the simulation data at SPIRE 350 μm as an example. In panel (1) $S_{in}-S_{out}$ is plotted against the simulation input flux S_{in}, which covers about $1-30\times$ the detection limit $\sigma_{350\,\mu\rm m}$. The overall median of $S_{in}-S_{out}$ is generally small, indicating that the (constant) background levels used in the *galfit* work are quite accurate.

For all bands we explore the dependence of $S_{in}-S_{out}$ on the following three key properties: (1) the flux uncertainty σ_{galfit}, which is directly the output of *galfit* fitting; (2) the residual flux $f_{\rm residual}$, measured in the output residual image; and (3) the *crowdedness* , which is a proxy of prior source blending situation as described in the previous section. When testing parameter (1) and (2), we further use the rms noise $\sigma_{rms\,noise}$ to normalize these 2 parameters, in order to account for the local rms variation in case of non-uniform depth of the data over the whole GOODS-N region. For example, if sources at the map center have smaller rms noise while sources further out have larger rms noise, the outer sources will likely have higher σ_{galfit} and $f_{\rm residual}$ only because of their locations.

As shown in panel (2) to (4) of Fig. 10, we bin simulated sources by source properties. In each bin we compute the median of $S_{in}-S_{out}$, which is just the flux bias f_{bias}. Then we fit the f_{bias} in each bin by a 3-order polynomial function. The fitted polynomials are shown as the red curves in panel (2) to (4). Note that the quantities along the x-axes are measurable for each real fitted source, thus these functions are also applicable to each real source.

5.3. *Flux uncertainty correction*

With the Monte Carlo simulations, we also provide a path towards obtaining reliable estimations of flux uncertainties. The flux error returned by *galfit* (σ_{galfit}) only reflects the fitting uncertainty in a formal way (e.g. Peng et al. 2002). In fact, the *galfit* formalism is optimized for optical/near-IR images and assumes non-correlated noise (all pixel are independent) in the data. Thus it cannot fully account for real uncertainties especially in the presence of correlated noise and confusion noise. Imperfect flux uncertainties will strongly affect the power of SED fitting for individual sources and the assessment of detections or lack thereof.

We analyze the statistics of $(S_{in}-S_{out})/\sigma_{galfit}$ with simulation data, which should have a rms dispersion of 1.0

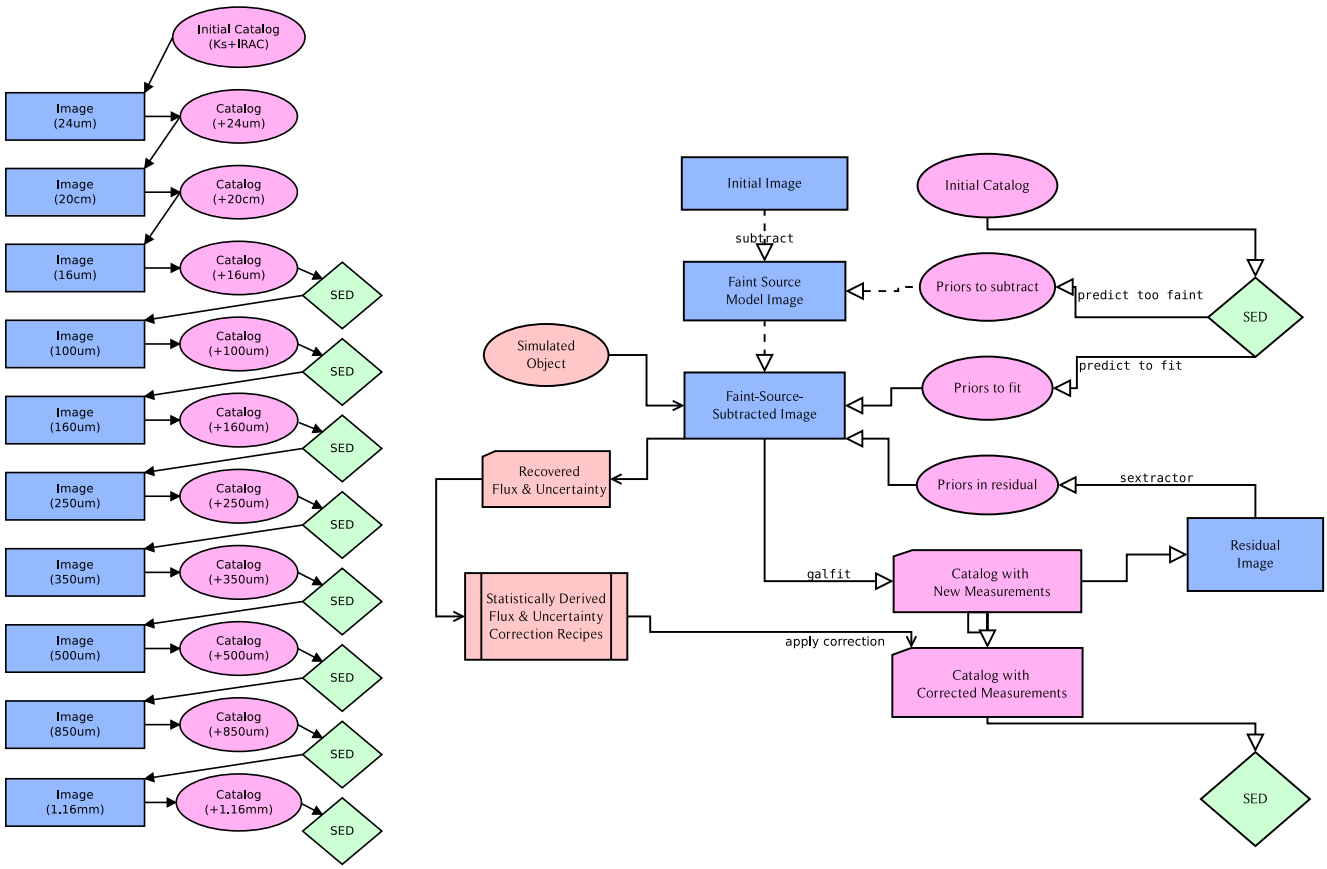

FIG. 12.—: **(Left:)** The flow chart of our photometry procedures applied to all bands. We start from the IRAC catalog and perform photometry for 24 μm, 20 cm and 16 μm as described in Section 2. Then SED fitting is used to help determine an updated source prior list for each FIR/mm band, as illustrated in Section 3. **(Right:)** The *"super-deblended"* procedures at each FIR/mm band. For each source in the initial catalog, we run SED fitting and predict current band flux and uncertainty (Section 3.1). Then we split prior sources into two lists: "priors to subtract" and "priors to fit" (Section 3.2). We make a source-model-image for sources in the former list and subtract it from the initial observed image, resulting into a faint-source-subtracted image on which the *galfit* photometry are performed for the latter list (Section 3.3). We further blindly extract additional sources on the residual image and re-run the *galfit* photometry with "priors in residual" (Section 3.4), which results in the "catalog with new measurements". Meanwhile, we generate simulated objects in the faint-source-subtracted-image, then recover flux and analyze and calibrate uncertainties as fully described in Section 5. We derive sophisticated "correction recipes" that make use of measurable parameters, thus for each fitted source, we can measure these parameters and apply the corrections to real measurements. Finally, we obtain the "catalog with corrected measurements" for each band and fit the SED again which will be used in the next band or as the final output after the last FIR/mm band.

by definition if uncertainties are well defined. Taking 350 μm simulation as an example, in the left upper panel of Fig. 11, we bin simulated objects by the measurable parameter $(\sigma_{galfit}/\sigma_{\rm rms\,noise})$ as in previous section, and in the middle and right upper panel we show the histograms of $(S_{in}-S_{out})/\sigma_{galfit}$ (in blue) and $(S_{in}-S_{out})/\sigma_1$ (in red), where σ_1 is the first-step corrected flux uncertainty. The blue histogram is clearly much broader than a width of 1.0, indicating that σ_{galfit} are substantially underestimated.

We determine correction factors as a function of the X axis parameter, requiring that, in bins defined for quantities in the X axis, the rms dispersion of $(S_{in}-S_{out})/\sigma$ is equal to 1.0. In each bin, we compute the rms of $(S_{in}-S_{out})$ and the median of σ_{galfit}, then calculate their ratio, which is exactly the correction factor that we need for correcting σ_{galfit} to the real uncertainty of $(S_{in}-S_{out})$. Similarly to the previous section, we fit the correction factor as a 3-order polynomial function against the X axis parameter. The fitted polynomial functions are shown as the red curves in the figure. In this way, we obtain the first-step corrected σ_1, whose histogram is shown in red, and is much closer to a width of 1.0. We find that generally for objects whose *galfit* uncertainties are around the median, the flux uncertainties are often quite underestimated, while for the objects with the largest uncertainties (typically those affected by substantial deblending uncertainties) they are often overestimated (real errors are smaller as judged from our simulations).

The first-step corrected uncertainty histograms sometimes can have asymmetric shapes, which indicate that there are still some systematic biases. Thus we take in turn the first-step corrected uncertainty σ_1 as the input and perform the second and the third steps. In the second step, we first perform the flux bias correction with parameter $f_{\rm residual}/\sigma_{\rm rms\,noise}$, then perform the uncertainty correction with the same param-

eter as illustrated by the middle row panels of Fig. 11. Then, similarly, in the third-step we apply the flux bias correction, followed by the flux uncertainty correction with the parameter *crowdedness* . Therefore, with these correction recipes, we are able to apply the correction to real fitted sources.

We have also tried multiple iterations or different combinations of the three-steps, for example after the three-step processing, we use the output corrected flux and uncertainty as the input for several more times three-step processing, but the corrected values and histograms are stable and can not be further improved.

Similar figures for all examined bands are reported in the Appendix C. In general, we find that the *galfit* errors (the initial uncorrected ones) are underestimated except when they are substantially larger than the average (due to fit degeneracies), in which case they are often overestimated. Similarly, very large (small) flux residual at the fitted positions imply that flux uncertainties are overestimated (underestimated). An analogous effect is seen for the *crowdedness* parameter. We have analyzed a number of other parameters (including flux itself, spatial positions, redshift, different kind of *crowdedness* and residual definitions, etc.) and we found no other significant dependency to further correct flux uncertainties.

6. SUPERDEBLENDED PHOTOMETRY - OVERALL WORK FLOW

Based on the simulation analyses, we apply the correction recipe to real fitted sources. For each fitted source, we begin with the flux uncertainty given by *galfit* fitting (σ_{galfit}), then measure the local rms noise on the rms image ($\sigma_{rmsnoise}$), the local residual flux on the residual image ($f_{\rm residual}$), and the *crowdedness* parameter using all fitted prior source coordinates at each band. Therefore the aforementioned three measurable parameters can be obtained for each fitted source. We compute the correction factor from each parameter and correct flux bias and uncertainty sequentially in the steps described in Section 5.2 and 5.3. Finally, we obtain the *"super-deblended"* GOODS-N FIR+mm photometry results.

Our *"super-deblended"* method of optimizing prior source lists with the help of the highly optimized SED fitting ensures that we are fitting all the most likely detectable prior sources in each band. The flux and uncertainty corrections we derive on a source-by-source basis make our detections and SED fitting more reliable. We list the final detection limit ($1\sigma^{det.}$) and number of S/N > 3 sources ($N_{\rm S/N} > 3$, i.e. single band detected catalog sources) at each band in Table 1.

When all photometric measurements have been derived for all bands we run a final global SED fitting, from which we derive various galaxy properties. While a detailed discussion of extraction of physical parameters and their uncertainties from FIR galaxy SEDs (which would include AGN components, dust temperature, IR8, radio excess, etc) is beyond the scope of this work, for the sake of the scientific analysis presented in this paper (see Section 8) it is worth mentioning the derivation of the best fitting LIR, and also SED-driven photometric redshifts. The latter are in most case a simple possible refinements of optical/near-IR photometric redshifts, corresponding to the redshift within the allowed range (close to existing photometric redshifts) where the best fit is obtained. However for the objects with no existing photometric redshift available, we fit over the whole $0 < z < 8$ range, and the SED fitting provides an estimate of their photometric redshift and uncertainty. We will investigate in a future publication the possible derivation of IR/radio photometric redshifts and their performance, improving over the work of Daddi et al. (2009) and several others.

The overall flow chart of our *"super-deblended"* method is presented in Fig. 12.

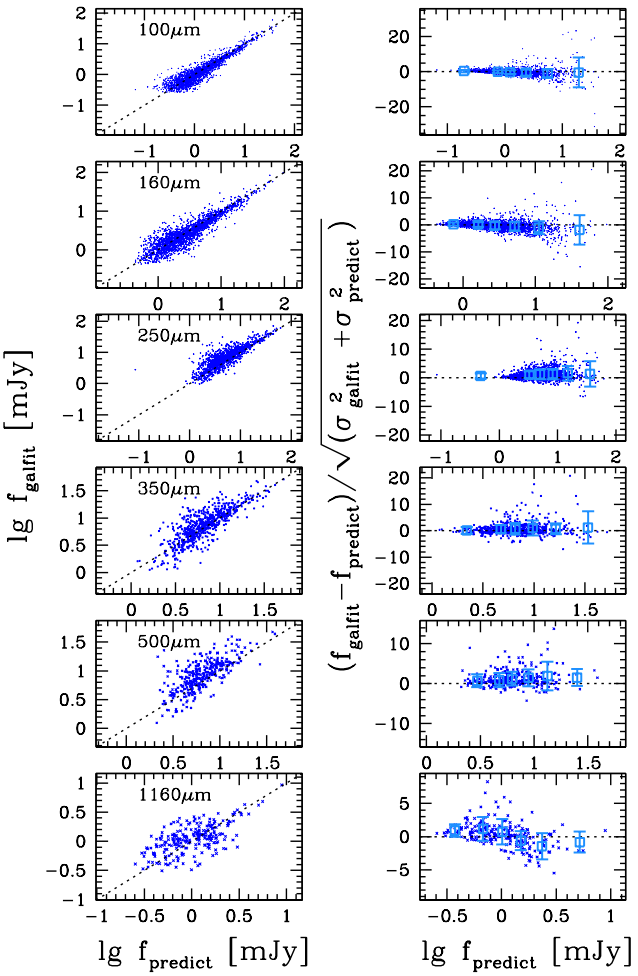

FIG. 13.—: Comparison between SED-predicted flux ($f_{\rm predict}$) before the *galfit* photometry step, and the newly measured flux (f_{galfit}) after the *galfit* photometry step for each band, as a demonstration of the performance of our SED prediction. The left panels show the flux-flux comparison in log space, while the right panels show the flux versus flux difference weighted by the combined error in linear space, for the same bands as the left panels. Because SED flux and error ($f_{\rm predict}$ and $\sigma_{\rm predict}$) are used **(a)** to determine which sources are too faint to be detectable, and **(b)** to subtract their flux contribution from the observed data (see Section 3.3), it is essential to ascertain that SED predictions are not subject to strong biases. In this figure, $f_{\rm predict}$ and f_{galfit} are generally consistent at all bands, though with larger dispersion (indicated by the error bars in the right panels) at longer wavelengths. The small skewness in the results be explained by the fact that only significant ($> 3\sigma$) detections are shown, which produces biasing toward sources with higher $f_{galfit}/f_{\rm predict}$ ratios.

7. QUALITY CHECKS AND KNOWN LIMITATIONS

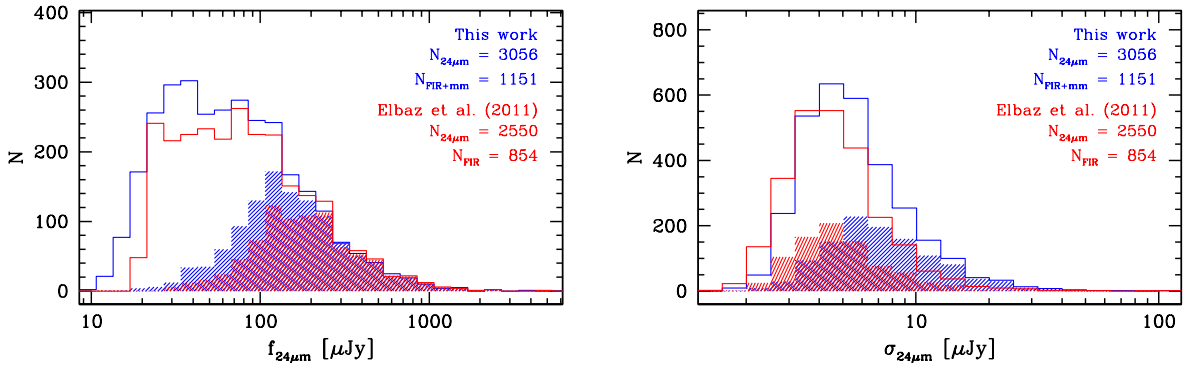

FIG. 14.—: Comparison of the 24 μm flux histogram (left) and flux uncertainty histogram (right) between this work and Elbaz et al. (2011). The open areas of the histogram show all prior sources, while the shaded areas represent the sources that are significantly detected (with $S/N_{\rm FIR+mm} \geq 5$ for our sources, or $S/N_{\rm FIR\,(100\,to\,500\mu m)} \geq 5$ for Elbaz et al. 2011 sources, see definition of $S/N_{\rm FIR+mm}$ in Section 8.1 and Equation 2). Results from this work are shown in blue, and for Elbaz et al. (2011) in red. In the left panel, the histograms of bright sources are consistent, but there are more sources from this work for fainter flux. This means that we have about 450 more candidate prior sources for the longer wavelength photometry than in Elbaz et al. (2011). The FIR to mm detected sources, which are the red and blue shaded areas, also show consistency for brighter fluxes but are more numerous in this work. In the right panel, due to the simulation-based flux uncertainty correction (see Section 5.3), the flux uncertainties in this work are generally higher, even for the FIR and 24 μm detected sources in the shaded area. The $N_{24\,\mu\rm m}$ is the number of $S/N_{24\,\mu\rm m} \geq 3$ sources in each catalog, and $N_{\rm FIR+mm}$ is the number of FIR-to-mm (or FIR 100-to-500 μm for Elbaz et al. (2011) catalog) sources.

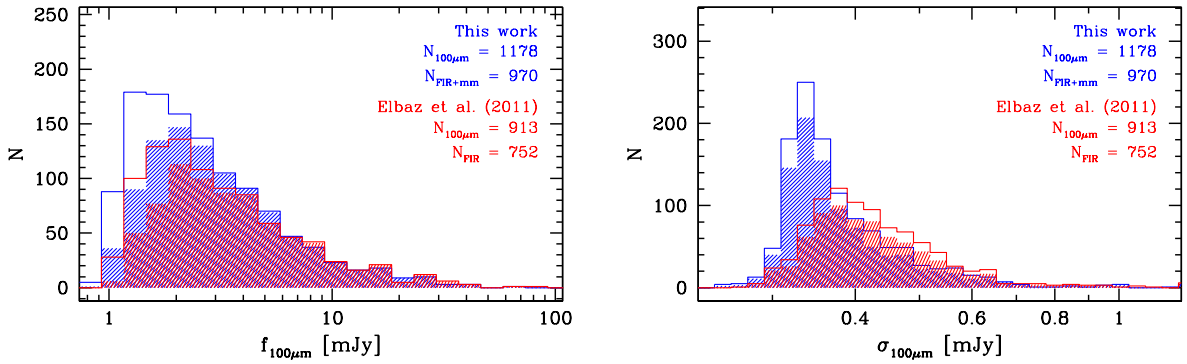

FIG. 15.—: Comparison of the 100 μm flux histogram and flux uncertainty histogram between this work and Elbaz et al. (2011). Colors and histograms are defined in Fig. 14. In the left panel, this work has about 200 more sources and span a slightly deeper flux range. In the right panel, after applied the simulation-based flux uncertainty correction (see Section 5.3), the flux uncertainties in this work are lower than that in Elbaz et al. (2011) catalog, both because of the larger number of fainter sources in the left panel and the simulation-based corrections to the flux uncertainty.

7.1. *Comparing SED predictions with measurements*

An important step in our procedure is to predict fluxes for sources in a given band before actually performing measurements in that dataset. Sources with predicted flux brighter than $f_{\rm cut}$ are retained to be fitted with *galfit*. For those fitted sources, we can now compare their measured flux to their SED predictions, in order to investigate the presence of any potential bias in the SED predictions of the fitted sources (and by extension also of the faint/subtracted sources).

These comparisons are shown in Fig. 13. In the left panels we compare $f_{\rm predict}$ and f_{galfit}, and in the right panels we show the difference $(f_{galfit} - f_{\rm predict})$ divided by the total uncertainty, against $f_{\rm predict}$. The error bars represent the combined uncertainties of σ_{galfit} and $\sigma_{\rm predict}$.

$f_{\rm predict}$ and f_{galfit} generally agree well with each other. There are a small fraction of sources having lower $f_{\rm predict}$ than f_{galfit} at the faint end as seen in the left panels (but less obvious in the right panels when actual flux uncertainties are kept into account). This small bias is driven by the requirement of a significant detection from *galfit* for a point to be shown in the plot, and vanishes when this selection bias is taken into account.

7.2. *Comparison to literature results*

Here we compare our 24 μm, PACS and SPIRE flux measurements and uncertainties with Elbaz et al. (2011), and 1.16 mm with Penner et al. (2011).

In Fig. 14, we compare our 24 μm flux and uncertainty histograms with the Elbaz et al. (2011) catalog. In the left panel, the flux histogram of $S/N_{24\,\mu\rm m} \geq 3$ sources in this work is

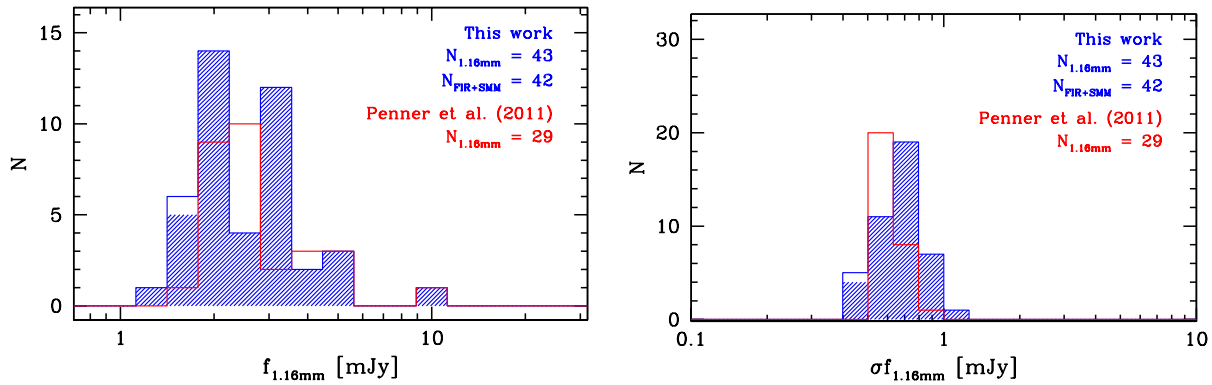

FIG. 16.—: Comparison of the 1.16 mm flux histogram and flux uncertainty histogram between this work and Penner et al. (2011). Colors and histograms are defined in Fig. 14. The fluxes from Penner et al. (2011) are deboosted fluxes when available. Most 1.16 mm detected sources are also FIR+mm detected sources. In the left panel, this work has about 10 more sources over a similar flux range. In the right panel, after applying the simulation-based flux uncertainty correction (see Section 5.3), the flux uncertainties in this work are slightly higher than those in the Penner et al. (2011) catalog. $N_{1.16\,\mathrm{mm}}$ is the number of $S/N_{1.16\,\mathrm{mm}} \geq 3$ sources in each catalog, and $N_{\mathrm{FIR+SMM}}$ is the number of PACS 100 μm to 1.16 mm $S/N \geq 5$ and $S/N_{1.16\,\mathrm{mm}} \geq 3$ sources.

shown in blue, and Elbaz et al. (2011) in red. The shaded area under each histogram represents the FIR+mm multi-band combined $S/N_{FIR+mm} \geq 5$ and $S/N_{24\,\mu\mathrm{m}} \geq 3$ sources, where S/N_{FIR+mm} is defined as Equation 2 in Section 8.1. Elbaz et al. (2011) do not include (sub-)mm bands, implying that for their sources the combined S/N only involves 100 μm to 500 μm photometry. For the bright sources, the flux histograms from both works are consistent, while for fainter sources, the flux histogram from this work shows more prior sources. It shows that we have about 450 more 24 μm detected candidate prior sources for the longer wavelength photometry than Elbaz et al. (2011). The shaded area, or the FIR to mm and 24 μm detected sources, also have a larger detection number in this work. The newly detected sources are fainter. Notice how IR-detected sources drop very rapidly below 100 μJy, suggesting that our prior sample is quite complete and possibly redundant for *Herschel* sources at typical redshifts (although we might still be somewhat incomplete for the highest redshift, as previously noted in Section2.4). In the right panel, due to the simulation-based flux uncertainty correction (see Section 5.3), the flux uncertainties in this work are generally higher, but should have less bias and be better representative of the true uncertainty in the measurements (see Section 5.3 and Section C). For the FIR and 24 μm detected sources in the shaded area, our flux uncertainties are also generally higher.

In Fig. 15, we compare the 100 μm flux and uncertainty histograms from this work and the Elbaz et al. (2011) catalog. In the left panel, this work has about 200 more sources and extends to a slightly deeper flux range. In the right panel, after applying the simulation-based flux uncertainty correction (see Section 5.3), the flux uncertainties in this work are lower than that in Elbaz et al. (2011) catalog, and this is both because of the excess fainter sources in the left panel and the simulation-based corrections to the flux uncertainties.

Other PACS and SPIRE bands have similar histograms as this band and hence are not shown here. The comparisons of 1.16 mm flux measurements and uncertainties with Penner et al. (2011) are shown in Fig. 16. We use their deboosted flux when possible. The number of sources are small at this band. But this work has about 10 more detections. The sources span a similar flux range in both works. After applying the simulation-based flux uncertainty correction (see Section 5.3), the flux uncertainties in this work are slightly higher than those in Penner et al. (2011) catalog. Similar to the 24 μm case, we believe that the difference is mainly due to the fact that our simulation-based corrections return more reasonable flux uncertainties (as far as seen by simulation data).

The one-to-one flux comparisons for the three SPIRE bands and 1.16 mm band are presented in Fig. 17. We cross-match common sources (with a distance limit of 5″ because of the large *Herschel* PSFs) and compare the flux between our catalog and the Elbaz et al. (2011) catalog. The majority of the sources show consistent fluxes, but some sources in the Elbaz et al. (2011) catalog have higher SPIRE fluxes, which is due to source blending. The two most extreme outliers are marked with their IRAC ID in the first panel. They are ID 14896 (ID 2132 in Elbaz et al. 2011) and ID 10611 (ID 1512 in Elbaz et al. 2011). ID 14896 is one of very few sources that have higher fluxes in our catalog than in that of Elbaz et al. (2011). It is due to the complex blending situation and Elbaz et al. (2011) assign most of the flux to a nearby source but little to this source. Fig. 18 shows the multi-band cutouts around this source. The three sources: ID 14896, ID 14867 and ID 15027 become blended at 160 μm. Their SEDs are shown in Fig. 19. Red data points for comparison are from Elbaz et al. (2011) in the ID 14896 and ID 15027 panels. ID 14867 has no counterpart in Elbaz et al. (2011). Note that the best-fit redshift is shown in the upper left corner of each panel (when available we fix the redshift to the spectroscopic redshift; the second and third sources both have spectroscopic redshifts). In the third panel, ID 15027 at a spectroscopic redshift of 1.371 is not likely to have SPIRE flux as high as the red data points. And in the first panel, the 20 cm and 500 μm flux of ID 14896 all suggest that its 250 μm flux is not likely as low as that reported by Elbaz et al. (2011). Thus in our opinion, for this case our deblending leads to more reasonable results. For the other extreme case mentioned above (ID 10611 and its surrounding sources), we have also checked their cutouts and

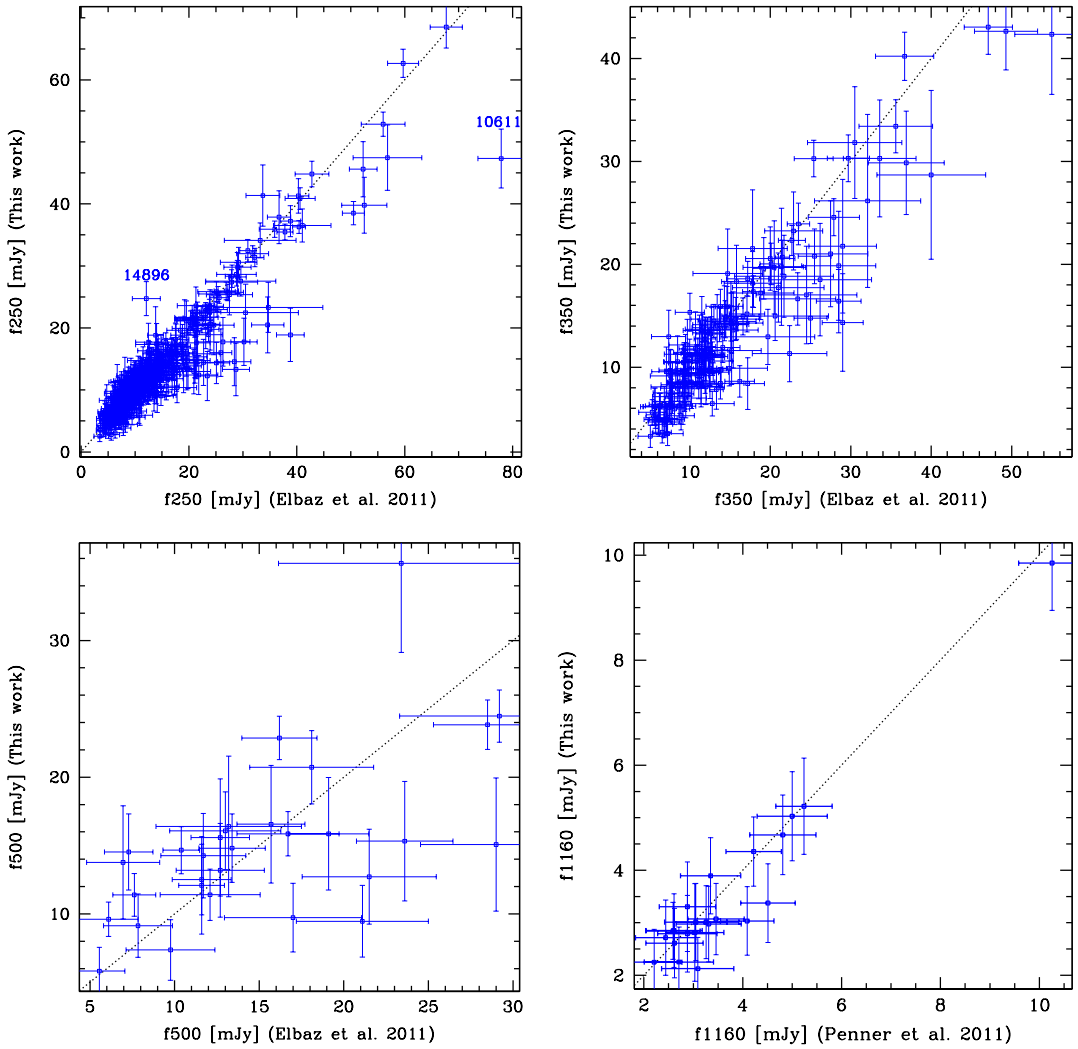
f250 [mJy] (This work)
f250 [mJy] (Elbaz et al. 2011)
14896
10611
f350 [mJy] (This work)
f350 [mJy] (Elbaz et al. 2011)
f500 [mJy] (This work)
f500 [mJy] (Elbaz et al. 2011)
f1160 [mJy] (This work)
f1160 [mJy] (Penner et al. 2011)

FIG. 17.—: The comparisons between the flux measurements in this work and literature catalogs at SPIRE 250, 350, 500 μm and 1.16 mm bands from the left panel to the right panel. The literature fluxes of the three SPIRE bands are from Elbaz et al. (2011), and the literature 1.16 mm fluxes are from Penner et al. (2011). The flux comparisons are between cross-matched common sources in our catalog and literature catalogs. Elbaz et al. (2011) used PACS detected sources as the prior sources for SPIRE band photometry, while in this work we use the near-infrared to PACS, SPIRE and radio bands SED fitting to determine the prior sources for SPIRE band photometry, and subtract the faint source flux contribution from the observed data, therefore our flux measurement tend to be smaller than literature flux values especially when the source is in highly blended situations. Two most extreme outliers are marked with their IRAC ID in the first panel, which are ID 14896 (Elbaz et al. (2011) ID 2132) and ID 10611 (Elbaz et al. (2011) ID 1512). We discuss ID 14896 in detail in Section 7.2 and the next figures. Although the offset is in the opposite, we have checked that ID 10611 has a very similar blending issue thus its figures are not shown.

SEDs. They have a very similar blending situation, and in Elbaz et al. (2011) catalog most of the SPIRE flux are attributed to ID 10611 (e.g. like ID 15027). Thus the detailed figures and SEDs are not shown here.

7.3. *Effects of varying the prior density*

Our method attempts to use all available information on galaxies in the region under consideration in order to define an ideal set of priors to fit FIR/(sub)mm data, containing the smallest possible number of useful sources. Increasing the number of priors will increase photometric errors for all galaxies on average, because of increased blending. This effect is exemplified in Fig. 20 where we show as a function of the *crowdedness* parameter the flux error (normalized to the value at low *crowdedness*) for the 100 μm and 250 μm bands. Despite these two bands having quite different numbers of priors per beam (0.3 and 1 respectively, see also Fig. 1), the normalized behavior of the flux error versus *crowdedness* is similar for the two bands. To first order the relative flux error scales proportionally to *crowdedness* , although a second order polynomial fit is a better description for *crowdedness* > 2. At 250 μm, as a result of the much larger beam, we are fitting a smaller absolute number of priors (see Fig. 20 and Table 1) that are on average at higher *crowdedness* values. The median value for the *crowdedness* is 1.64 (1.05) at 250 μm (100 μm), and the median relative flux error is similarly larger 1.63 (vs 1.02). The increase of the typical 'noise' is the price to pay for fitting all reasonable priors. We note that the effect is not so

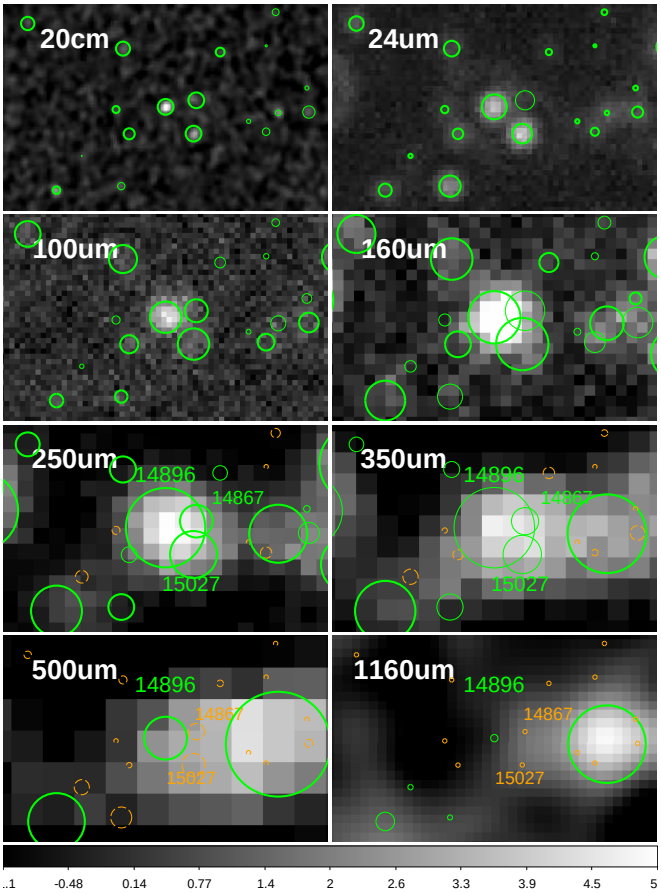

FIG. 18.—: Multi-wavelength cutouts around the outlier ID 14896 which has a significant lower flux in our catalog than in Elbaz et al. (2011). The discrepancy is because Elbaz et al. (2011) assign more flux to ID 15027. Each circle represents a 24+radio prior source (Section 2). Same as in Fig. 8, green circles are the fitted prior sources, while orange circles are the excluded ones. The circle sizes scale with flux (see caption of Fig. 8). The SEDs of the three heavily blended sources, ID 14896, ID 14867 and ID 15027 are shown in Fig. 19.

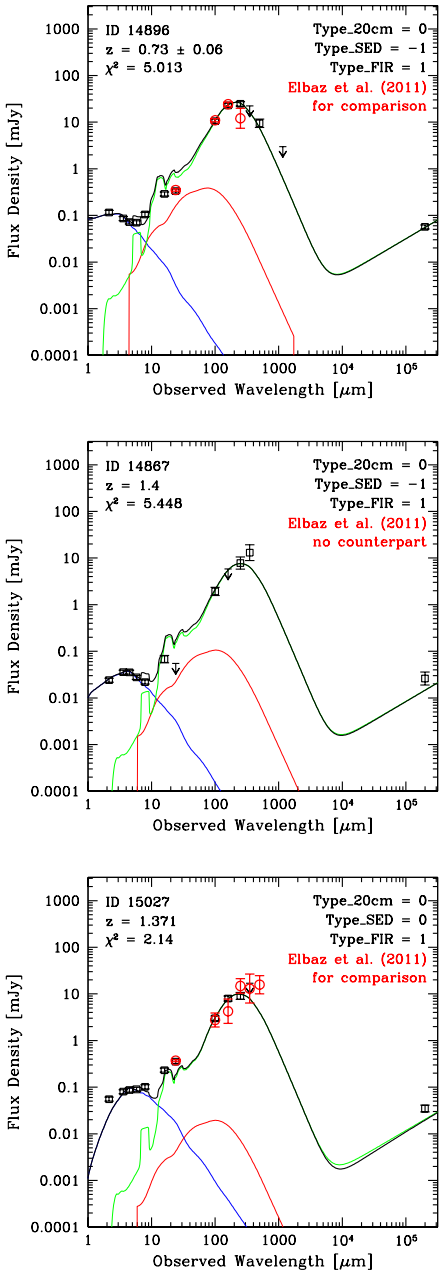

FIG. 19.—: The SEDs of 3 sources highlighted in Fig. 18, to help explain the discrepancy between our photometry results and those of Elbaz et al. (2011). We show the red data points from Elbaz et al. (2011) for comparison in the ID 14896 and ID 15027 panels. ID 14867 has no counterpart in Elbaz et al. (2011). Note that the best-fit redshift and χ^2 are shown in the upper left corner of each panel. When the source has a spectroscopic redshift, we fix the redshift to that and no error is quoted. The second and third source both have a spectroscopic redshift, thus our deblending work seems more reasonable. More details of the SED fitting are given in Section 3.1. See also caption in Fig. 9.

dramatic and errors are still quite acceptable, even if we are dealing with a density of priors approaching 1 per beam (in possible contradiction with results and discussions in Scudder et al. 2016 and Karim et al. 2013).

Fig. 5 shows that, given the information in hand, it is not possible to reduce substantially further the number density of priors without renouncing to fit objects that could be potentially fairly bright in the imaging dataset. For example, raising $f_{\rm cut}$ from 3 to 6σ would reduce $\rho_{\rm beam}$ from 1 to $\sim$0.8 only. On the other hand, if we were to reduce $f_{\rm cut}$ to 1.5σ we would reach $\rho_{\rm beam}$ of about 2. It is interesting at this point to evaluate what the impact of these choices would be. Fig. 21 shows the distribution of *crowdedness* values for the different cases. Reducing the source density from 1.0 to 0.8 per beam has indeed a fairly minor effect on the implied *crowdedness* , hence noise. Increasing the source density much beyond 1 has much stronger effects: the fraction of sources in reasonable isolation with *crowdedness* < 1.5 drops from 42% ($\rho_{\rm beam} = 1.0$) to 15% ($\rho_{\rm beam} = 2.0$), while the sources with poor measure-

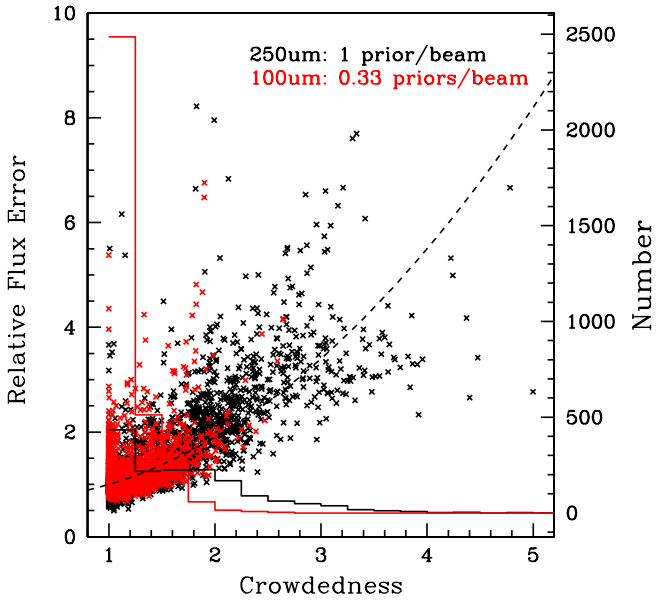

FIG. 20.—: We plot the flux error as a function of *crowdedness* (normalized for low values of *crowdedness*), with values indicated on the left-Y axis. Results from 100 μm are in red, while those from 250 μm are in black. The dashed line is a reasonable fit to both data sets going like *crowdedness* $^{0.5}$. Histograms of *crowdedness* values are also shown in the right-Y axis. At 250 μm we are fitting a smaller number of priors that are in more crowded regions on average.

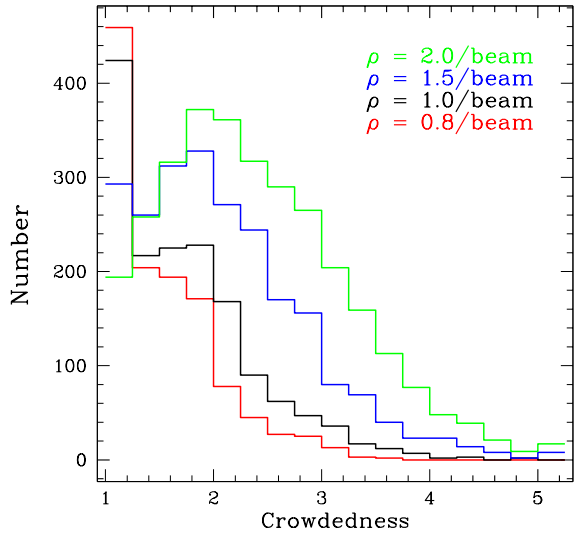

FIG. 21.—: Histograms of number of priors versus *crowdedness* for different choices of prior density $\rho_{\rm beam}$ from 0.8 to 2.0, computed here for 250 μm varying the choice of $f_{\rm cut}$.

ments due to blending with *crowdedness* >2.5 rise from 12% ($\rho_{\rm beam}=1.0$) to 41% ($\rho_{\rm beam}=2.0$). Therefore if we were to accept more sources for fitting, including some of those below $f_{\rm cut}=3\sigma$, this would result in a much increased noise and poorer performance for all objects. Staying within the limits of $\rho_{\rm beam}\sim 1$, as we have done for SPIRE in this paper, appears thus as a fairly reasonable choice.

7.4. *Robustness to source subtraction errors*

We are subtracting faint sources models from the images before running the photometric analysis. This procedure is prone to errors, as we might being over (or under) estimating their fluxes to subtract. We expect that any such error would be automatically accounted for by our simulation based approach. For example, if we were over-subtracting the fluxes of many faint sources, this would create to first order a negative (false)background, which we would detect and correct with our bias measurements that in practice establish the effective background in the data. To second order, the over-subtracted sources in the example, after zero level determination, would result in increased background fluctuations and noise, because they are likely not spatially homogeneous and their fluxes vary. This extra noise would be reflected in our simulation based calibration of uncertainties and thus accounted for in our error bars.

7.5. *Known limitations*

We are aware of a number of possible remaining problems that might still be affecting fluxes and thus their uncertainties.

One is the presence of additional sources (most often at high redshifts) which could significantly contribute flux in the data but which are not in our prior list. Such objects could spuriously boost the inferred flux (and hence lead to underestimated error bars) of other priors. Judging from the simulation this effect does not seem to be a big issue, since the distribution of $(S_{in}-S_{out})/\sigma$ ultimately closely resembles a Gaussian with width equal to 1 (see Fig. 11 and Appendix C).

Also, a fraction of photometric redshifts or even spectroscopic redshifts could be wrong. Such catastrophic outliers should be a small fraction, possibly at the level of a few percent or even below. In particular, note that in order to accept a spectroscopic redshift from the literature we require that it is in agreement within 10% in $(1+z)$ with the photometric redshift, to avoid possible wrong redshifts. Using a wrong redshift can affect SED predictions. To some extent the use of a range of dust temperatures (or $\langle U\rangle$ values more specifically in our case) moderates the impact, because of the redshift-temperature degeneracy, especially if the redshift used is not catastrophically wrong. In the latter cases, due to SED flux prediction errors, there could be a few objects that are kept for *galfit* fitting instead of being dropped (only somewhat increasing *crowdedness* , but this is probably a very negligible effect), while some objects might be erroneously dropped from fitting while still being significantly bright in the data. The latter cases could give rise to sources in the residual images if they are isolated. If they fall atop or near other priors, they may corrupt their photometry, biasing recovered fluxes high. Of course, in all cases, the impact of wrong redshifts would extend beyond simple photometric accuracy to the derivation of wrong bolometric $L_{\rm IR}$ and SFR, thus affecting the science.

Finally, another limitation is that we are using *galfit* with a constant background. Possible background variations would act as increased noise. Carefully accounting for background variations could improve photometric uncertainties, but is limited by our knowledge of PSF wings, and of course by the very large beams in the SPIRE and (sub)mm imaging. We attempted a correction of background variations at 24 μm and 16 μm, where the beam is still fairly small and manageable. Dealing with this for PACS and SPIRE imaging is beyond the scope of the present work.

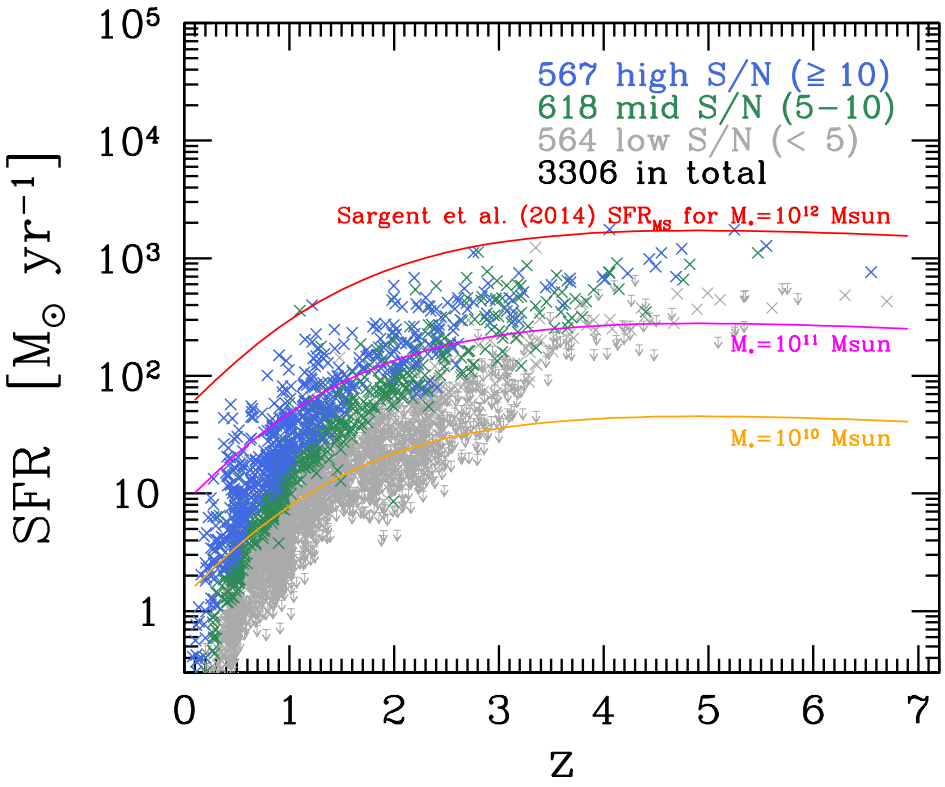

FIG. 22.—: The SFR versus redshift diagram for all 3306 sources in the 24+radio catalog (Section 2.4). SFRs are computed from the integrated 8-1000 μm infrared luminosity of their FIR+mm SEDs, SFR $= L_{\rm IR}/1\times10^{10}\,{\rm M}_\odot\,{\rm yr}^{-1}$, assuming Chabrier IMF (Chabrier 2003). Colors indicate the combined S/N over FIR+mm bands (see Equation 2). We show the empirical tracks of the MS galaxy SFR as a function of redshift at three representative MS stellar masses: $M_*=10^{12}\,{\rm M}_\odot$, $10^{11}\,{\rm M}_\odot$ and $10^{10}\,{\rm M}_\odot$, according to Sargent et al. (2014) who compiled literature SFR and M_* data and derived empirical MS correlation (i.e. SFR as a function of M_* and z).

8. RESULTS AND DISCUSSION

In this final section we use the FIR/(sub)mm catalog developed in this work to study the IR emission of high redshift galaxies and to provide an estimate of the SFR density in the Universe, up to high redshift.

In order to evaluate whether a source is detected in the FIR+mm we adopt a simple approach considering the combined S/N over PACS, SPIRE, 850 μm and 1.16 mm bands:

$$\begin{aligned}{\rm S/N}^2_{\rm FIR+mm} = {\rm S/N}^2_{100\,\mu{\rm m}} + {\rm S/N}^2_{160\,\mu{\rm m}} + {\rm S/N}^2_{250\,\mu{\rm m}} + \\ {\rm S/N}^2_{350\,\mu{\rm m}} + {\rm S/N}^2_{500\,\mu{\rm m}} + {\rm S/N}^2_{850\,\mu{\rm m}} + {\rm S/N}^2_{1.16\,{\rm mm}}\end{aligned} \quad (2)$$

Our ${\rm S/N}_{\rm FIR+mm}$ definition is equivalent to a Chi-Squared field whose expectation value (in presence of pure noise) for 7 bands being added, is equal to $\sqrt{7}\approx2.6$ and the probability to have ${\rm S/N}_{\rm FIR+mm}\geq5$ is 7×10^{-4} for pure Gaussian random fields (Bloomfield et al. 2016). In such an ideal case, this would produce at most a couple of spurious IR detection from our starting pool of prior positions. Among the 3306 24+radio sources, 1185 are detected with ${\rm S/N}_{\rm FIR+mm}\geq5$, and 567 are very significantly detected with ${\rm S/N}_{\rm FIR+mm}\geq10$.

While we have applied our photometric technique to the whole GOODS-N area, we focus in the reminder of the paper on those objects lying in the central 134 arcmin^2 region of GOODS-N (hereafter *goodArea*), avoiding outer regions where the instrumental noise at 24 μm starts to rise (and hence the 24 μm prior sources will be less complete). This *goodArea* contains 862 ${\rm S/N}_{\rm FIR+mm}\geq5$ sources and 427 ${\rm S/N}_{\rm FIR+mm}\geq10$ sources.

8.1. *Redshift and SFR distributions*

In Fig. 22, we present the dust-obscured SFR versus redshift diagram for all the 3306 24+radio sources. The SFR are derived from the pure dust component IR luminosity over 8–1000 μm (excluding AGN torus components as derived from our SED fitting, see Section 3.1). Among all the detected sources (hereafter FIR+mm sources), 119 sources have $z\geq2.5$ (FIR+mm SED based photometric redshift or spectroscopic redshift when available), 71 at $z\geq3$ and 20 at $z\geq4$. Within the *goodArea* we find 82 sources at $z\geq2.5$, 50 at $z\geq3$ and 13 at $z\geq4$.

In Fig. 22 we indicate the SFRs of typical MS galaxies with three stellar masses ($M_*=10^{12}\,{\rm M}_\odot$, $10^{11}\,{\rm M}_\odot$ and $10^{10}\,{\rm M}_\odot$ respectively), computed with the Eq. (A1) of Sargent et al. (2014). This FIR+mm sample is clearly non-uniform in either SFR or stellar mass. At lower redshift (e.g. $z<1$), the limits of the SFR and stellar mass both rise quickly. At $z<1$, the GOODS-N FIR+mm data can detect emission from MS galaxies with $M_*<10^{10}\,{\rm M}_\odot$, but at $z>1$ all detected galaxies are more massive. At higher redshift (e.g. $z>3$), the sample is clearly biased towards high SFRs and stellar masses ($M_*>10^{11}\,{\rm M}_\odot$). Both the effective limits of SFR and stel-

TABLE 2: GOODS-N "Super-deblended" Photometry Catalog (Example)

ID	R.A.	Dec.	z	f_{500}	$\sigma_{f_{500}}$	S/N	$\log M_*$	SFR	$\sigma_{\rm SFR}$	goodArea	T_{20cm}	T_{SED}
(1)	(2)	(3)	(4)	(5)	(6)	(7)	(8)	(9)	(10)	(11)	(12)	(13)
11499	189.2606049	62.2172966	4.496	10.07	1.704	20.7	10.64	848.7	42.61	1	0	-1
564	189.2994995	62.3700371	4.055	47.47	7.5	20.0	9.95	1751	87.45	1	0	1
2592	189.3670044	62.3222733	4.744	14.81	2.496	18.0	···	1200	66.56	1	0	-1
3532	189.3077393	62.3073006	3.988	9.501	1.972	16.8	9.51	694.4	179.3	1	1	-1
16332	189.2442017	62.1585388	3.501	10.88	4.73	16.3	9.76	592.9	150.9	1	0	0
14914	188.9597931	62.1782951	5.245	20.73	2.68	15.9	10.01	1744	142.2	0	0	-1
4990	189.1330261	62.2873993	4.229	12.51	2.576	15.3	10.65	741.5	48.39	1	0	1
15289	188.9900818	62.1734276	3.075	9.137	2.318	15.3	10.31	354.6	24.97	0	0	1
4500	189.4094086	62.2934532	3.190	14.53	2.789	15.0	10.15	292.3	19.5	1	0	1
9053	189.0358124	62.2431564	3.446	14.55	1.701	14.9	9.95	564.8	96.91	1	0	-1
18911	189.1133881	62.1015778	4.551	31.58	4.512	14.4	10.32	1109	94.1	0	0	0
1159	189.2011871	62.3519135	3.234	14.55	5.254	13.5	9.31	514.9	38.14	0	0	-1
17624	189.0368347	62.1344681	3.683	12.33	4.628	12.8	9.92	626.8	81.45	0	0	-1
13107	189.1156006	62.1996002	3.608	9.185	1.986	12.3	10.48	399.4	124.8	1	0	-1
16810	189.0555725	62.1504669	3.138	9.826	1.613	12.1	9.64	352.2	46.74	0	0	-1
17381	189.2108612	62.1394119	3.100	6.149	13.03	11.6	10.14	461.5	178.4	1	0	0
11758	189.0360870	62.2141380	4.689	9.223	1.675	11.4	9.13	697.2	61.23	1	0	-1
18603	189.0650787	62.1119728	3.678	12.26	8.522	11.2	10.72	671.8	122.4	0	0	0
18392	189.0688019	62.1174965	4.434	15.46	10.77	10.9	11.21	985.2	91.32	0	0	-1
1735	189.1885529	62.3387527	4.007	9.722	2.509	10.8	10.67	659.4	124.8	1	0	-1
12646	189.1147461	62.2050095	6.551	0.2036	2.633	10.6	9.47	760.8	71.82	1	0	0
7959	189.0670776	62.2537880	3.190	13.06	11.92	10.4	9.81	749.5	247.5	1	0	-1
9710	189.1391907	62.2356987	5.551	11.09	2.387	10.4	10.07	1273	375.3	1	0	0
6006	189.4907074	62.2752075	3.130	7.215	4.518	10.4	9.97	438.9	125	1	0	0
13517	189.2389984	62.1951675	3.134	···	···	10.2	10.55	291	28.43	1	0	0

Table 2 is published in its entirety in the machine-readable format. A portion is shown here for guidance regarding its form and content. Here we show a few example columns and a few example $S/N_{\rm FIR+mm} \geq 10$ sources at $z \geq 3$ (sorted by the $S/N_{\rm FIR+mm}$). Column (1), (2) and (3) are the IRAC catalog from GOODS-*Spitzer* Legacy Program (see Section 2). Column (4) is the spectroscopic redshift when available, otherwise the FIR+mm SED fitting photometric redshift. Column (5) and (6) are flux and uncertainty in unit of mJy. Column (7) is the FIR+mm combined S/N in Equation 2. Column (8) is the stellar mass from 3D-HST program or Pannella et al. (2015), converted to Chabrier IMF when needed. Column (9) and (10) are the SFR and uncertainty from FIR+mm SED fitting (see Fig. 22 caption for deriving SFR from $L_{\rm IR}$). Column (11) is the "goodArea" parameter, equals 1 if the source is in the inner lower r.m.s. area in 24 μm (has deeper prior catalog for surrounding sources), otherwise 0 (has shallower or even incomplete prior catalog for surrounding sources). Column (12) is the "Type_20cm" parameter, equals 1 if the source is classified as radio excess and its radio data point is not fitted in SED fitting, otherwise 0. Column (13) is the "Type_SED" parameter, equals 1 if the source is classified as starburst type (its SED is fixed to using starburst templates), or -1 if classified as main-sequence type (its SED is fixed to using main-sequence templates), otherwise 0 (allowing fitting all SED templates).

lar mass have risen by one to two orders of magnitudes (e.g. compared to $z \sim 1$), which is expected for flux limited surveys in the FIR (the Malmquist bias in SFR would be less for a pure (sub)mm selection, but the deepest probed data in our case is *Herschel*).

We present FIR+mm catalog in Table 2. The full machine-readable version can be accessed via the on-line journal; here we only show a few important columns whose descriptions are in the caption.

8.2. *Stellar mass and SFR properties*

In Fig. 23 we compare our sample with empirical MS correlations in all redshift bins up to redshift 6. Only *goodArea* FIR+mm sources with stellar masses available from 3D-HST or Pannella et al. (2015) are shown here (7 FIR+mm sources are dropped for lack of these estimates). The differences between the three MSs considered here (from Sargent et al 2014, Schreiber et al 2015 and Bethermin et al 2015) are relatively large at both $z < 1.5$ and $z > 4$, but the different estimates are more consistent at $1.5 < z < 4$. In the highest redshift bins, the Sargent et al. (2014) MS has the lowest SFR normalization. The difference between this MS and the other two can reach a factor of 3 at $10^{11.5}\,M_\odot$ and $z \sim$4–6, where global uncertainties still prevent a solid derivation of the MS level.

Red symbols in each panel are sources classified as strong starbursts during the SED fitting step (Section 3.1) using Sargent et al. (2014) MS. They are relatively rare, and most of them are less massive, with $M_* \lesssim 10^{10.5}\,M_\odot$. The fraction of SBs in this sample is 9.8% at $1 < z < 4$, intermediate between the fraction of 30-50% for SMG-like selection at the highest luminosities and the fraction of 2% to 3% derived for the stellar mass selected sample at $1.5 < z < 2.5$ (complete to $M_* \geq 10^{10}\,M_\odot$; Rodighiero et al. 2011[29]).

The shaded area in each panel indicates the stellar mass range over which the sample is incomplete (evaluated by analyzing star-forming galaxy SMFs in the next section). This shows that our FIR+mm sample can already reach a high completeness at the characteristic stellar mass $M^*_{\rm star}$ in the 4 lowest redshift bins, where the $M^*_{\rm star}$ of star-forming galaxies are estimated to be $10^{10.81}\,M_\odot$ (Kroupa IMF) at $0.2 < z < 0.5$ by (Muzzin et al. 2013) (or $10^{10.60}\,M_\odot$ in Ilbert et al. 2013, or $10^{10.26}\,M_\odot$ in Davidzon et al. 2017, both in Chabrier IMF), and are not increasing much in the $2.0 < z < 2.5$ bin (by only 0.01, 0.13 and 0.19 dex in Muzzin et al. 2013, Ilbert et al. 2013 and Davidzon et al. 2017 respectively).

At $z > 3$, the $M^*_{\rm star}$ varies between $10^{10.74-11.56}\,M_\odot$ (David-

[29] Their definition of SB is the same as we adopted in this work, i.e. $\log {\rm SFR} - \log {\rm SFR_{MS}} > 0.6$ dex

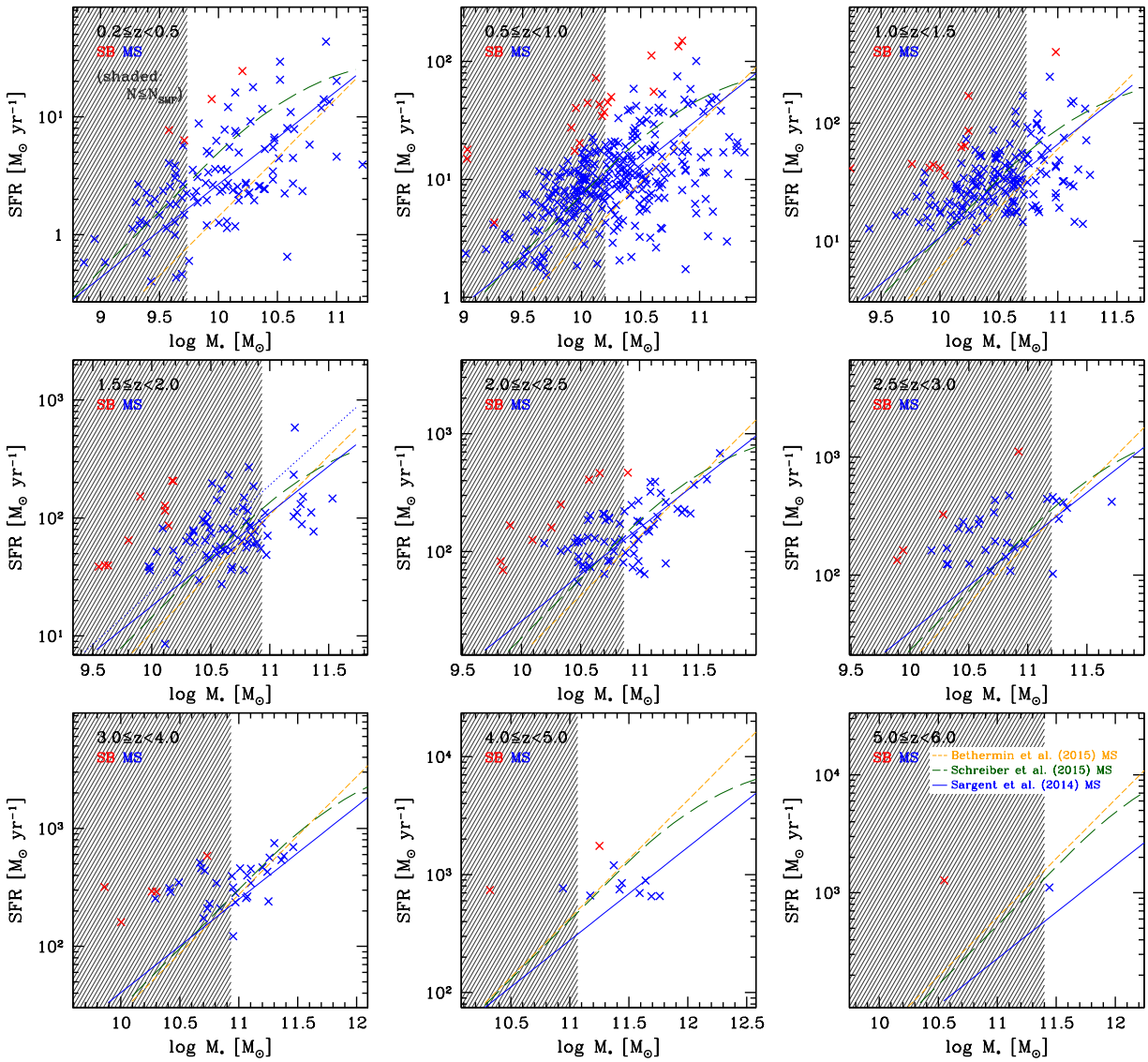

FIG. 23.—: The dust-obscured SFR versus stellar mass M_* diagram for our FIR+mm sample in 9 redshift bins: $0.2 \leq z_{\rm phot} < 0.5$, $0.5 \leq z_{\rm phot} < 1.0$, $1.0 \leq z_{\rm phot} < 1.5$, $1.5 \leq z_{\rm phot} < 2.0$, $2.0 \leq z_{\rm phot} < 2.5$, $2.5 \leq z_{\rm phot} < 3.0$, $3.0 \leq z_{\rm phot} < 4.0$, $4.0 \leq z_{\rm phot} < 5.0$ and $5.0 \leq z_{\rm phot} < 6.0$. All values assume Chabrier IMF (Chabrier 2003). Red symbols are sources classified as SBs during our SED fitting (Section 3.1) according to their SFR, S/N of SFR and the distance to the MS of Sargent et al. (2014), while blue symbols are all other sources. The shaded area indicates where our FIR+mm sample becomes incomplete (see the evaluation of incompleteness in Section 8.3) according to our next stellar mass histogram analysis in Fig. 24. Three literature MSs are compared in each panel: blue solid line is the Sargent et al. (2014) MS, green long-dash line is the Schreiber et al. (2015) MS, while the yellow dashed line is the Béthermin et al. (2015) MS. Note that the discrepancies between the three empirical MSs are small at lower redshift bins but not for the highest redshift bin, where the difference can be as large as a factor of 3. The Sargent et al. (2014) MS has the lowest SFR.

zon et al. 2017; Grazian et al. 2015; Ilbert et al. 2013; Muzzin et al. 2013). Therefore the FIR+mm sample can only probe a minority of galaxies at the high mass end of SMF.

8.3. *Comparing with literature SMFs*

To evaluate the incompleteness of our FIR+mm sample we consider sources in each redshift bin, further dividing them into bins of stellar masses in Fig. 24, and compare their distribution with various star-forming galaxy SMFs from the literature.

The literature SMFs are convolved to a common stellar mass uncertainty (σ_{M_*}, see labels in each panel) so as to account for measurement errors to directly compare with our observed stellar mass histograms (blue and red histograms in the figure, representing the full FIR+mm sample and the SB sub-sample respectively). This is done by first using the Eddington bias-corrected (i.e. intrinsic) SMFs in these literature, then convolving with a common σ_{M_*} (which is redshift-dependent), following the approach described in Appendix A of Ilbert et al. (2013) (except for Song et al. (2016) where the authors have not done that correction). We multiply by the *goodArea* co-moving volume to convert SMF (in units of

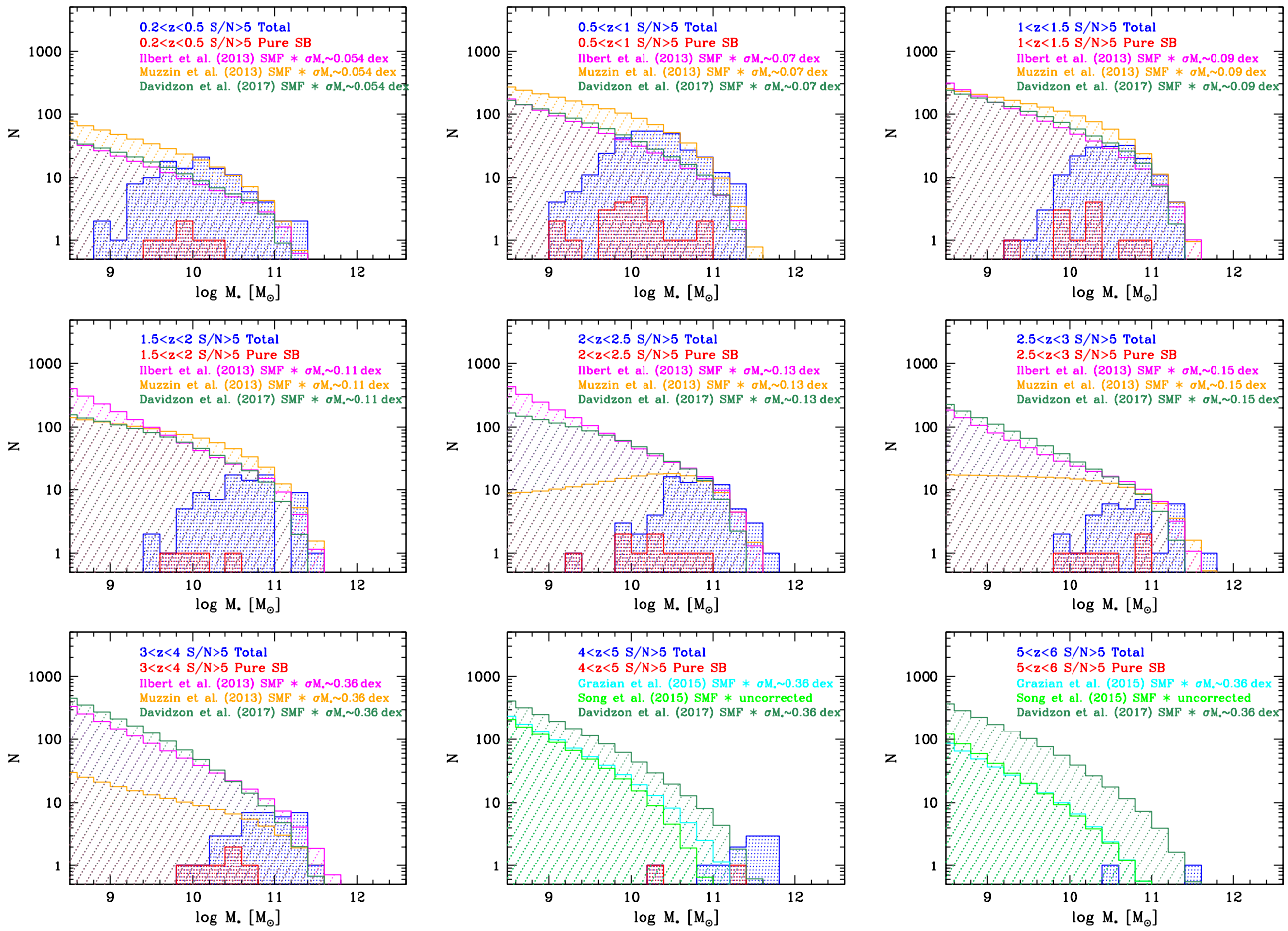
0.2<z<0.5 S/N>5 Total
0.2<z<0.5 S/N>5 Pure SB
Ilbert et al. (2013) SMF * σM,~0.054 dex
Muzzin et al. (2013) SMF * σM,~0.054 dex
Davidzon et al. (2017) SMF * σM,~0.054 dex
0.5<z<1 S/N>5 Total
0.5<z<1 S/N>5 Pure SB
Ilbert et al. (2013) SMF * σM,~0.07 dex
Muzzin et al. (2013) SMF * σM,~0.07 dex
Davidzon et al. (2017) SMF * σM,~0.07 dex
1<z<1.5 S/N>5 Total
1<z<1.5 S/N>5 Pure SB
Ilbert et al. (2013) SMF * σM,~0.09 dex
Muzzin et al. (2013) SMF * σM,~0.09 dex
Davidzon et al. (2017) SMF * σM,~0.09 dex
1.5<z<2 S/N>5 Total
1.5<z<2 S/N>5 Pure SB
Ilbert et al. (2013) SMF * σM,~0.11 dex
Muzzin et al. (2013) SMF * σM,~0.11 dex
Davidzon et al. (2017) SMF * σM,~0.11 dex
2<z<2.5 S/N>5 Total
2<z<2.5 S/N>5 Pure SB
Ilbert et al. (2013) SMF * σM,~0.13 dex
Muzzin et al. (2013) SMF * σM,~0.13 dex
Davidzon et al. (2017) SMF * σM,~0.13 dex
2.5<z<3 S/N>5 Total
2.5<z<3 S/N>5 Pure SB
Ilbert et al. (2013) SMF * σM,~0.15 dex
Muzzin et al. (2013) SMF * σM,~0.15 dex
Davidzon et al. (2017) SMF * σM,~0.15 dex
3<z<4 S/N>5 Total
3<z<4 S/N>5 Pure SB
Ilbert et al. (2013) SMF * σM,~0.36 dex
Muzzin et al. (2013) SMF * σM,~0.36 dex
Davidzon et al. (2017) SMF * σM,~0.36 dex
4<z<5 S/N>5 Total
4<z<5 S/N>5 Pure SB
Grazian et al. (2015) SMF * σM,~0.36 dex
Song et al. (2015) SMF * uncorrected
Davidzon et al. (2017) SMF * σM,~0.36 dex
5<z<6 S/N>5 Total
5<z<6 S/N>5 Pure SB
Grazian et al. (2015) SMF * σM,~0.36 dex
Song et al. (2015) SMF * uncorrected
Davidzon et al. (2017) SMF * σM,~0.36 dex
N
log M* [M⊙]

FIG. 24.—: The stellar mass histograms of FIR+mm detected sources within GOODS-N 134 arcmin^2 *goodArea* in 9 redshift bins (blue histograms). The red histograms indicate the sources classified as pure starbursts (SB) in our SED fitting. The empirical stellar mass functions (SMFs) of Ilbert et al. (2013), Muzzin et al. (2013), Grazian et al. (2015), Song et al. (2016) and Davidzon et al. (2017) are shown as the magenta, yellow, cyan, light green and dark green curves respectively. The SMFs are for star-forming galaxies, converted to Chabrier IMF when needed, and convolved with typical stellar mass uncertainties (σ_{M_*}) as indicated by the labels in each panel, following the Appendix A of Ilbert et al. (2013) (except for Song et al. (2016) which is the directly observed one). Shaded area are colored in the same way. The SMFs of Ilbert et al. (2013) and Muzzin et al. (2013) extend up to redshift 4, while that of Grazian et al. (2015), Song et al. (2016) and Davidzon et al. (2017) probe higher redshifts (Davidzon et al. 2017 dose not fully cover the last redshift bin; we show a simple linear redshift extrapolated SMF).

number per volume) to the absolute number of galaxies within each stellar mass bin and each redshift bin.

The literature SMFs do not always agree with each other, but in general, they agree with our observed histograms in Fig. 24 up to the $3 < z < 4$ bin without doing any fitting. The Muzzin et al. (2013) non-fixed-slope SMF lead to large discrepancies at the low-mass end than other SMFs at $z > 2$ (their fixed-slope SMFs agree obviously better only at $2 < z < 3$ bins hence are not shown).

Note that the SMF of Davidzon et al. (2017) does not fully cover our highest redshift bin. Here we did linearly extrapolation with their $3.5 < z < 4.5$ and $4.5 < z < 5.5$ data to the $5 < z < 6$ bin for purpose of comparison. Because their SMF is even higher at $4.5 < z < 5.5$ than at $3.5 < z < 4.5$, the extrapolated SMF is also obviously higher.

To evaluate the stellar mass range (shown as the shaded-area in Fig. 23) over which our sample becomes incomplete in each redshift bin, we estimate at which value of stellar mass the number of observed galaxies in our sample starts to be substantially smaller than the number indicated by each SMF.

In the last 3 redshift bins of Fig. 24, our FIR+mm sample tends to have more galaxies at the highest masses than would be predicted by the literature SMFs. In the $3.0 < z < 4.0$ panel, the excess is not so obvious, but in the $4.0 < z < 5.0$ panel, our FIR+mm sample has 8 more sources than what is predicted by the Grazian et al. (2015) and Song et al. (2016) SMFs, or 6 more sources than predicted by the Davidzon et al. (2017) SMF. Note that in the GOODS-N field there is a well known $z = 4.055$ proto-cluster including three FIR+mm sources in this work: GN20, GN20.2a and GN20.2b (Daddi et al. 2009; Tan et al. 2014). Thus small number statistics is already becoming an important factor in these redshift bins.

Moreover, Grazian et al. (2015) discussed the importance of cosmic variance between GOODS-S and UDS fields in their Fig. 3. The SMF derived from UDS sources is much higher than the SMF derived from GOODS-S sources at the high-mass end, and the former one agrees better with the Ilbert et al. (2013) and Muzzin et al. (2013) SMFs. Hence cosmic

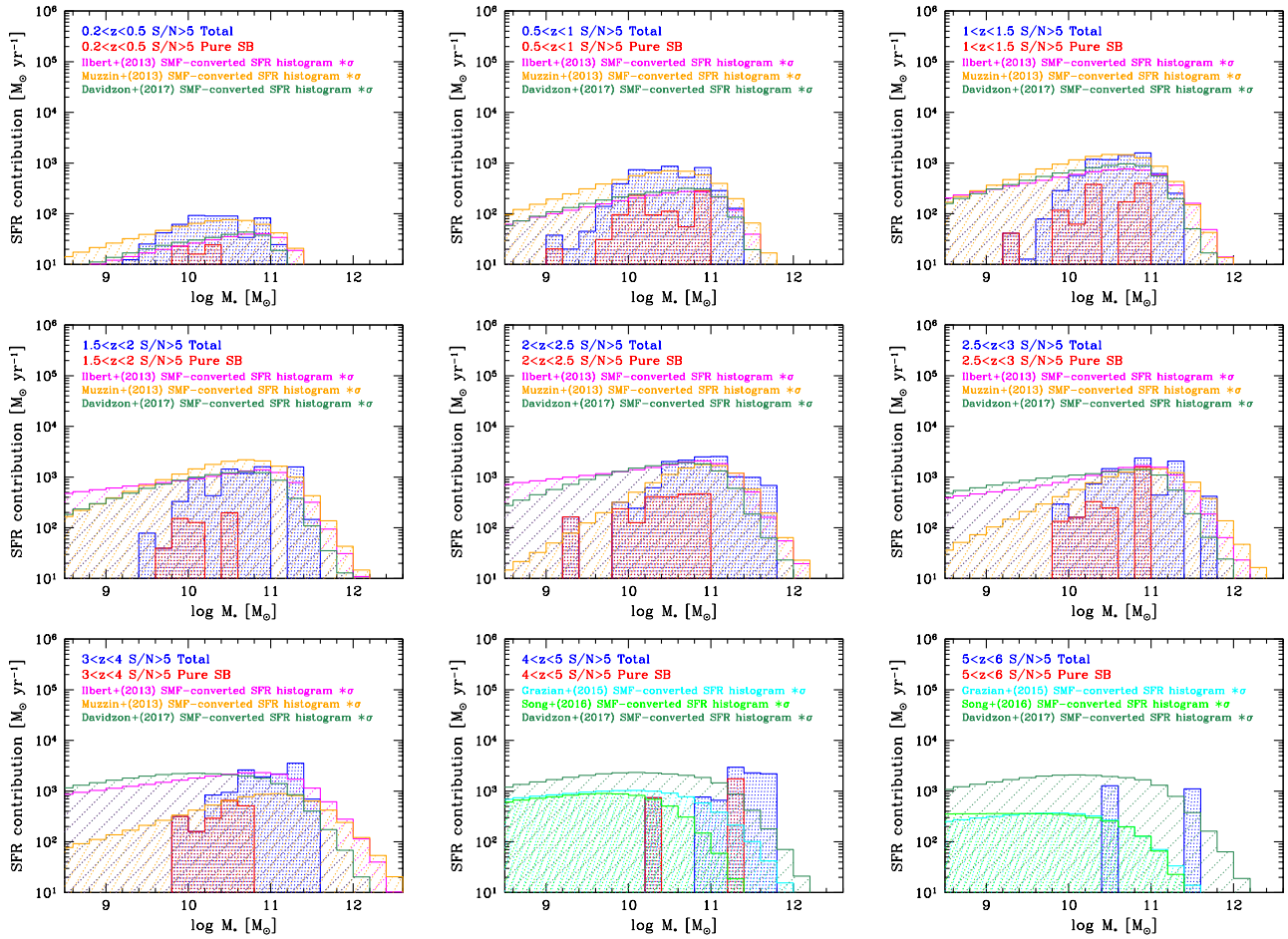

FIG. 25.—: The star formation rate (SFR) contribution in bins of stellar mass (M_*) for the FIR+mm detected sources in 9 redshift bins. The FIR+mm sample is within GOODSN 134 arcmin^2 area. The blue histogram represents the sum of SFRs for sources in each stellar mass bin. The red histogram is for sources classified as pure starburst. The literature SMFs are the same as Fig. 24. We convert the SMF histograms into SFR histograms by multiplying the specific-SFR defined by MS of Sargent et al. (2014). See text in Section 8.5.

variance may also be responsible for the excess in the highest redshift bins found in this work.

Our forthcoming work in the 2 square degree COSMOS field with the same approach (S. Jin et al 2017, in preparation) will be able to provide information less affected by cosmic variance, in the high redshift bins.

8.4. *Comparing with SFR histograms*

In Fig. 25, we further analyze the SFR contributions of our sample of galaxies in bins of stellar mass. We divide our sources into several stellar mass bins (from $\sim 10^{8.5}\,M_\odot$ to $\sim 10^{12.5}\,M_\odot$ with intervals of 0.2 dex, as in the previous section), then compute the sum of SFRs in each bin.

For literature SMFs, we first multiply by the co-moving volume to obtain the absolute number of galaxies, then convert the stellar mass of each stellar mass bin to SFR by applying the MS correlations, and finally multiply the SFR by the absolute number of galaxies to get the SFR contribution for each stellar mass bin ($\int \mathrm{SMF} \times \mathrm{SFR_{MS}}$). In this way, we are able to see how does the SFR of this FIR+mm sample distribute as a function of the stellar masses, and to what fraction this sample contributes in SFR to the whole population of star-forming galaxies at each redshift up to 6. Here we show the results computed with the Sargent et al. (2014) MS, but the main results will not change substantially if the other two MSs (Béthermin et al. 2015; Schreiber et al. 2015) were applied.

The shape of these SMF-converted SFR histograms usually displays a peak around $M^*_{\rm star}$. In the three lowest redshift bins, the Muzzin et al. (2013) SMF-converted SFR has the best agreement with our sample, but it is suggesting a higher SFR contribution from the most massive end ($M_* > 10^{11.0}\,M_\odot$), where we might miss some galaxies due to the limited volume of our survey. The Davidzon et al. (2017) SMF-converted SFR fits well the high-mass end but is overall too low. The Ilbert et al. (2013) SMF-converted SFR is in between. The FIR+mm sample is already accounting for most of the global SFR density at these redshifts. In the intermediate redshift bins ($1.5 < z < 4.0$), the Ilbert et al. (2013) SMF-converted SFR fits better the normalization. The Muzzin et al. (2013) one fits better the shape at the low-mass end, which is probably due to the different stellar mass limit in Muzzin et al. (2013) (e.g. $M_{*,95\%\,\rm lim.} = 10^{10.54}\,M_\odot$ at $2 < z < 2.5$) than in Ilbert et al. (2013) (e.g. $M_{*,90\%\,\rm lim.} = 10^{10.01}\,M_\odot$ at $2 < z < 2.5$), keeping in mind the current difficulties in determining the low-mass end slope of SMFs (see Appendix C of Muzzin et al. 2013). In the last two redshift bins, the Davidzon et al. (2017)

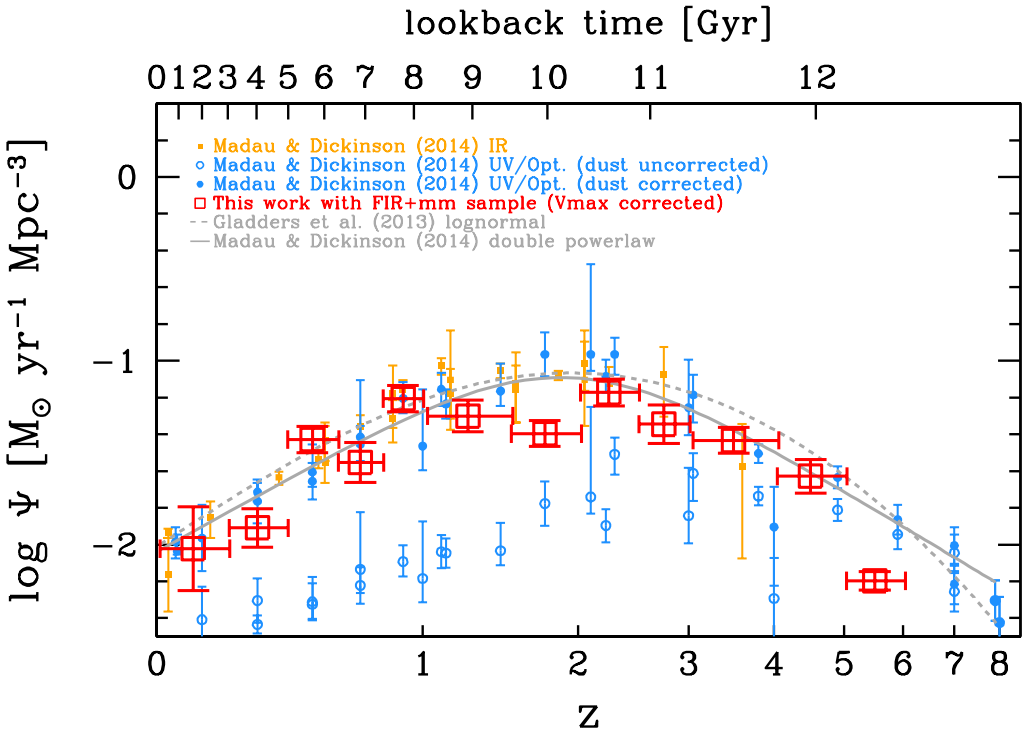
lookback time [Gyr]
0 1 2 3 4 5 6 7 8 9 10 11 12
Madau & Dickinson (2014) IR
Madau & Dickinson (2014) UV/Opt. (dust uncorrected)
Madau & Dickinson (2014) UV/Opt. (dust corrected)
This work with FIR+mm sample (Vmax corrected)
Gladders et al. (2013) lognormal
Madau & Dickinson (2014) double powerlaw
log Ψ [M⊙ yr⁻¹ Mpc⁻³]
0
−1
−2
0 1 2 3 4 5 6 7 8
z

FIG. 26.—: The SFR densities (Ψ) of our FIR+mm sample (red symbols) and the comparisons with literature cosmic SFR densities. The X direction error bars represent the redshift bin ranges, and Y direction error bars represent the uncertainties. See details of the measurements (i.e. $1/V_{max}$ and bootstrapping methods) in Section 8.5. Yellow solid squares are the IR-based measurements from Madau & Dickinson (2014). Blue solid circles are the UV/optical-based dust attenuation corrected measurements, while the blue open circles are UV/optical-based measurements without dust attenuation correction. The dashed gray curve is the best-fit log-normal function of Gladders et al. (2013), while the solid gray curve is the best-fit double power-law function given in Madau & Dickinson (2014).

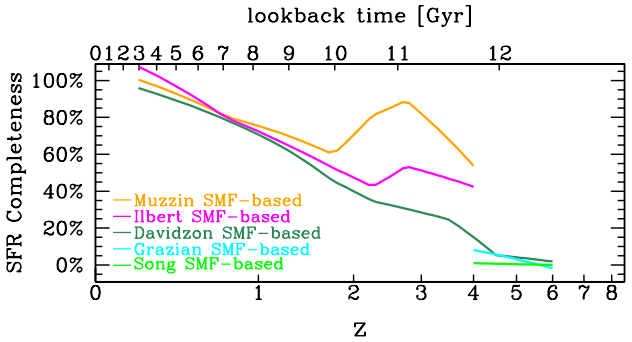

FIG. 27.—: The completeness in SFR for our FIR+mm sample, estimated based on fitting/re-normalizing the SMFs. See details in Section 8.6 and Appendix Fig. D51.

SMF-converted SFR seems the most reasonable one, but the SFR excess of our FIR+mm sample is still obvious.

8.5. *Comparing with literature cosmic SFR densities*

At redshift above 2–3, our understanding of the cosmic SFR density is still largely limited to UV- and optical-based studies. Direct knowledge of dust-obscured star formation at such high redshift, i.e. from the FIR to mm data, mainly comes from a small number of rarest and most ultraluminous galaxies, leaving considerable uncertainty about the UV-based cosmic SFR densities (Madau & Dickinson 2014). Recent attempts to derive dust-obscured SFR densities have been pushed to redshift $3.0 < z < 4.2$ by Gruppioni et al. (2013) and to redshift 6 by Rowan-Robinson et al. (2016).

In this and the next section, we first directly compute the inferred SFR densities from our FIR+mm *goodArea* sample up to redshift 6 (Fig. 26) and compare with literature cosmic SFR densities results, then estimate the incompleteness corrections with literature SMFs (Fig. 27). Finally, we repeat the comparison after correcting for incompleteness in our sample (Fig. 28).

We use the non-parametric $1/V_{max}$ method (Schmidt 1968) to estimate the SFR density of our FIR+mm sample in each redshift bin so as to eliminate the Eddington bias (e.g. Appendix A of Ilbert et al. 2013) We compute for each source the farthest redshift z_{max} at which it can still be detected in our catalog (i.e. $S/N_{FIR+mm} \geq 5$). Then for each redshift bin (lower and higher boundaries are z_1 and z_2), we compute the co-moving volume for each source (V_{max}) from z_1 to

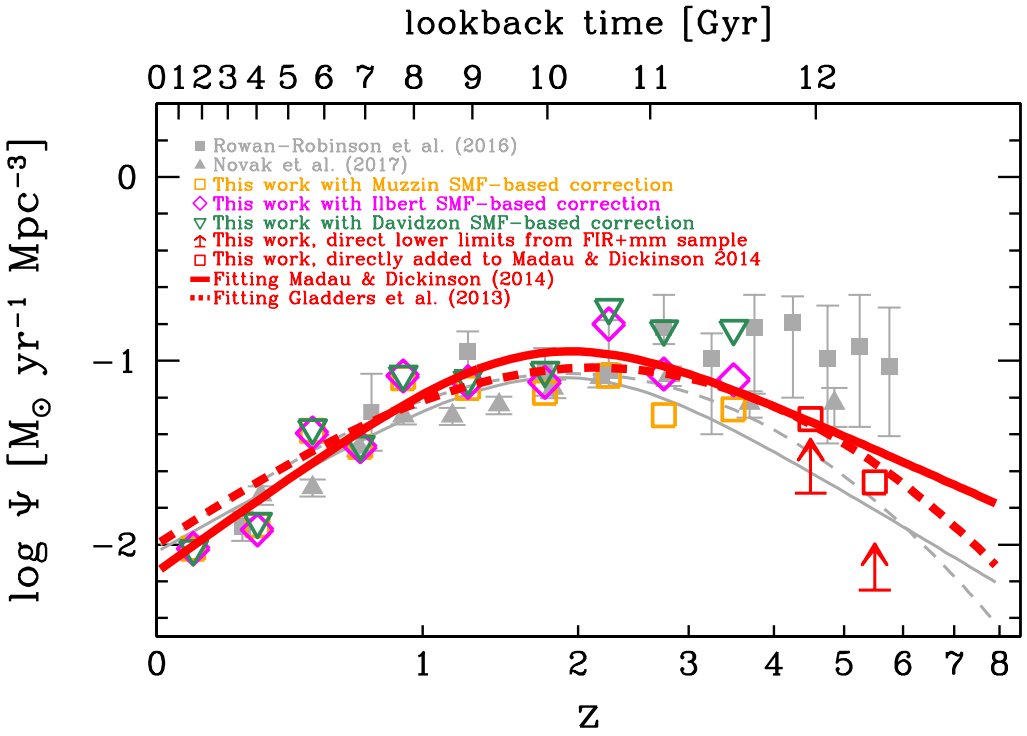
lookback time [Gyr]
0 1 2 3 4 5 6 7 8 9 10 11 12
Rowan−Robinson et al. (2016)
Novak et al. (2017)
This work with Muzzin SMF−based correction
This work with Ilbert SMF−based correction
This work with Davidzon SMF−based correction
This work, direct lower limits from FIR+mm sample
This work, directly added to Madau & Dickinson 2014
Fitting Madau & Dickinson (2014)
Fitting Gladders et al. (2013)
log Ψ [M⊙ yr⁻¹ Mpc⁻³]
0
−1
−2
0 1 2 3 4 5 6 7 8
z

FIG. 28.—: The incompleteness-corrected cosmic SFR densities based on our FIR+mm sample. We estimate the incompleteness using literature SMFs (Davidzon et al. 2017; Grazian et al. 2015; Ilbert et al. 2013; Muzzin et al. 2013; Song et al. 2016) and based on the MS correlation fitted by Sargent et al. (2014). At $z < 4$, we show the incompleteness-corrected cosmic SFR density derived from each SMF-based correction by different colors and symbols (see labels in the figure). At $z > 4$, we show lower limits as well as the added total cosmic SFR density of our FIR+mm sample and the Madau & Dickinson (2014) UV-based sample. See details in Section 8.6. The two gray color empirical curves are the same as in Fig. 26, but here we also show two red thick curves which are our new best-fit to all the colored data points (details in the text). All values are assumed Chabrier IMF (or converted to Chabrier IMF when needed).

$min(z_{max}, z_2)$ (i.e. the smaller one, e.g. Pozzetti et al. 2003). Then the SFR density of this sample is the sum of all individual SFR$/V_{max}$ in each redshift bin. To account for more realistic uncertainties, we compute SFR$/V_{max}$ in a bootstrapping method: we randomly select the same number of sources in each redshift bin but allow duplication, then repeat 1000 times to compute the mean and rms (i.e. the uncertainty of the measured SFR density).

In Fig. 26, the SFR densities directly measured from our observed sample are represented, and compared to the results of Madau & Dickinson (2014) and Gladders et al. (2013). The wiggles up and down from bin to bin at $0 < z < 3$ (where we expect a smooth redshift dependence) suggest of order of $\sim$0.2 dex of total errors in our determinations, probbaly dominated by cosmic variance (although note that the bins are not equal in the co-moving volume).

We compare our direct SFR densities with the recent results of Bourne et al. (2017). Based on 230 arcmin^2 (almost twice the area of this work) SCUBA-2 450 μm image data ($1\sigma \sim 1.0$ mJy) and other multi-wavelength data, Bourne et al. (2017) derived the SFR densities of a stellar mass complete sample ($M_* > 10^{10}\,M_\odot$) within the redshift range of $0.5 < z < 6$. In their highest redshift bin ($4 < z < 6$), they find that the FIR-only SFR density for this sample is about $10^{-1.9}\,M_\odot\,yr^{-1}\,Mpc^{-3}$ (by reading their Fig. 15), and one-third are contributed by their FIR-luminous galaxies which are detected in 450 μm (i.e. 4 sources, by reading their Fig. 5). In comparison, our FIR+mm sample has direct SFR densities of $10^{-1.628\pm0.092}$ and $10^{-2.198\pm0.050}\,M_\odot\,yr^{-1}\,Mpc^{-3}$ at $4 < z < 5$ and $5 < z < 6$ respectively (see Table 3). We have about 13 sources in $4 < z < 6$, hence our SFR density is higher than that of their 450 μm detected subsample but more close to that of their mass complete sample.

8.6. *Incompleteness corrections for cosmic SFR densities*

Based on the analysis in Section 8.2 and Fig. 25, we estimate the incompleteness corrections for our measured SFR densities of the FIR+mm sample, and then estimate the total cosmic SFR densities. We fit the literature SMF-converted SFR histograms to the observed SFR histogram in Fig. 25 at each redshift bin. The fitting only adjusts the normalization, and only uses the high-mass end histogram where the sample reaches the 50%-complete stellar mass limit ($M_{*,50\%lim.}$, e.g. by examining Fig. 24, since which stellar mass the FIR+mm galaxy number $N \geq 0.5 \times N_{SMF}$, see Section 8.3). The fitted SFR histograms are shown in Appendix D (Fig. D51). Then we integrate the re-normalized SMF-inferred SFR histogram (down to $10^8\,M_\odot$, same as Ilbert et al. 2013 and Muzzin et al.

TABLE 3: GOODS-N FIR+mm Star Formation Rate Densities

z_{low}	z_{high}	$\Psi_{SFR,obs.}$	$\sigma_{\Psi_{SFR}}$	$\Psi_{SFR,corr.}$	$SMF_{corr.}$	$f_{comp.}$
0.0	0.2	-2.022	0.227	-2.022	Muzzin	100.0%
				-2.022	Ilbert	100.0%
				-2.022	Davidzon	100.0%
0.2	0.4	-1.909	0.105	-1.895	Muzzin	96.9%
				-1.920	Ilbert	102.5%
				-1.876	Davidzon	92.7%
0.4	0.6	-1.429	0.071	-1.381	Muzzin	89.5%
				-1.394	Ilbert	92.3%
				-1.365	Davidzon	86.4%
0.6	0.8	-1.553	0.109	-1.468	Muzzin	82.1%
				-1.468	Ilbert	82.1%
				-1.457	Davidzon	80.0%
0.8	1.0	-1.206	0.073	-1.094	Muzzin	77.3%
				-1.082	Ilbert	75.3%
				-1.074	Davidzon	73.8%
1.0	1.5	-1.300	0.087	-1.148	Muzzin	70.4%
				-1.115	Ilbert	65.3%
				-1.099	Davidzon	62.9%
1.5	2.0	-1.396	0.070	-1.175	Muzzin	60.0%
				-1.117	Ilbert	52.5%
				-1.054	Davidzon	45.4%
2.0	2.5	-1.173	0.072	-1.082	Muzzin	81.1%
				-0.800	Ilbert	42.4%
				-0.712	Davidzon	34.6%
2.5	3.0	-1.345	0.105	-1.295	Muzzin	89.2%
				-1.073	Ilbert	53.4%
				-0.827	Davidzon	30.4%
3.0	4.0	-1.433	0.070	-1.265	Muzzin	67.9%
				-1.103	Ilbert	46.8%
				-0.825	Davidzon	24.6%
4.0	5.0	-1.628	0.092	···	Davidzon	∼5.3%?
				···	Grazian	∼5.6%?
				···	Song	∼0.7%?
				-1.317	MD14	∼49%
5.0	6.0	-2.198	0.050	···	Davidzon	∼3.0%?
				···	Grazian	∼0.7%?
				···	Song	∼0.2%?
				-1.662	MD14	∼29%?

The measured SFR density ($\Psi_{SFR,obs.}$, in unit of $M_\odot\,yr^{-1}\,Mpc^{-3}$) and uncertainty ($\sigma_{\Psi_{SFR}}$) from this work as described in Section 8.5, as well as the incompleteness-corrected cosmic SFR density ($\Psi_{SFR,corr.}$) and the completeness percentage in SFR ($f_{comp.}$, i.e. $= 10^{(\Psi_{SFR,obs.}-\Psi_{SFR,corr.})} \times 100\%$) as described in Section 8.6. We use literature SMFs and the Sargent et al. (2014) MS correlation to estimate the completeness percentage, therefore each SMF leads to a corrected value of $\Psi_{SFR,corr.}$ at each redshift bin. The $SMF_{corr.}$ column indicates which SMF is used (Davidzon et al. 2017; Grazian et al. 2015; Ilbert et al. 2013; Muzzin et al. 2013; Song et al. 2016), except for the MD14 (Madau & Dickinson 2014) rows at $z > 4$, which are our FIR+mm cosmic SFR densities added by the (Madau & Dickinson 2014) UV-based attenuation corrected SFR densities, under the assumption that our FIR+mm sample does not overlap with the UV-based samples at $z > 4$ (see demonstration in Section 8.8). The values with "?" in the last column indicate that they are unreliable because our FIR+mm sample has too low completeness, or even not overlapping with the UV-based samples (based on which the literature SMFs are determined).

2013) as an estimation of the total cosmic SFR. And the ratio of the total observed SFR to the total cosmic SFR is just the completeness fraction ($f_{comp.}$).

In Fig. 27, we present the cosmic SFR completeness fractions estimated with each literature SMF at each redshift bin. And in Fig. 28, we present the incompleteness-corrected total SFR densities.

At $z < 2$, the completeness of our sample drops linearly with $\log(1+z)$, and the three SMF-based results are fully consistent. However, starting from redshift 2, the three SMF-based estimations show large discrepancies. Due to the fact that Muzzin et al. (2013) SMF has a shallower low-mass end and fits our observed histograms much better, the completeness based on it has a high percentage of about 80% at $z \sim 3$. While the SMFs from Ilbert et al. (2013) and Davidzon et al. (2017) have steeper low-mass end hence lead to more than a factor of 2 lower completeness (see values of the completeness fraction $f_{comp.}$ in Table 3).

At $z > 4$, the fitting of our observed SFR histograms lead to too high SMF normalizations (see Appendix Fig. D51), hence the completeness fractions are very low, ranging from $\sim 0.2\%$ to $\sim 5\%$. If we do not re-normalize the SMFs but just integrate the SMF-based SFR histogram (i.e. as shown in Fig. 25), we will get a total cosmic SFR density fully consistent with the Madau & Dickinson (2014) curve at $z \sim 5$, and the excess of the observed SFR histograms will not be counted. The main reason for this would be that our FIR+mm sample at $z > 4$ will be mostly not overlapping with the UV-based samples (which will be demonstrated in the next sections). Thus to estimate the total cosmic SFR density at this high redshift range, we need to add our FIR+mm SFR density to the UV-based SFR density. In Fig. 28, we show the added total cosmic SFR densities at $z > 4$ as the red open squares. Our directly observed FIR+mm SFR densities are also shown as the red arrows. We list all corrected cosmic SFR density values in Table 3.

Our corrected measurements seem to imply total SFR densities consistent with what are reported in Madau & Dickinson (2014) over $0.5 < z < 2$, but possibly up to 0.4 dex higher at $2 < z < 4$ where the results are less reliable and largely dependent on the assumed SMF. But we also note that several recent FIR, (sub)mm and radio studies also seem to find similar trends. In Fig. 28, we show the literature cosmic SFR density measurements in Rowan-Robinson et al. (2016) and Novak et al. (2017, in prep.) for comparisons. Based on much larger area ($20\,degree^2$) but shallower FIR surveys, Rowan-Robinson et al. (2016) studied the FIR luminosity function with 3035 SPIRE $500\,\mu m$ sources. Their cosmic SFR densities (the gray filled squares) are much higher than the UV estimates at $3.5 < z < 6$ (i.e. the Madau & Dickinson (2014) curve in the figure) by factors of $\sim 2-6\times$. They assumed a fixed $500\,\mu m$ luminosity function (fixed $\alpha = 1.2$ and $\sigma = 0.60$ parameters) at $z > 3.5$, but whether such fixed form of FIR luminosity function is applicable is still controversial. Based on deep VLA imaging data in the large area COSMOS field, Novak et al. (2017, in prep.) integrated the radio 3 GHz luminosity function (assuming pure luminosity evolution) up to redshift 5–6, and estimated cosmic SFR density assuming a redshift dependent FIR-radio correlation (represented by the gray triangles in Fig. 28), which are in good agreement with the Madau & Dickinson (2014) curve and the average of our incompleteness-corrected data points at $z < 4$. However, at $z \sim 5$, their cosmic SFR density is $\sim 3\times$ the Madau & Dickinson (2014) value. Meanwhile, several works using HST optical/near-IR (e.g. H_{F160W}) band catalog sources as priors and applying stacking techniques in (sub)mm image data (i.e. Bourne et al. 2017; Dunlop et al. 2017) found very consistent cosmic SFR densities to the Madau & Dickinson (2014) values at $z \sim 5$. Bourne et al. (2017) even found that at $z \sim 5$ the

UV-based attenuation-corrected SFR density is higher than the FIR SFR density for their sample. This could likely be the fact that their sample lacks very dusty galaxies as in this work (which is IRAC, MIPS plus radio prior based).

As a further step, we make a simple parameter fitting to our incompleteness-corrected data points (i.e. all colored data points in Fig. 28) using the Madau & Dickinson (2014) double power-law and Gladders et al. (2013) (Abramson et al. 2016) log-normal equations, and obtain the following newly fitted equations/parameters:

$$\Psi = \Psi_0 \frac{(1+z)^{3.45}}{1+[(1+z)/2.70]^{5.60}}\ \mathrm{M_\odot\,yr^{-1}\,Mpc^{-3}}$$
$$\Psi_0 = 0.0071 \text{ (Chabrier IMF), or}$$
$$\Psi_0 = 0.0117 \text{ (Salpeter IMF)} \quad (3)$$

(the red thick solid curve in Fig. 28), and

$$\Psi = \frac{A_0}{t\sqrt{2\pi\tau^2}} \exp\left[\frac{-(\ln(t)-T_0)^2}{2\tau^2}\right]\ \mathrm{M_\odot\,yr^{-1}\,Mpc^{-3}}$$
$$t \text{ is the cosmic age in Gyr, } T_0 = 1.60,\ \tau = 0.70 \quad (4)$$
$$A_0 = 0.624 \text{ (Chabrier IMF), or}$$
$$A_0 = 1.023 \text{ (Salpeter IMF)}$$

(the red thick dashed curve in Fig. 28).

The new curves do not have large offset at the $z < 1$ range. The double power-law (solid curve) is higher at $z \sim 2$ but the log-normal (dashed curve) keeps original values at $z \sim 2$ where SMF-inferred agreed. At $z > 3$, both two new curves can generally fit the new FIR/radio-based data points. However, they split up at the last redshift bin, where Rowan-Robinson et al. (2016) measured a very high value but this work recovers only moderate value of FIR SFR density. There might still be some less extremely dusty galaxies that are missed by both this FIR+mm sample and the UV-based sample, but it would be beyond the detection limits of current FIR+mm data sets in this work.

8.7. *V/Vmax distribution of FIR+mm galaxies at $z > 2.5$*

The V/V_{max} diagram offers a way of examining the spatial distribution of the sample along redshift axis (Schmidt 1968). V is the co-moving volume for each source, while V_{max} is the maximum observable co-moving volume for each source (same as what were used when computing SFR densities in previous section). If the sample distributes uniformly along distance/volume axis, then V/V_{max} has a uniform distribution and a mean value of 0.5 (Schmidt 1968).

Fig. 29 shows the histograms of V/V_{max} of our $z > 2.5$ sample (upper panel), and a sub-sample of massive ($M_* > 10^{11.5}\,\mathrm{M_\odot}$) dusty galaxies (lower panel). In the upper panel, the observed V/V_{max} histogram has a nearly uniform distribution from 0 to about 0.5 then decreases rapidly, indicating that the sample is homogeneous at $z \sim 2-3$ then becomes rarer and rarer toward $z \sim 6-7$. However, in the lower panel, although the number is quite small, the distributions of most massive galaxies are almost homogeneous across the redshift range from $\sim 2-3$ to $\sim 6-7$.

8.8. *Comparing with Lyman-break galaxies*

We have found a substantial population of IR detected galaxies all the way to $z = 3$–6, and estimated their contribution to the SFR densities of the Universe to be fairly relevant and comparable or larger than that derived from UV rest-frame dropout surveys. It is therefore interesting to discuss the possible overlap between our IR selection and dropout selection in the UV, to evaluate whether our measurement should be *added* to the cosmic SFR density at least in part, or if we are measuring the same population.

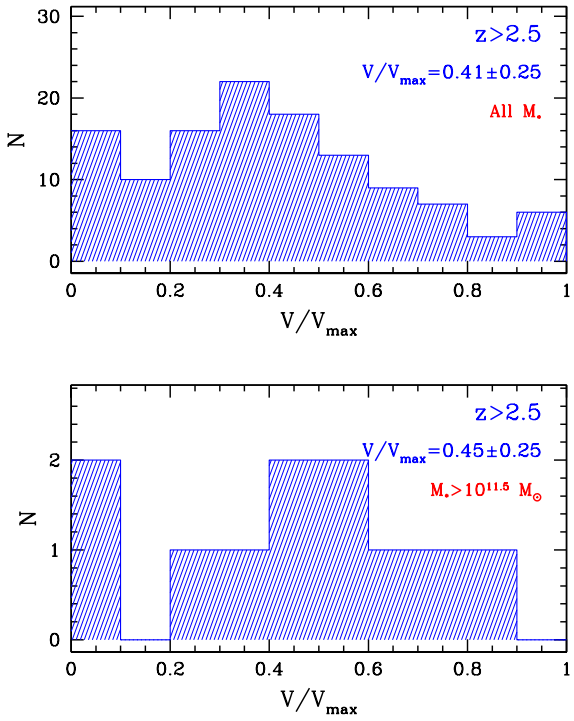

FIG. 29.—: The V/V_{max} histograms of all FIR+mm detected galaxies (upper panel) and $M_* > 10^{11.5}\,\mathrm{M_\odot}$ galaxies (lower panel) with $z > 2.5$. The V/V_{max} histogram reflects the spatial distribution of the sample along redshift axis (e.g. Schmidt 1968). See text in Section 8.3. The mean and scatter of V/V_{max} are shown in each panel. The mean value should equal 0.5 if the sample distributes homogeneously.

When a galaxy is at redshift $z \sim 3.1-4.4$ (Giavalisco et al. 2004; Vanzella et al. 2009), its Lyman break feature is shifted out of the B band, and its light suddenly becomes very faint from B band to all shorter wavelength bands, therefore it can be easily identified out as a B-dropout Lyman break galaxy (LBG). When the source is at a higher redshift, $z \sim 4.4-6.5$ (Giavalisco et al. 2004; Vanzella et al. 2009), similarly it can be identified out as a V-dropout LBG. However, such technique relies on measuring rest-frame UV light, and may therefore miss a fraction of dusty galaxies with large dust attenuation in the rest-frame UV bands. To investigate how dusty galaxies are missed in the dropout technique (i.e. LBG samples), we compare our GOODS-N FIR+mm detected sources at $z \sim 3.1-4.4$ and $z \sim 4.4-6.5$ with the B- and V-dropout criteria (e.g. Bouwens et al. 2012; Dickinson et al. 2004; Giavalisco et al. 2004; Stark et al. 2009; Vanzella et al. 2009).

We use the HST optical to near-infrared photometry in Skelton et al. (2014) (cross-matched in Section 2) and use the color-color criteria from Vanzella et al. (2009) for seleting the B- and V-dropout LBGs in GOODS-N for comparison:

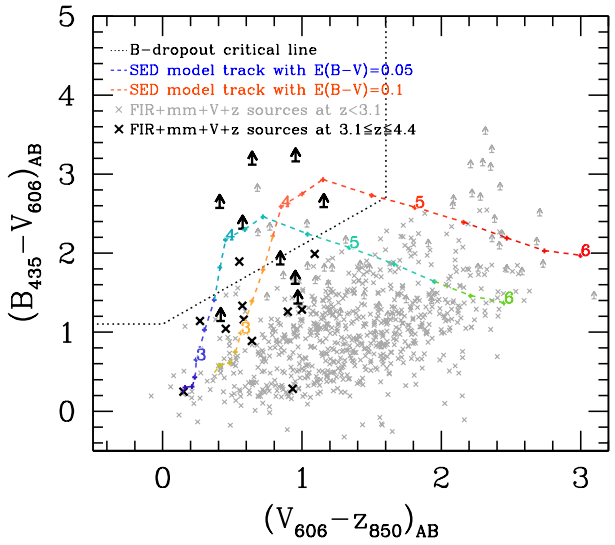

FIG. 30.—: Color-color diagram for identifying B-dropouts at $3.1 \leq z \leq 4.4$ (Vanzella et al. 2009). Data points are FIR+mm detected galaxies which are also detected at V_{606} and z_{850} bands. Gray ones are at $z < 3.1$, and black ones are at $3.1 \leq z \leq 4.4$ (e.g. Fig. 1 of Vanzella et al. 2009). Galaxies not detected in B_{435} are shown as upward arrows ($1\,\sigma$ lower limits). The dotted line indicates the B-dropout criteria (Eq. 5). Two colored curves indicate two model tracks calculated from our SED templates (Fig. 2), with E(B-V) = 0.05 and 0.1 as two examples. The small colored number at each node of the track indicates the redshift.

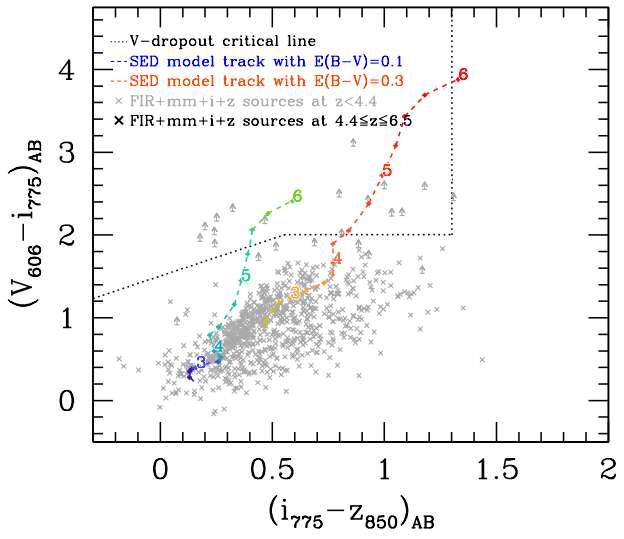

FIG. 31.—: Color-color diagram for identifying V-dropouts at $4.4 \leq z \leq 6.5$ (Vanzella et al. 2009). Data points are FIR+mm detected galaxies which are also detected at i_{775} and z_{850} bands. All data points are in gray color, which represents they are at $z < 4.4$. No black data point in this figure which represents $4.4 \leq z \leq 6.5$ (e.g. Fig. 2 of Vanzella et al. 2009). Galaxies not detected in V_{606} are shown as upward arrows ($1\,\sigma$ lower limits). The dotted line indicates the V-dropout criteria (Eq. 6). The colored curves indicate the model tracks (similar to the previous figure but with E(B-V) = 0.1 and = 0.3 as two examples).

- B-dropout

$$\begin{cases} (B_{435}-V_{606}) > (V_{606}-z_{850})+1.1 \\ \text{and } (B_{435}-V_{606}) \geq 1.1 \\ \text{and } (V_{606}-z_{850}) \leq 1.6 \end{cases} \quad (5)$$

- V-dropout

$$\begin{cases} \begin{cases} (V_{606}-i_{775}) > 0.9 \times (i_{775}-z_{850})+1.5 \\ \text{or } (V_{606}-i_{775}) > 2.0 \end{cases} \\ \text{and } (V_{606}-i_{775}) > 1.2 \\ \text{and } (i_{775}-z_{850}) < 1.3 \\ \text{and S/N}\,(B_{435}) < 2 \end{cases} \quad (6)$$

In Fig. 30, the FIR+mm detected sources that also have V_{606} and z_{850} detections are plotted in the $B_{435}-V_{606}$ versus $V_{606}-z_{850}$ diagram. The subscripts indicate the HST observing bands, i.e. F435W for B band, F606W for V band and F850LP for z band. The central wavelengths of these bands may slightly differ from literature B-dropout technique, for example F435W central wavelength is bluer than 0.435 μm (see Table 6 of Skelton et al. 2014), so B_{435} dropout LBGs actually corresponds to $z \sim 3-4.5$. In the figure, we also show two modeled tracks as the colored curves, which are calculated by redshifting the SED templates (BC03+DL07, e.g. Fig. 2). Here we show two example model tracks with $E(B-V) = 0.05$ and 0.1. Heavier dust attenuation will make the model track shift toward upper right. Data points within the upper left region identified by the dotted lines are the B_{435}-dropouts.

Among all the FIR+mm and V_{606} and z_{850} detected galaxies (i.e. data points shown in Fig. 30), we highlight in Fig. 30 the 37 ones having $3.1 \leq z \leq 4.4$. Only 6 of them can be identified as B-dropout (we use 1 σ limits same as Vanzella et al. 2009, but note that plotting with 2 σ limits will lead to half of them no longer being B-dropouts). In comparison, we have 51 FIR+mm galaxies in total with photometric redshift within $3.1 \leq z \leq 4.4$ (either with 3D-HST counterpart or not), thus most of them could not be identified as B-dropout. In addition, even for this very small number of galaxies that satisfy as dropouts, the rest-frame UV based SFR still significantly underestimates the dust-obscured SFR. For example for ID 3276, the source that is detected in B band and is within the B-dropout region in Fig. 30, the optical/near-IR (rest-frame UV) based SFR accounted for dust attenuation is $\sim 32\,M_\odot\,yr^{-1}$ (stellar mass $10^{11.06}\,M_\odot$) in the 3D-HST catalog. Meanwhile, its FIR+mm based SFR is as high as $256 \pm 37\,M_\odot\,yr^{-1}$ in our FIR+mm SED fitting.

In Fig. 31, we show the distribution of FIR+mm galaxies with i_{775} and z_{850} detections in the $V_{606}-i_{775}$ versus $i_{775}-z_{850}$ diagram. None of the 7 galaxies in our sample with a photometric redshift within the V-dropout range of $4.4 \leq z \leq 6.5$ is detected in i_{775} and z_{850}. There are some galaxies within the V-dropout region (the left-top region), for which we have a lower redshift estimate.

We conclude that there is very little overlap between our IR-selected high redshift galaxies and dropout samples. And even in that case the UV properties do not allow to recover the large SFRs in these sources. We thus conclude that the SFR density contributions we have estimated are largely independent from the UV ones, at least at $z \gtrsim 3$.

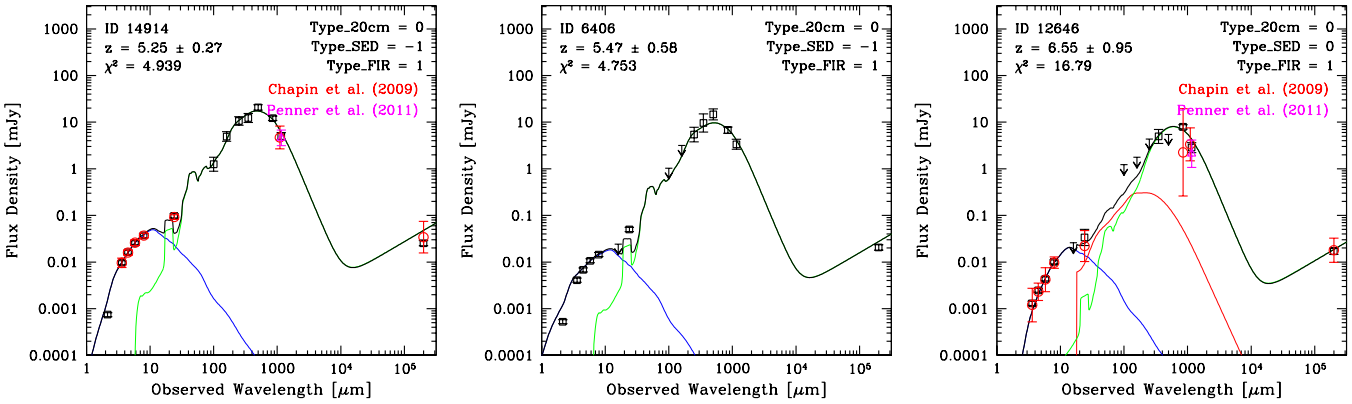

FIG. 32.—: The best-fit SEDs from the $\langle U \rangle$-dependent SED fitting for the three $z \geq 5$ MS type FIR+mm galaxies: ID 14914, ID 6406 and ID 12646. The blue (near-IR wavelengths), red (if present at mid-IR wavelengths) and green (FIR wavelengths) curves represent the stellar, mid-infrared AGN (if present) and dust components. Parameters in the upper right corner are described in Section 3.1.

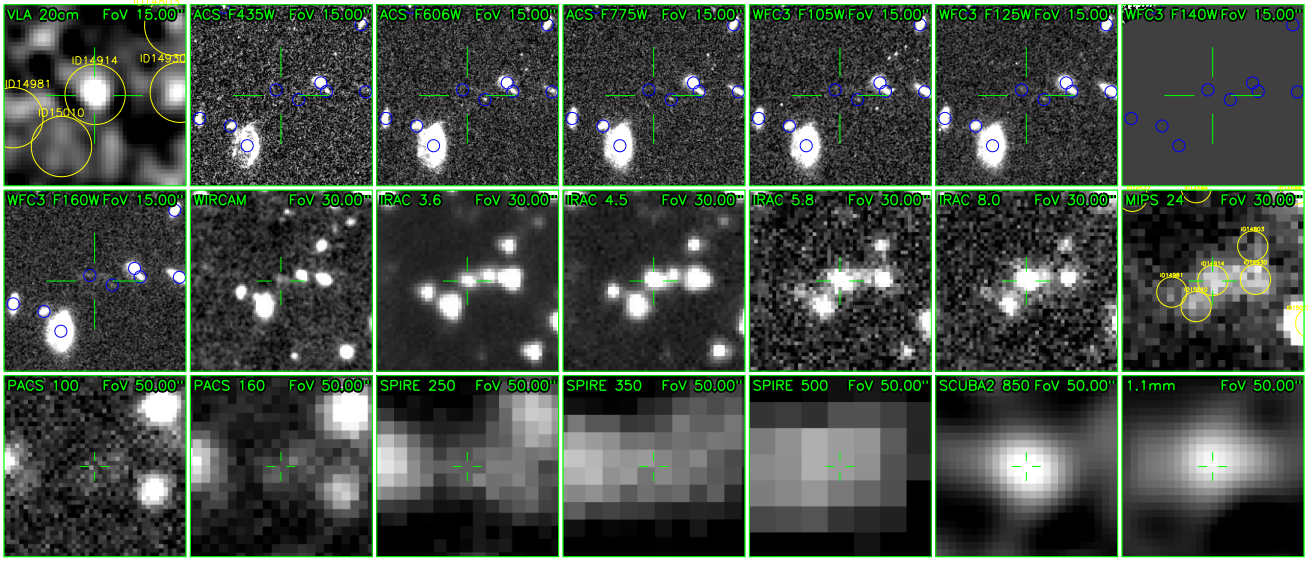

FIG. 33.—: The multi-wavelength cutouts of ID 14914. The instrument and bandpass of each cutout image is labelled in each panel. Yellow circles in the first panel and the MIPS 24 panel are our 24+radio sources and have a diameter of 5″. Blue circles in the HST panels are the 3D-HST sources and have a diameter of 0.5″. All panels are centered on the IRAC position (as indicated by the green cross) of the source under examination (ID 14914). The field of view is also indicated in each panel.

8.9. *A sample of candidate $z \geq 5$ MS galaxies*

From our FIR+mm catalog we find three sources that have FIR+mm SED photometric redshift ≥ 5 and appear to be consistent with the MS at these redshifts. These are ID 14914 (which is not in *goodArea*), ID 6406 and ID 12646 (the rightmost blue data point in Fig. 22, our highest redshift candidate, with $z \sim 6.5$). We discuss the properties of these three particularly interesting sources in some details below.

ID 14914 is detected in all FIR+mm bands. Its multi-wavelength cutouts are presented in Fig. 33. Weak extended emission in ACS and WFC3 images can be found. Two 3D-HST sources are very close to ID 14914. We cross-matched the closer (0.585″) 3D-HST source at North-East as the counterpart. Its IRAC emission is clearly detected as well as the (sub)mm and VLA 20 cm. The blending is not significant. The 3D-HST ID and other properties are listed below:

$$
\begin{aligned}
\mathrm{ID}_{\mathrm{IRAC}} &= 14914 \\
\mathrm{ID}_{\mathrm{3D\text{-}HST}} &= 7338 \\
z_{\mathrm{FIR+mm}} &= 5.21 \pm 0.24 \\
z_{\mathrm{3D\text{-}HST}} &= 5.57\ (5.335 - 5.90)\ ^{30} \\
M_* &\approx 10^{11.68}\ \mathrm{M}_\odot\ ^{31} \\
\mathrm{SFR}_{\mathrm{3D\text{-}HST}} &= 436.5\ \mathrm{M}_\odot\,\mathrm{yr}^{-1} \\
\mathrm{SFR}_{\mathrm{FIR+mm}} &= 1750 \pm 133.5\ \mathrm{M}_\odot\,\mathrm{yr}^{-1} \\
\langle U \rangle &\approx 45
\end{aligned}
\tag{7}
$$

[30] The photometric redshift range in brackets indicate the 1 σ (68%) lower and upper confidence limits.

[31] Note that 3D-HST has a stellar mass of $M_{*,\mathrm{3D\text{-}HST}} = 10^{12.55}\,\mathrm{M}_\odot$ for

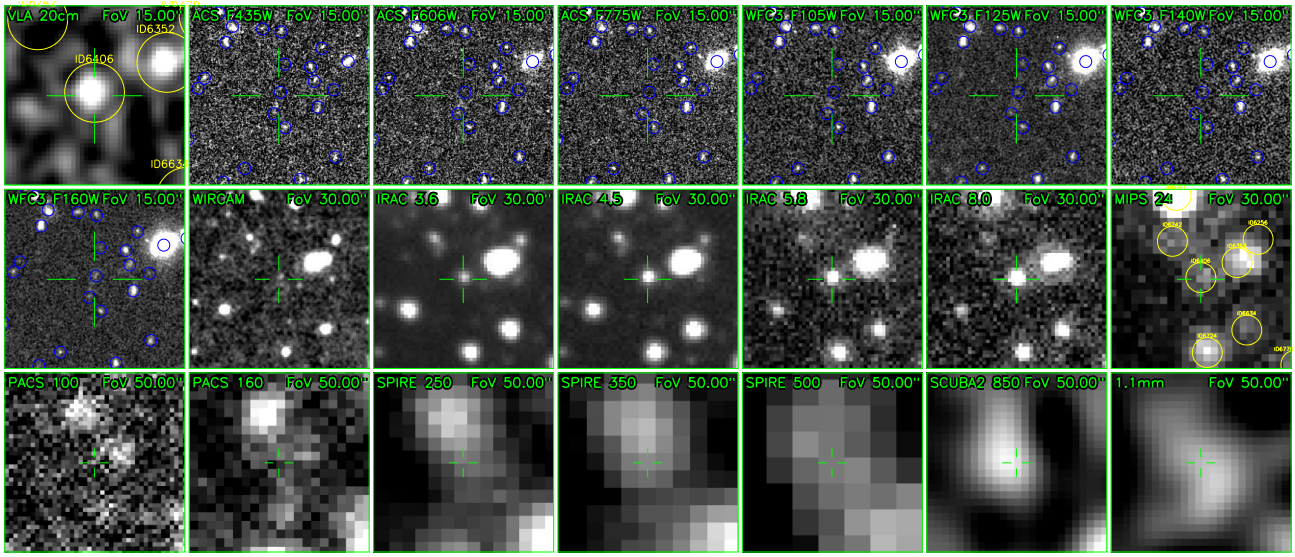

FIG. 34.—: The multi-wavelength cutouts of ID 6406. See the caption in Fig. 33.

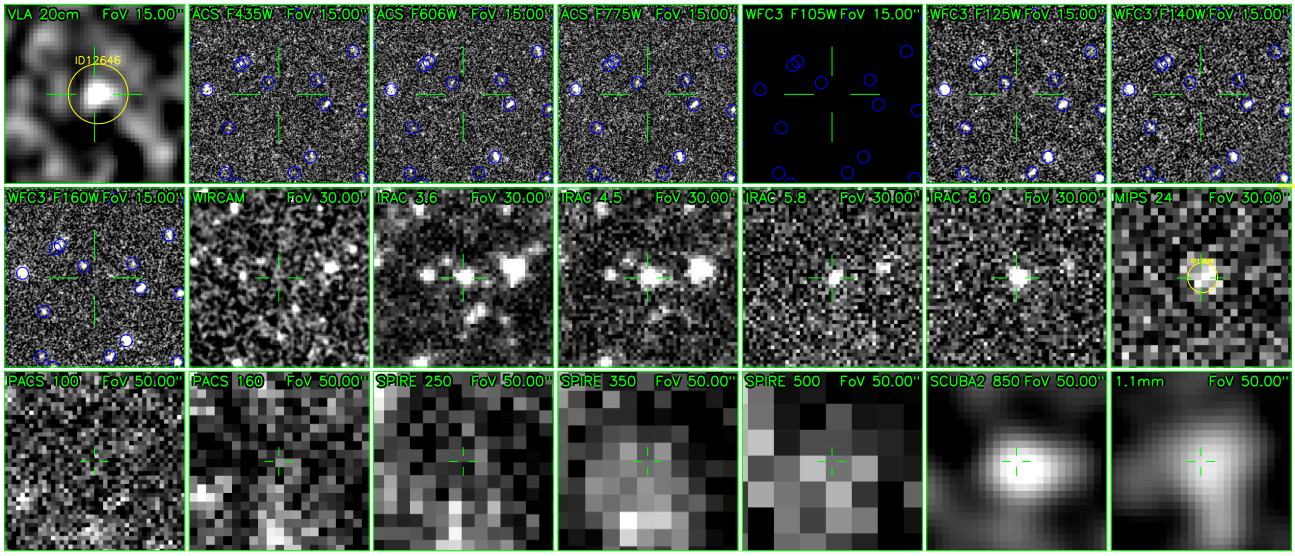

FIG. 35.—: The multi-wavelength cutouts of ID 12646. See the caption in Fig. 33.

It is also identified as AzGN04 and GN1200.12 in Perera et al. (2008), Greve et al. (2008) and Penner et al. (2011). We show the photometry of Chapin et al. (2009) and Penner et al. (2011) in Fig. 32 for comparisons (as red circles and magenta triangle respectively), which show good agreement.

ID 6406 is detected in the long-wavelength FIR and (sub)mm bands. Its cutouts are presented in Fig. 34. It is almost invisible in ACS images but but is detected in the near-IR by WFC3 images and becomes clear in IRAC images, as well as the (sub)mm and radio images. Its 3D-HST and FIR+mm properties are listed below:

$$\begin{aligned} \mathrm{ID}_{\mathrm{IRAC}} &= 6406 \\ \mathrm{ID}_{\text{3D-HST}} &= 26337 \\ z_{\mathrm{FIR+mm}} &= 5.47 \pm 0.58 \\ z_{\text{3D-HST}} &= 5.47\ (3.725 - 5.82) \\ M_{*,\text{3D-HST}} &= 10^{11.44}\ \mathrm{M}_{\odot} \\ \mathrm{SFR}_{\text{3D-HST}} &= 0.1\ \mathrm{M}_{\odot}\,\mathrm{yr}^{-1} \\ \mathrm{SFR}_{\mathrm{FIR+mm}} &= 1109 \pm 119.6\ \mathrm{M}_{\odot}\,\mathrm{yr}^{-1} \\ \langle U \rangle &\approx 50 \end{aligned} \tag{8}$$

This source has no counterpart in Perera et al. (2008), Greve et al. (2008) and Penner et al. (2011). The closest sub-mm source is AzGN31 in Perera et al. (2008) catalog (at a distance of 4.9″) and ID 33 in Penner et al. (2011) catalog (at a distance of 8.8″). But further NOEMA mm follow-up observation shows that its accurate position is consistent with the

this source (see the catalog of Skelton et al. 2014), fitted at redshift 5.57. However, from our SED fitting or simply by comparing IRAC fluxes with other sources e.g. GN20, we find much lower stellar mass at a similar redshift of 5.21. GN20 has a peak stellar (over IRAC wavelengths) flux of ∼35 μJy, $z = 4.055$ and $M_* = 10^{11.28}\,\mathrm{M}_{\odot}$ (see Fig. 9), then by scaling to $z = 5.21$ with $d_L^2\,(1+z)^{-1}$ and to an IRAC peak flux of ∼60 μJy (see Fig. 32), we get $M_* \approx 10^{11.68}\,\mathrm{M}_{\odot}$. This value is not far from our next SED fitting results, but much more reasonable than the 3D-HST value. Therefore here we quote our own stellar mass value.

IRAC and VLA 20 cm position (Liu, Daddi et al. in prep.).

The multi-wavelength cutouts of ID 12646 are presented in Fig. 35. There is no obvious detection in ACS or WFC3 images at the exact IRAC position. The closest 3D-HST source is 3D-HST ID 12669 at a photometric redshift of 4.65 (4.248 – 5.06), however at a distance of 1.52″. It is unlikely to be the counterpart of ID 12646 given the radio localization. ID 12646 is also not matched to any source in the catalog of Pannella et al. (2015), hence we do not have a stellar mass for it. The emission starts to be seen in the WIRCAM K_s image but has an irregular morphology and low S/N. It is fairly bright in IRAC images and bright in (sub)mm but with some offset from the emission peak. It matches AzGN10 in Perera et al. (2008), Chapin et al. (2009) and Penner et al. (2011). Its physical properties are listed below:

$$\begin{aligned} \mathrm{ID}_{\mathrm{IRAC}} &= 12646 \\ z_{\mathrm{FIR+mm}} &= 6.55 \pm 0.95 \\ M_* &\approx 10^{11.41}\ \mathrm{M}_\odot \ ^{32} \\ \mathrm{SFR}_{\mathrm{FIR+mm}} &= 728 \pm 58.6\ \mathrm{M}_\odot\ \mathrm{yr}^{-1} \\ \langle U \rangle &\approx 31 \end{aligned} \tag{9}$$

The photometry of Chapin et al. (2009) and Penner et al. (2011) is also shown in the ID 12646 panel of Fig. 32. The measurements generally agree with each other. To estimate the photometric redshift, Chapin et al. (2009) adopted a simple method which infers redshift as a function of IRAC and 24 μm flux according to Pope et al. (2006), and got a photometric redshift ~ 3. Note that using their equation, GN20 (ID 564 in this work) with a spectroscopic redshift of 4.055 would have a photometric redshift ~ 2.6.

While these sources are interesting and candidates for the most distant IR-detected sources in GOODS-N, we emphasize how we still only have photometric redshift estimates. In particular, the optical/near-IR SEDs are very red, faint in the optical and rising at wavelengths > 3 μm. It is hard to obtain precise redshifts in these cases. Note, however, that the redshifts estimated from the IR SED agree well in all cases, while using templates with $\langle U \rangle \sim 30$–$40$, lower than what is expected for MS galaxies at $z > 4$ (Béthermin et al. 2015) Because of the dust temperature/redshift degeneracies, using warmer templates would further increase their redshifts. We cannot exclude that these sources are actually SB galaxies, and their $\langle U \rangle$ values would be appropriate in that case. However, even in that case, substantially lower redshifts would require very cold dust SEDs, which seems unlikely.

Spectroscopic observations will be the key to break these limitations and help understand the reasons that cause different SED fitting results. Due to the dusty nature of these FIR+mm galaxies, optical/near-IR spectroscopic observations will likely not be as efficient as for LBGs. Mid-IR spectroscopic surveys with JWST and (sub)mm spectral line scan with ground-based interferometry arrays will be the most efficient ways to measure redshifts.

9. SUMMARY

In this work we present detailed *"super-deblended"* photometry for the far-infrared to (sub-)millimeter image data in GOODS-N. To overcome the heavy blending problems introduced by the large PSFs, especially at Herschel SPIRE and (sub)mm bands, we developed a new method in which we choose the prior sources to use in the fit for the photometric measurements and the ones to be frozen and subtracted at each FIR/mm band. We run SED fitting to predict the flux of each source at each band, then determine the critical flux value for choosing an actual prior source list at each band by considering both the number density and the priori detection limit. The number of fitted sources at each band can therefore be kept to reasonable values of less than or about 1 per PSF beam area. For the non-fitted sources, which are hopelessly faint at that band, we eliminate their flux by modeling their image and subtracting it from the observed data. In this way the problem of flux boosting of fitted sources can also be largely reduced.

We generated Monte-Carlo simulations to verify the photometry measurements, and generate statistical correction recipes to obtain reasonable uncertainties of measurements with a nearly Gaussian behavior. The corrections are linked to three measurable parameters in the three-step recipes. Thus for real sources, we can correct flux bias and uncertainties for each source according to their measured parameters. The final uncertainties follow well-behaved statistics, which are important to obtaining more reasonable physical properties from SED fitting.

Finally a list of 1185 IRAC catalog sources are selected with the combined $\mathrm{S/N} \geq 5$ over the FIR and (sub)mm bands, including 71 detections at $z \geq 3$. Comparing with the empirical SFR–M_* main-sequence at these redshifts, the majority of these dusty galaxies appear to be classified as "normal" type MS galaxies at such high redshift, although we caution that the MS level is not very well known yet at these highest redshifts.

We compute the directly observed SFR densities of our FIR+mm sample with the $1/V_{max}$ method plus a bootstrapping method. We estimate the completeness in SFR for our FIR+mm sample with the SMF-converted SFR histograms. At $z \leq 2$, values estimated using different stellar mass functions from the literature are similar and consistent, but they vary considerably at $z \sim 2-4$ due to the disagreements between faint-end SMF slopes in the literature, and are even worse at $z \sim 4-6$ where we effectively detect only the few most massive galaxies (including, notably, the GN20 protocluster galaxies).

We find that the completeness corrected cosmic SFR densities agree well with the standard literature results from Madau & Dickinson (2014) and Gladders et al. (2013) at $z \leq 2$. At $z \sim 2-4$, the corrections vary strongly with the adopted SMFs, but we suggest that the total SFR density could be higher than the literature SFR densities by as much as a factor of 3. At $z > 4$, we only provide the directly observed SFR densities in Fig. 26, and the value minus $1\,\sigma$ uncertainty as the very conservative lower limits in Fig. 28.

We find that our estimation for SFR densities are largely independent from those derived from the UV-selected galaxies, and thus should be in principle added to the UV ones, at least for $z \gtrsim 3$ and only for the directly measured quantities at the bright end, as our sample does not obviously overlap with *B*- and *V*-dropout LBGs.

DL and ED would like to thank the Chinese Academy of Sciences (ACS) – Le Centre national de la recherche scientifique (CNRS) Joint PhD Program. Y.G. acknowledges support from the National Natural Science Foundation of

[32] Similarly, by scaling GN20 to a peak stellar flux of ~ 23 μJy beyond IRAC wavelengths and a photometric redshift of 6.55, we get $M_* \approx 10^{11.41}\,\mathrm{M}_\odot$.

China (grants 11390373 and 11420101002) and the Chinese Academy of Sciences' Key Research Program of Frontier Sciences. MTS acknowledges support from a Royal Society Leverhulme Trust Senior Research Fellowship (LT150041).

APPENDIX

DATA SETS

GOODS-North (hereafter GOODS-N) is one of the most extensively observed blank deep fields with deepest data existing across all wavebands. Therefore it is the best field for testing and verifying the source deblending tools for FIR/mm images. In this work, we make use of deep NIR catalog as an initial step to determine the prior source position list for the prior source fitting photometry at each FIR/mm band. And the photometry at these bands are not independent, because at each band we have used all the measurements at shorter wavelengths/higher resolution bands, based on which we have constructed the NIR-to-radio SED for each prior source, and used SEDs to help reducing the prior list before actual prior fitting at this band. The used NIR catalog and NIR-to-radio data sets are listed as follows:

Initial catalogs and spectroscopic redshifts

In this work, we use the IRAC catalog from the GOODS-*Spitzer* Legacy Program (PI: M. Dickinson) as an initial step. We also use the *K* band photometry measurements and stellar mass properties from Pannella et al. (2015), as well as spectroscopic redshifts from various literature (Barger et al. 2008; Casey et al. 2012b; Cohen et al. 2000; Wirth et al. 2004, Stern et al. in prep; Inami et al. in prep;).

This IRAC catalog contains 19437 galaxies that are detected using SExtractor (Bertin & Arnouts 1996) in the weighted average image of the 3.6 μm and 4.5 μm images. This catalog is also adopted as the prior catalog in Elbaz et al. (2011); Magnelli et al. (2009, 2011, 2013).

There are also other deep catalogs at shorter wavelength bands, but their depths are not deeper than the IRAC catalog. For example, the Subaru/MOIRCS Ks-selected catalog (Kajisawa et al. 2011) contains 9873 sources in a smaller area (103.3 arcmin^2) than the area of IRAC catalog. Simply scaling to the same area, the source number is around 18000, so the number of sources in two catalogs are comparable within 8%. And the HST/WFC3-selected catalog (Skelton et al. 2014) also has comparable depth. It covers an area of 164 arcmin^2 in GOODS-N, and 15892 out of 38279 sources have S/N ≥ 3 at IRAC 3.6 μm band. When scaled to the same area as the IRAC catalog, the source number is around 18100, also within a percentage of 8%.

Mid-infrared and radio images

The GOODS-N MIPS 24 μm image data are from GOODS-*Spitzer* Legacy Program. The observations were done in August 2004 (PI: Dickinson) and approximately cover $10' \times 16.5'$ on the sky. The 1 σ noise is listed in Table 1 as well. More details can be found in GOODS-*Spitzer* document: http://irsa.ipac.caltech.edu/data/SPITZER/GOODS/docs/goods_dr3.html.

The GOODS-N VLA 1.4 GHz (radio) image data are from two data sets: Owen (2017) and Morrison et al. (2010). Both observations cover a similar area of $40' \times 40'$, which is much larger than that of 24 μm, but the former data are observed later and are deeper than the latter one. For reference, Morrison et al. (2010) detected 1230 sources with S/N $> 5\sigma$ (i.e. $\sim$20 μJy at center, and higher toward outer region) in their full image. A full radio catalog produced with the new data will be presented in Owen (2017). Here we have made preliminary radio photometry measurements, although this is not be the best way to measure flux for sources in interferometry data. In this work, the preliminary radio photometry measurements are only used in SED fitting to predict FIR/mm flux of each prior source, hence are still acceptable. We will compare with the more reliable radio catalog in Owen (2017) when it's available.

The GOODS-N *Spitzer* IRS Peak-Up Imaging (PUI) 16 μm image data (Teplitz et al. 2011) are also used in this work. Although the 16 μm image is much shallower than the 24 μm image data, they can still improve the accuracy of the SED fittings for brighter sources.

Far-infrared and (sub-)millimeter images

The PACS 100 and 160 μm image data are from the *PACS Evolutionary Probe* program (PEP; PI: D. Lutz). The image data are combined with the observations of PEP and the GOODS-*Herschel* key program (PI: D. Elbaz) by Magnelli et al. (2013). We adopt the photometry parameters suggested in the PEP data release v1 document of http://www.mpe.mpg.de/resources/PEP/DR1_tarballs/readme_PEP_global.pdf. Following which, we have also applied the high-pass filtering correction for the PACS photometry.

The SPIRE 250, 350 and 500 μm image data are from GOODS-*Herschel*. *The Herschel Multi-tiered Extragalactic Survey* (HerMES, PI: Oliver) also have the SPIRE observations, but the data from GOODS-*Herschel* are deeper. GOODS-*Herschel* data have a total observing time of 31.1 hours. See the document of http://hedam.lam.fr/GOODS-Herschel/data/files/documentation/GOODS-Herschel_release.pdf. In comparison, the HerMES data have a total observing time of 13.51 hours (Oliver et al. 2012). See their document of http://hedam.lam.fr/HerMES/index/download.

The sub-mm image data are from the ground-based *James Clerk Maxwell Telescope* (JCMT) 850 μm *SCUBA-2 Cosmology Legacy Survey* (S2CLS; Geach et al. 2017). The image data are recently publicly available on http://dx.doi.org/10.5281/zenodo.57792. We use their "S2CLS_GOODS-N_MF_FLUX_DR1.FITS" image data which are processed with matched-filtering recipe so that point source sensitivity can be best optimized. The median depth per field is approximately 1.2 mJy beam^{-1}, comparing that the confusion limit at this wavelength is approximately $\sigma_c \approx 0.8$ mJy beam^{-1}. For PSF fitting we constructed an PSF image with double-Gaussian function according to the Equation (1) of Geach et al. (2017) and the text therein.

The mm image data are a combination of two data sets from Penner et al. (2011): JCMT AzTEC 1.1 mm image and IRAM MAMBO 1.2 mm image. The image data can be found in http://www.astro.umass.edu/%7epope/goodsn_mm/.

The combined data have a central wavelength of 1.16mm, with an overall 1σ noise of $\sim 0.5 mJy$ (Penner et al. 2011). The PSF is relatively large ($19.5''$). Penner et al. (2011) identified 41 secure sources with $S/N \geq 3.8$ from blind source extraction. A comparison between our flux measurements and uncertainties and theirs are in Fig. 16 and Fig. 17.

In Table 1 we summarize the PSF FWHM of each image, and the mean $1\,\sigma$ rms noise ($\bar{\sigma}$) measured from our final catalog, and the number of sources with S/N > 3 at each band.

PHOTOMETRY IMAGE PRODUCTS

We present the photometry image products at each band here. In Fig. B36, the three images in the first row show the subtraction of *hopelessly faint* sources (see description in Section 3.3). From left to right, they are the original image at this band, the faint-source-model image made from their SED predicted flux, and the faint-source-subtracted image which is made by subtracting the middle panel from the left panel. The three images in the second row show the prior-extraction photometry at this band. From left to right, they are the faint-source-subtracted image (identical to the right panel of first row but marked sources with yellow circles), the best-fit-model image, and the residual image which is left panel subtracting middle panel. We run SExtractor in the residual image to detect additional sources at each band. But at this band we detect no obvious additional source. At other FIR/mm bands, for example Fig. B37, we show the detection of additional sources (green circles) and the fitting including them in the third row images. In Fig. B37 to Fig. B41, from left to right, the three images in the third row are the faint-source-subtracted image, the best-fit-model image including prior sources and additional sources, and the final residual image.

All images have the same scaling. At this band the images are shown in logarithm scaling. The circles in the bottom-left panel indicates all fitted sources. Circle radii are proportional to the power 0.5 of their measured flux, but with a maximum value when S/N reaches 10. Sources with S/N below 3 are shown as dashed circles.

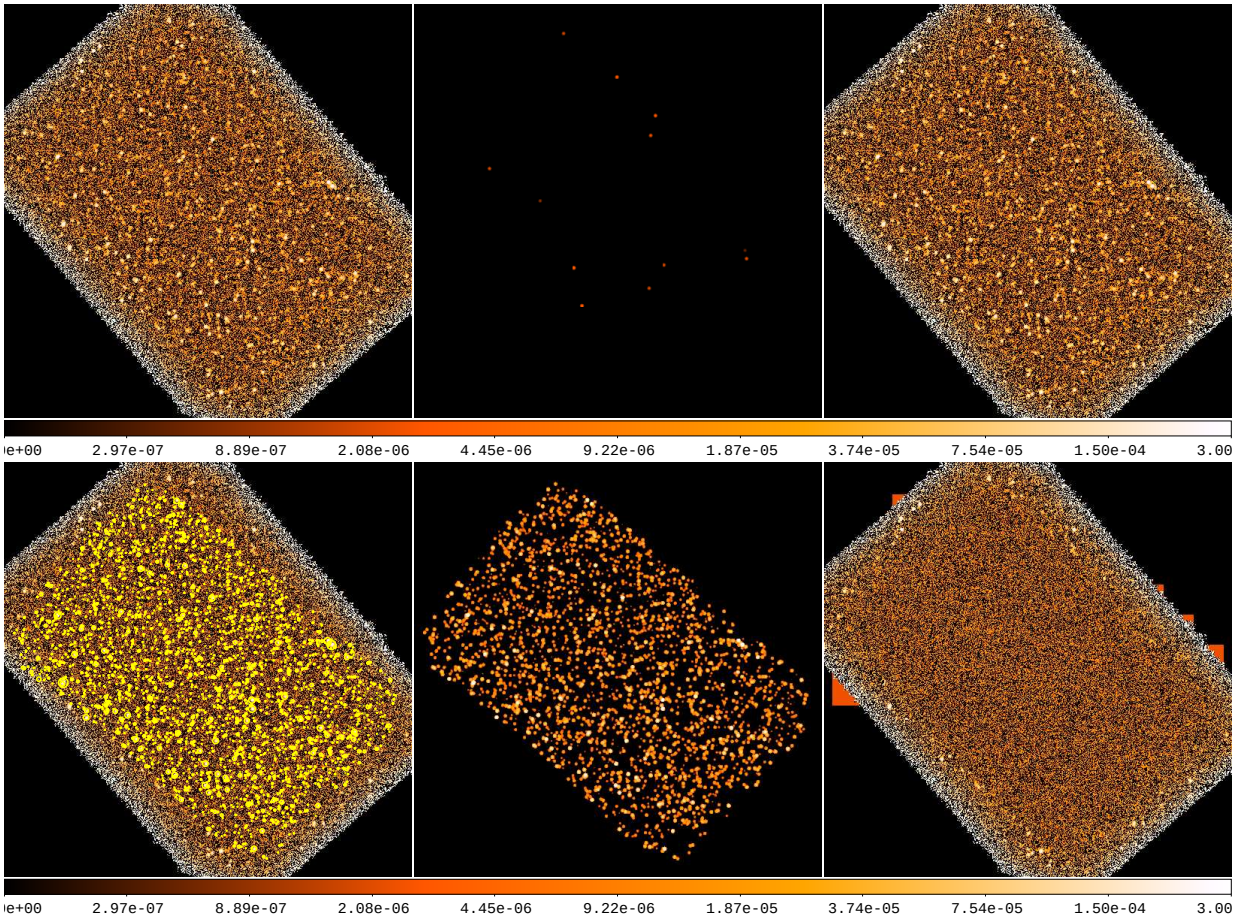

FIG. B36.—: Photometry image products at 100 μm. See descriptions in text.

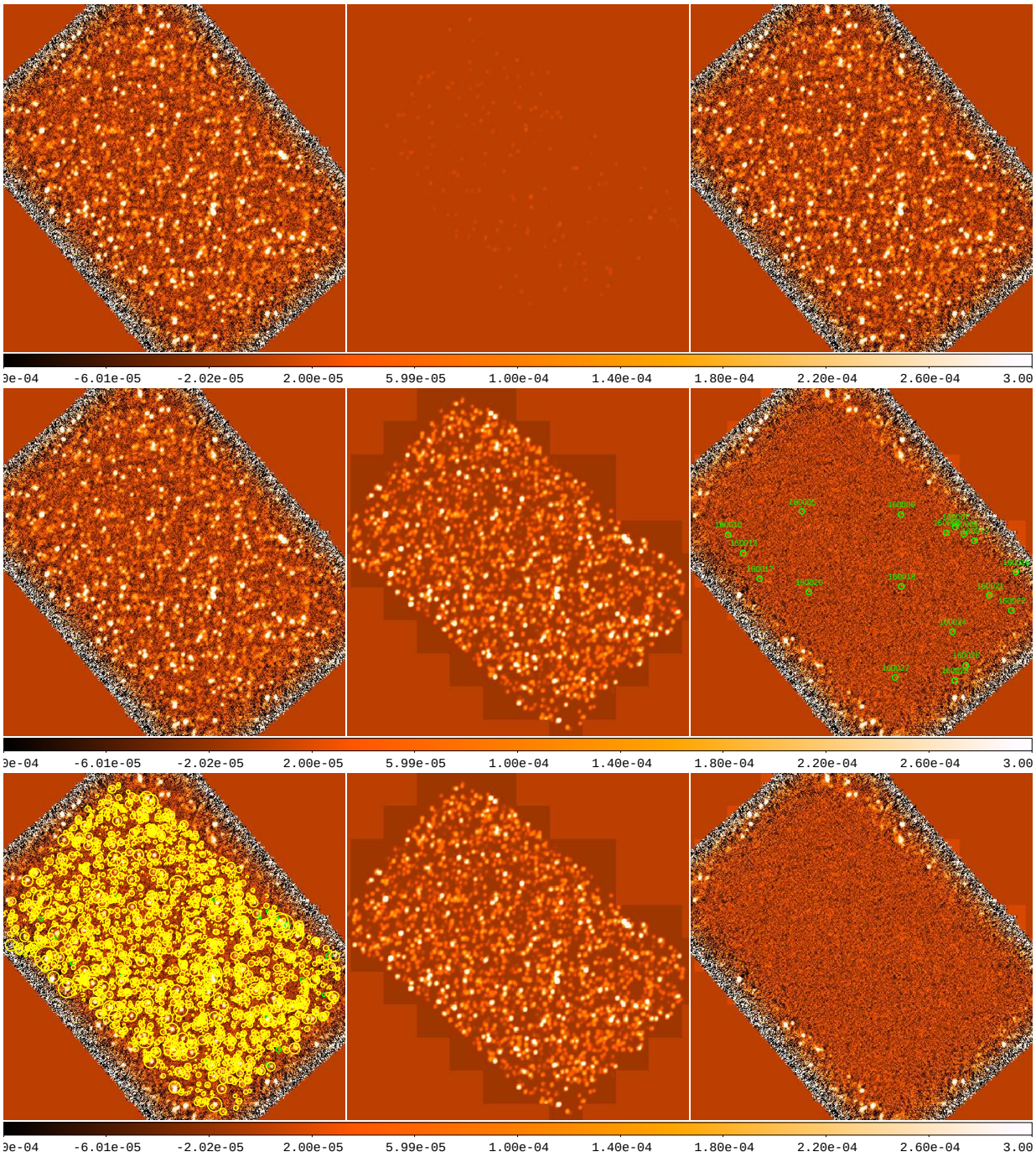

FIG. B37.—: Photometry image products at 160 μm. See descriptions in text.

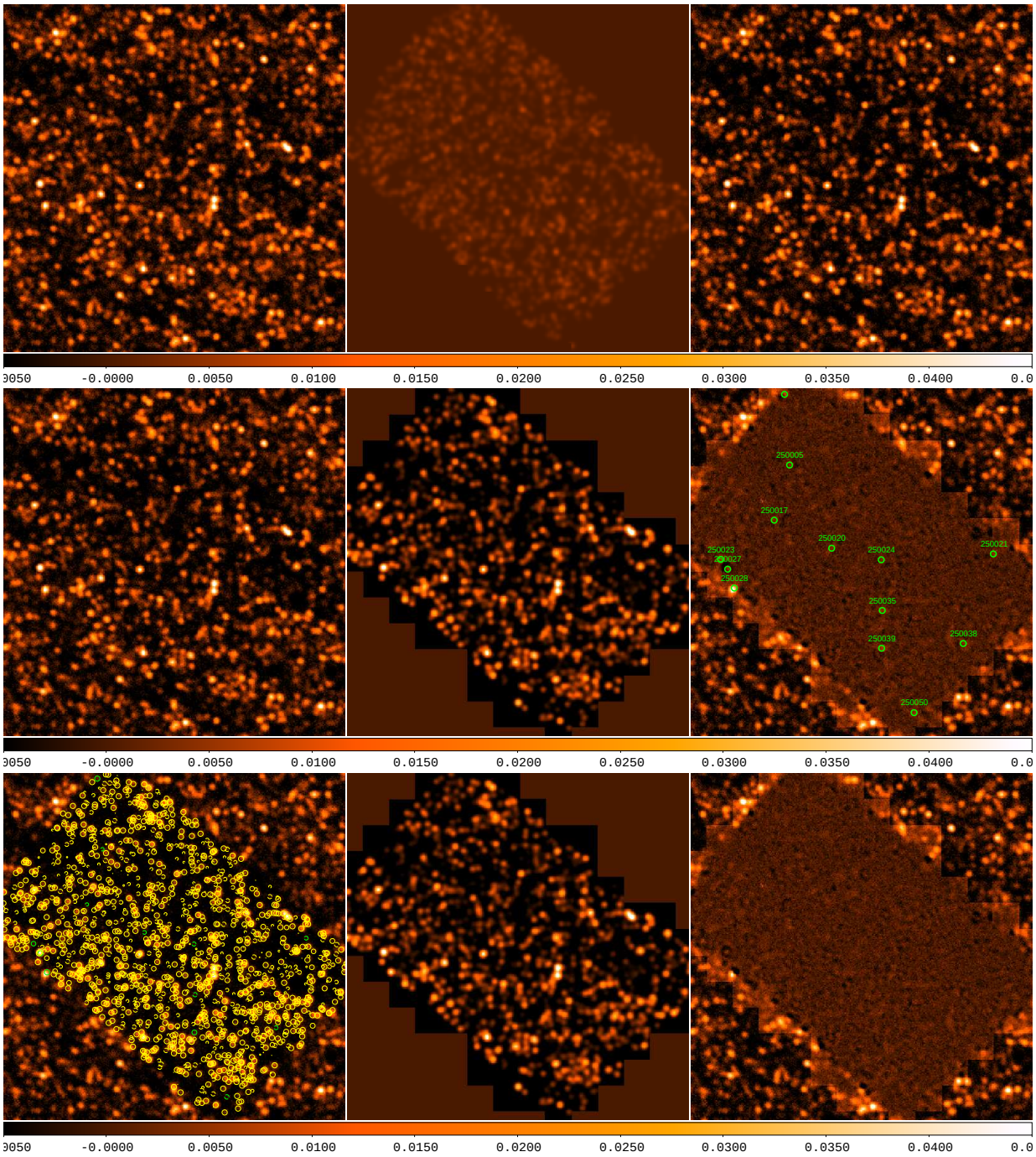

FIG. B38.—: Photometry image products at 250 μm. See descriptions in text.

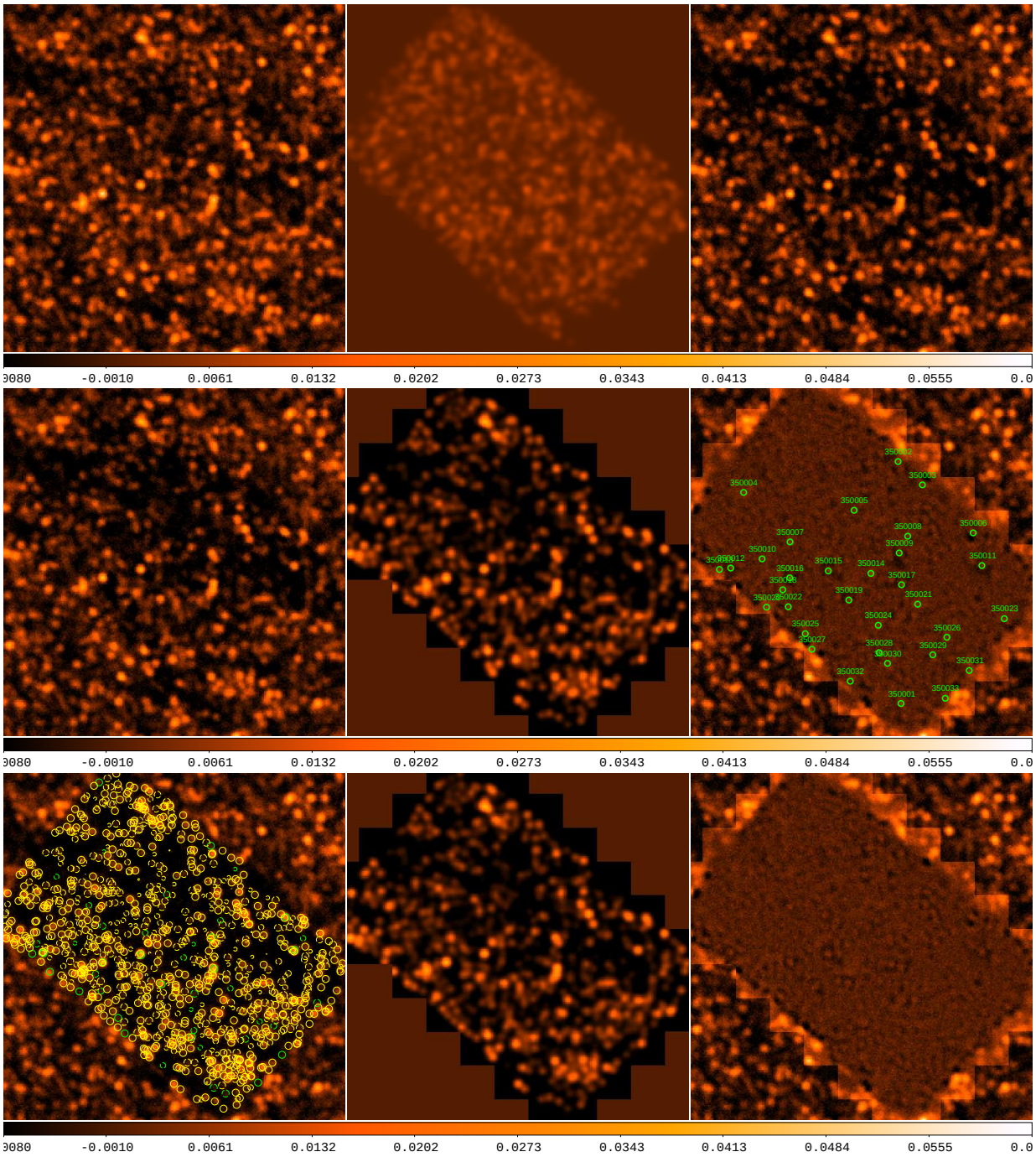

FIG. B39.—: Photometry image products at 350 μm. See descriptions in text.

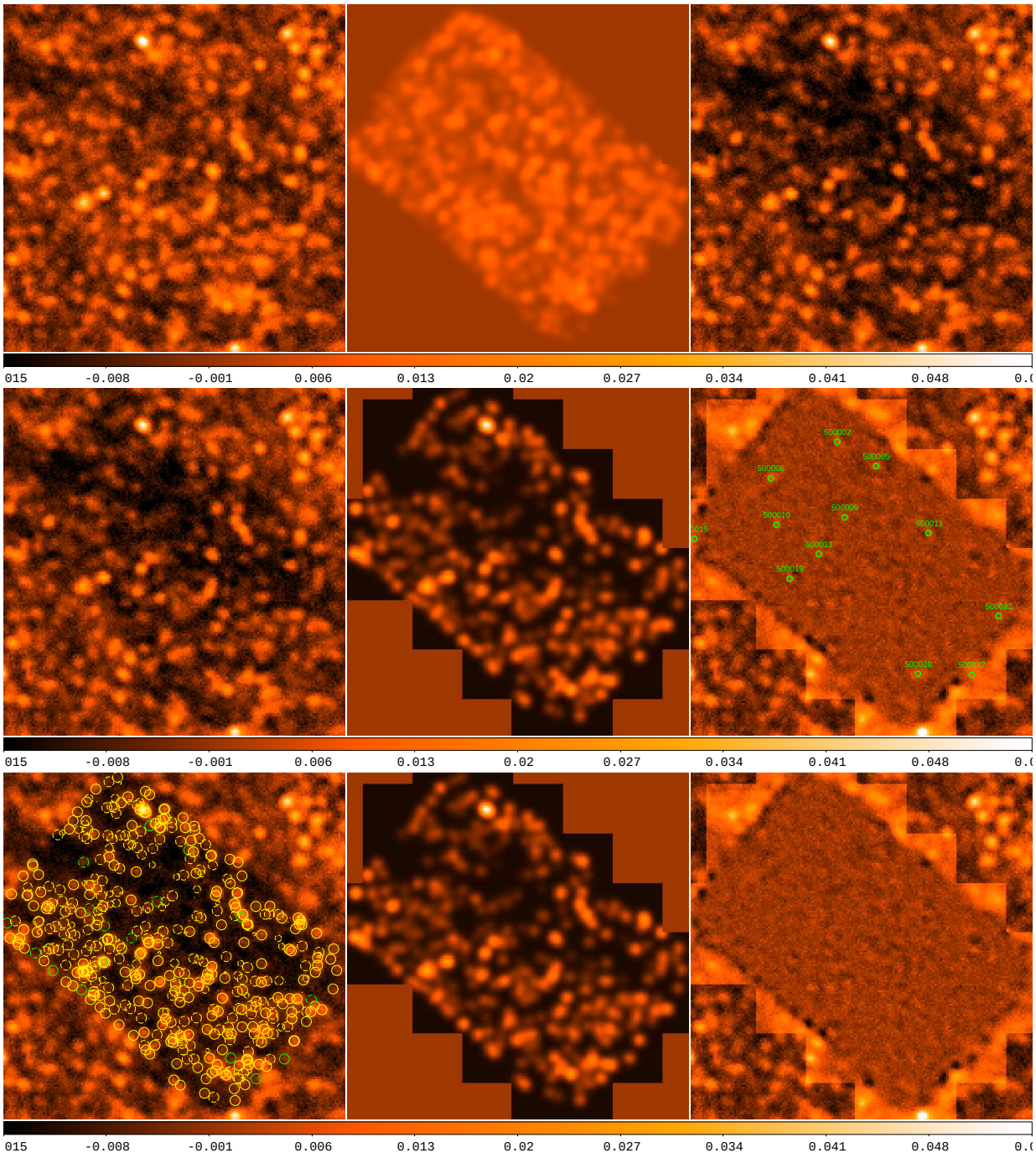

FIG. B40.—: Photometry image products at 500 μm. See descriptions in text.

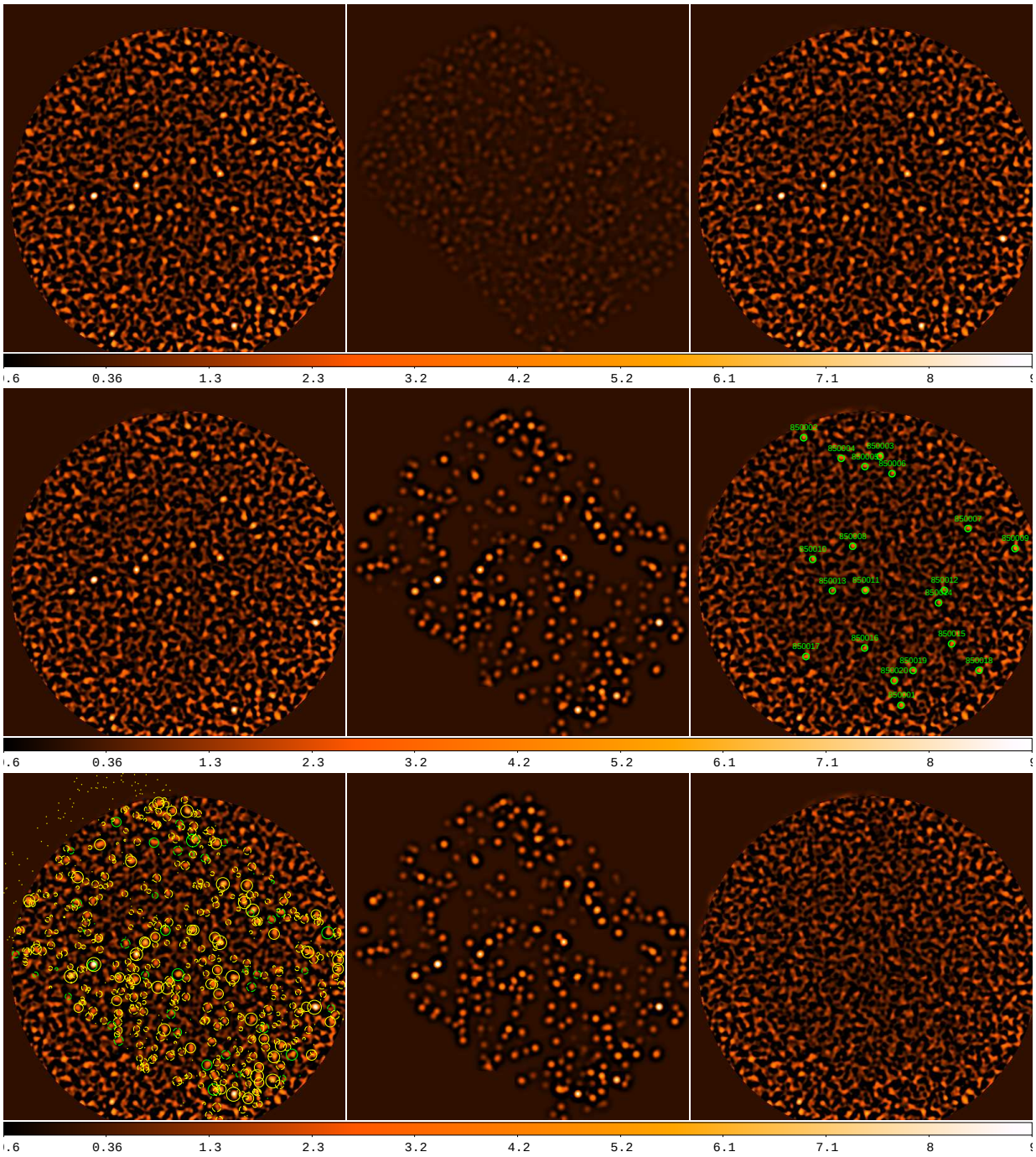

FIG. B41.—: Photometry image products at 850 μm. See descriptions in text.

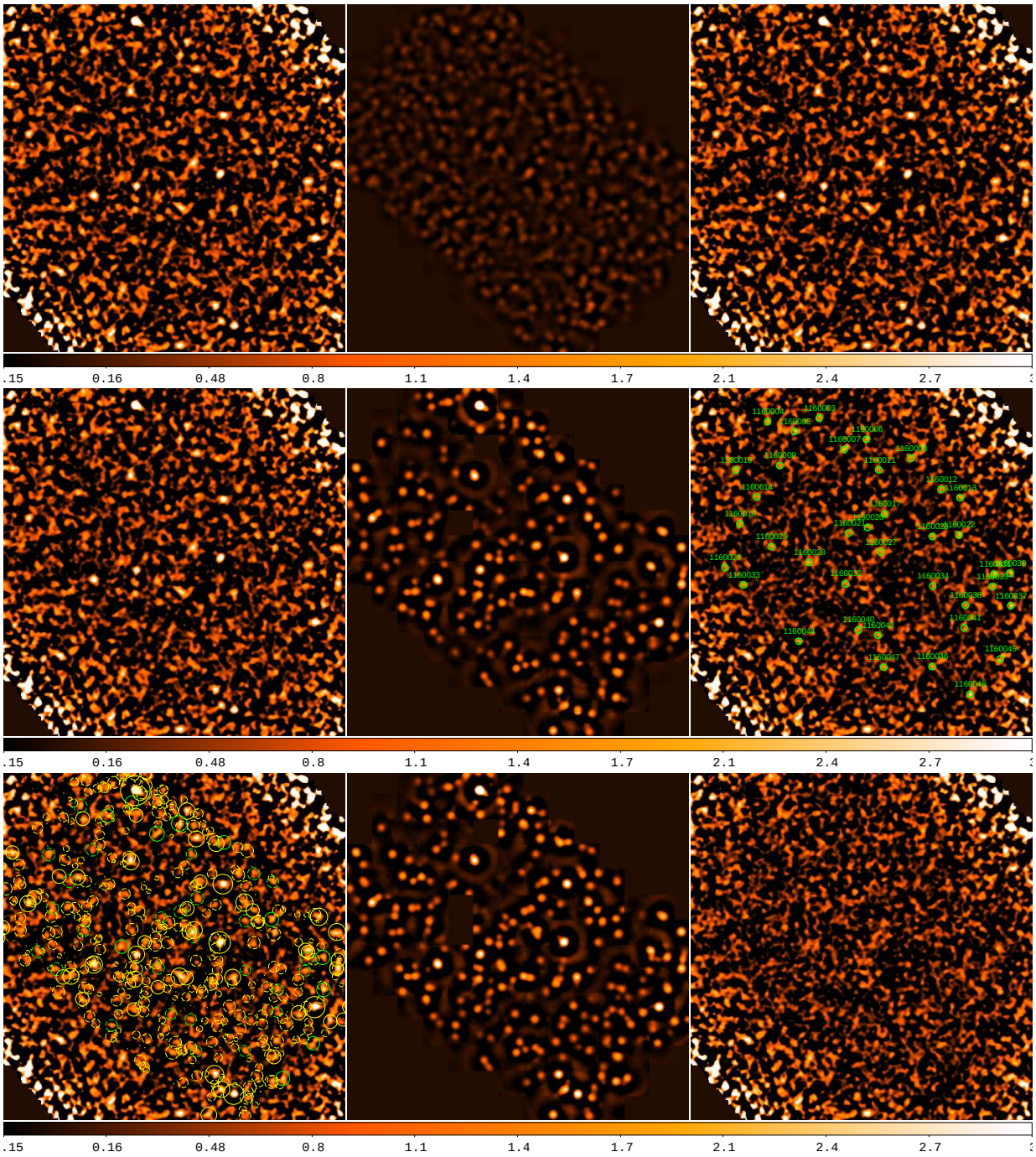

FIG. B42.—: Photometry image products at 1.16 mm. See descriptions in text.

SIMULATION CORRECTION ANALYSES

We present the analysis figures of our simulation-based correction recipes at each band here. For example, in Fig. C43, we bin simulation data points by three measurable parameters: the *galfit* flux uncertainty normalized by the local rms noise at the source position ($\sigma_{galfit}/\sigma_{\rm rms\,noise}$) in the first column, the residual flux within one PSF beam area on the residual image normalized also by the local rms noise ($f_{\rm residual}/\sigma_{\rm rms\,noise}$) in the second column, and the *crowdedness* parameter (see Section 5.1) in the third column. Bins are indicated by the dashed vertical lines in the first and second row images.

In the first row, we analyze the difference between the input and output flux of each simulated source ($S_{in}-S_{out}$), which reflects the flux bias of our photometry. We fit a 3-order polynomial function to the bin-averaged ($S_{in}-S_{out}$) on each parameter, shown as the red curve. Thus we can compute flux bias for real sources just according to each parameter value.

In the second row, we analyze the flux difference (($S_{in}-S_{out}$)) divided by the flux uncertainty (σ) of each simulated source (($S_{in}-S_{out}$)/σ). The scatter in each bin can be considered as the correction factor that needs to be applied to σ. Blue data points are uncorrected, while red ones are corrected. After correction, the scatter of $(S_{in}-S_{out})/\sigma$ in each bin is very close to 1.0, indicating that the corrected σ is statistically consistent with the scatter of $S_{in}-S_{out}$. We fit a 3-order polynomial function to the bin-averaged flux uncertainty correction factor on each parameter, which is shown as the red curve. The right axis indicates its value.

In the third row, we show the histogram of $(S_{in}-S_{out})/\sigma$ before and after the three-parameter corrections. Its shape, after correction (i.e. the red histogram), becomes well-behaved Gaussian distribution (i.e. symmetric and has a Gaussian width of 1.0), and is much better than the uncorrected one (i.e. the blue histogram). See also the main text in Section 5.3.

In the fourth row, we show the histogram of flux, and in the fifth row we show the histogram of flux uncertainty. In each panel, the blue one is before correction and the red one is after correction. From left to right, the panels are in the same three-parameter order. Generally the flux changes are very small, while the flux uncertainties are largely correction from the galfit-given values.

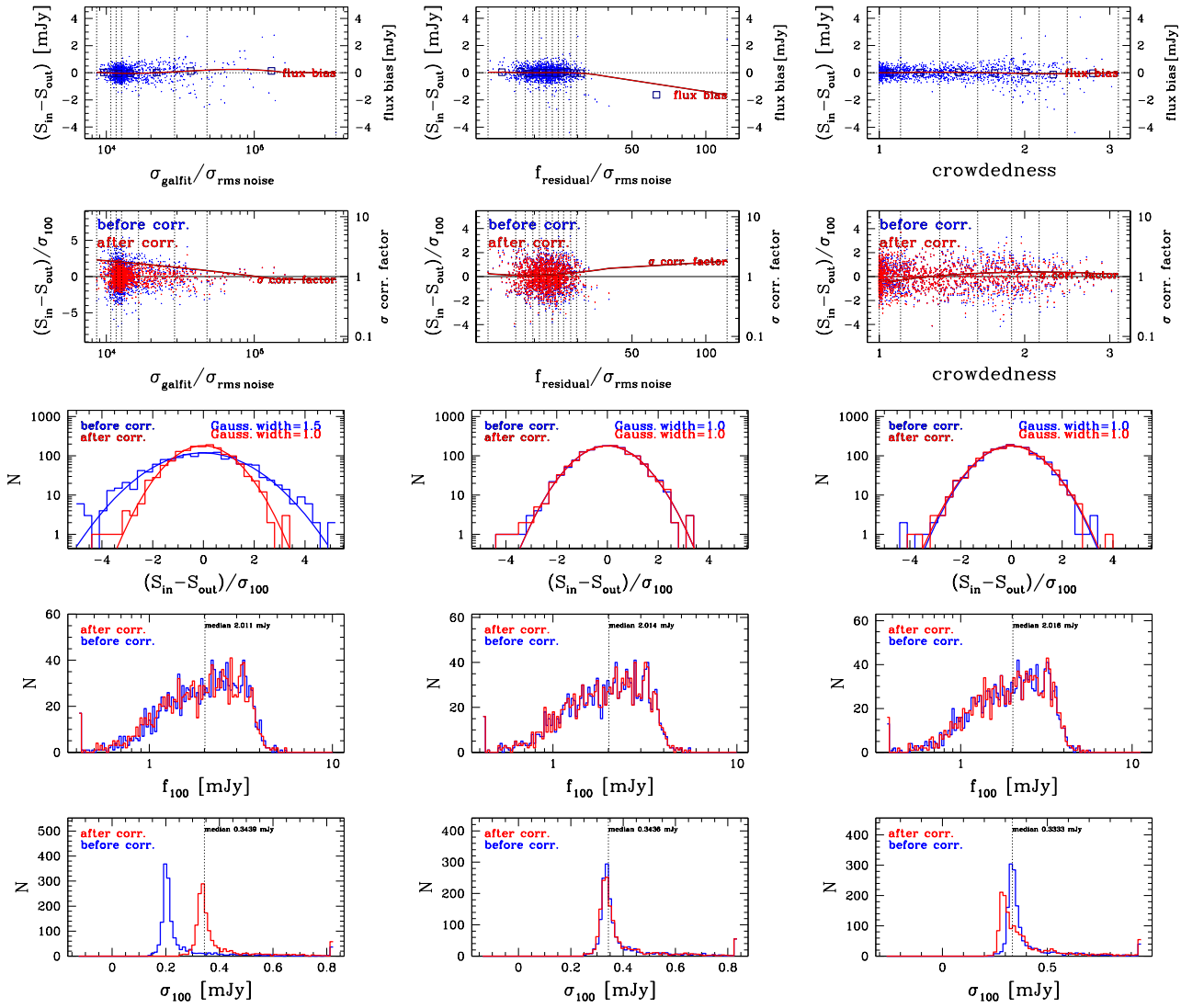

FIG. C43.—: Simulation correction analyses at 100 μm. See descriptions in text.

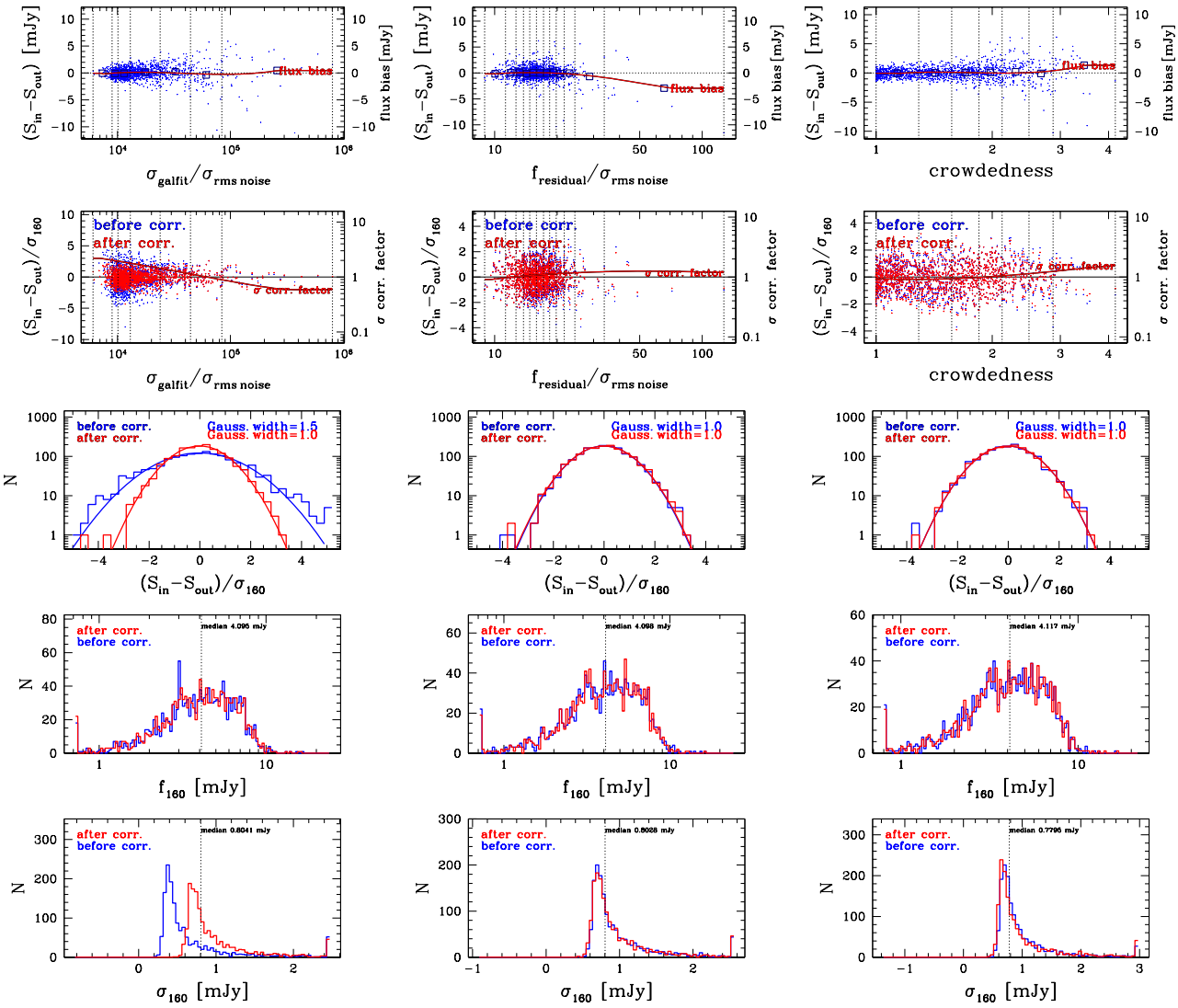

FIG. C44.—: Simulation correction analyses at 160 μm. See descriptions in text.

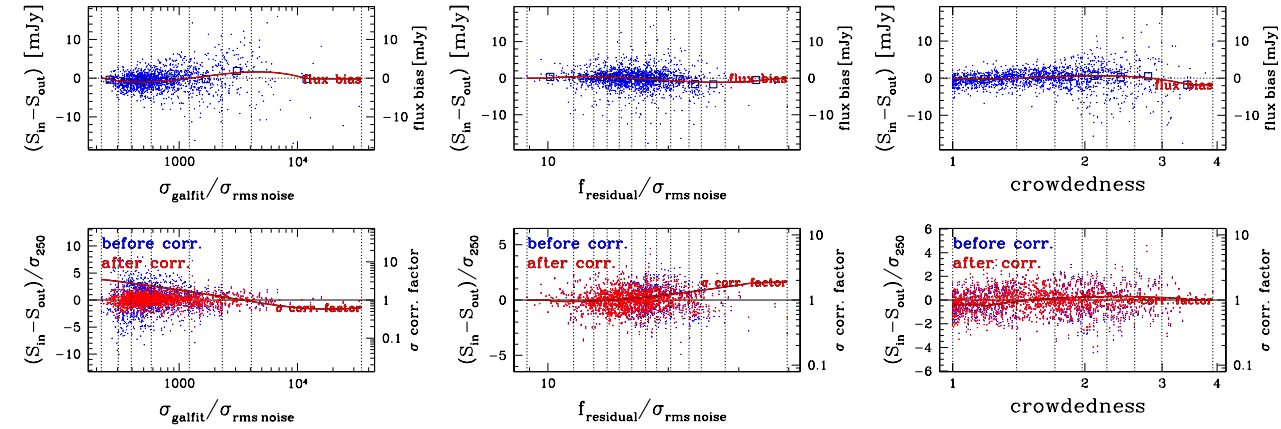

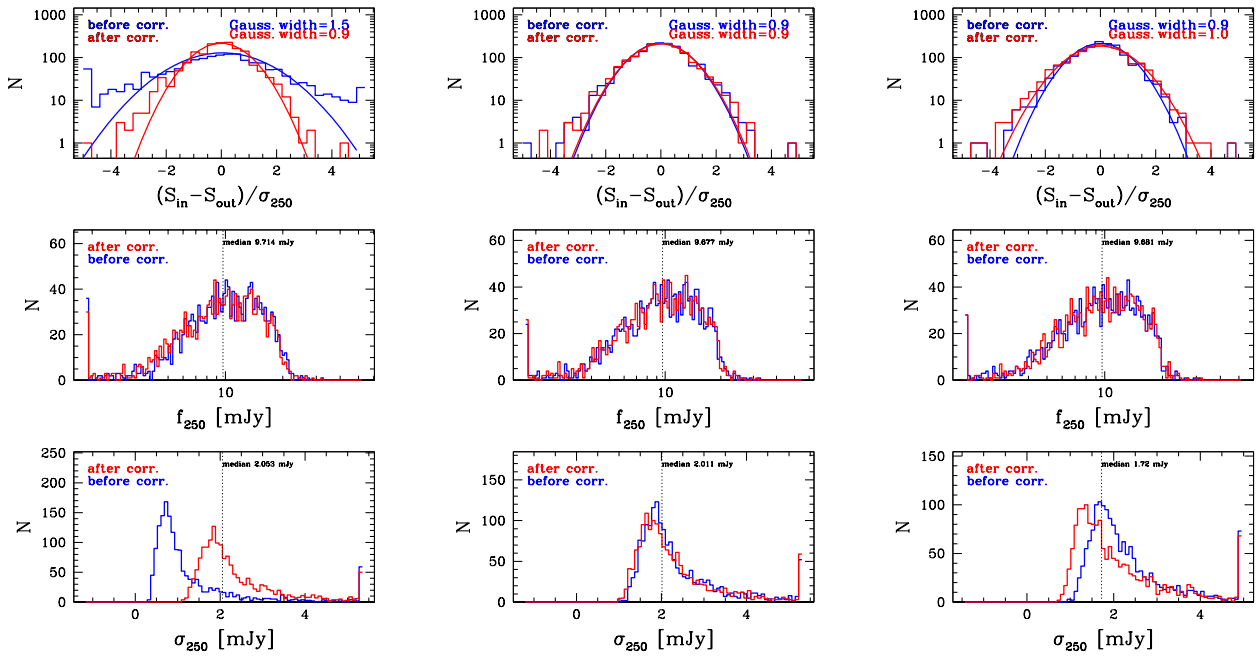

FIG. C45.—: Simulation correction analyses at 250 μm. See descriptions in text.

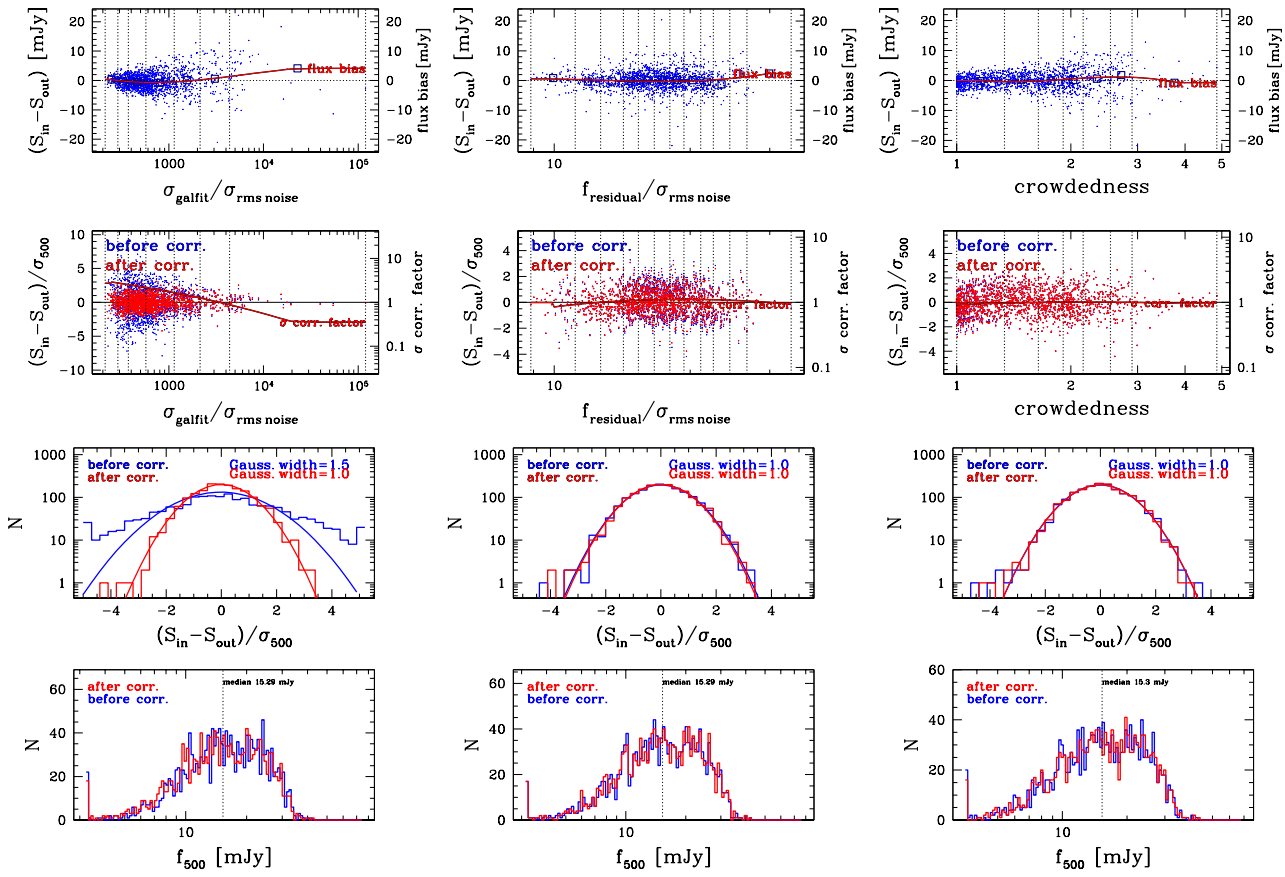

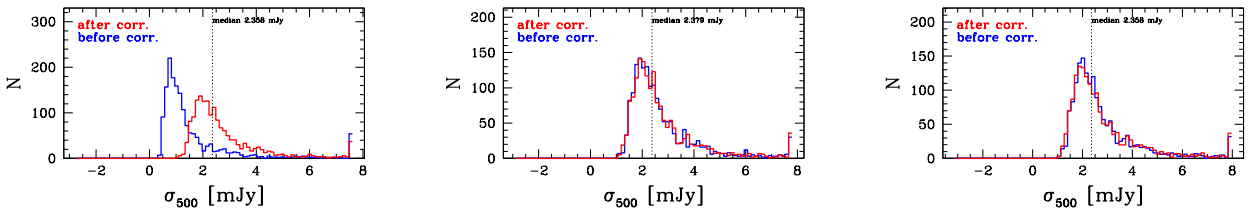

FIG. C46.—: Simulation correction analyses at 500 μm. See descriptions in text.

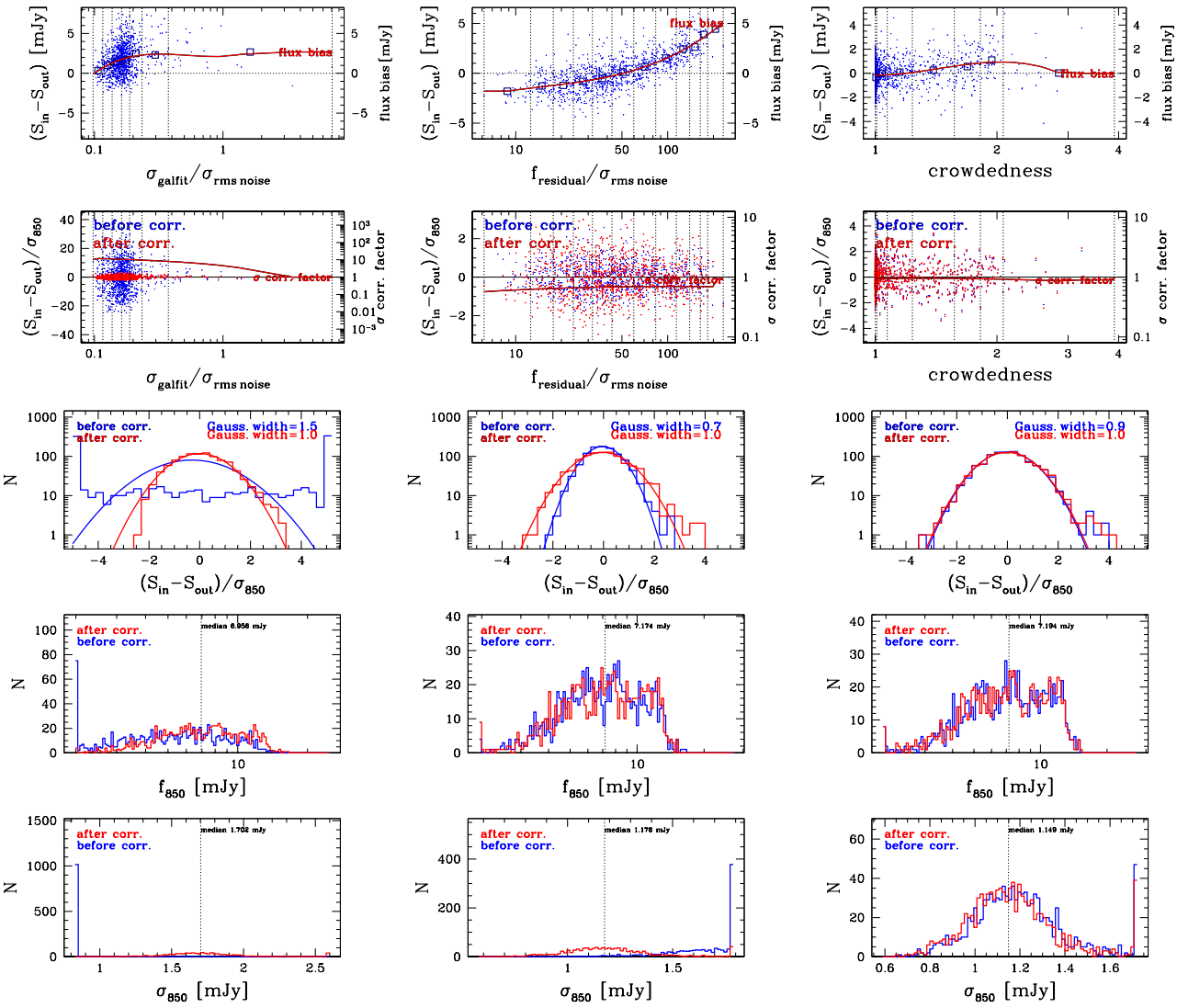

FIG. C47.—: Simulation correction analyses at 850 μm. See descriptions in text.

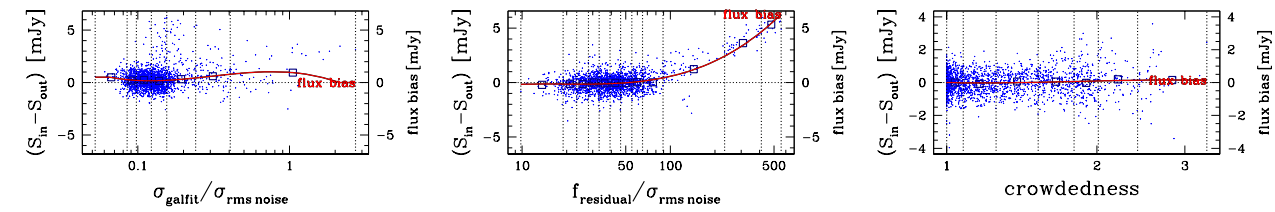

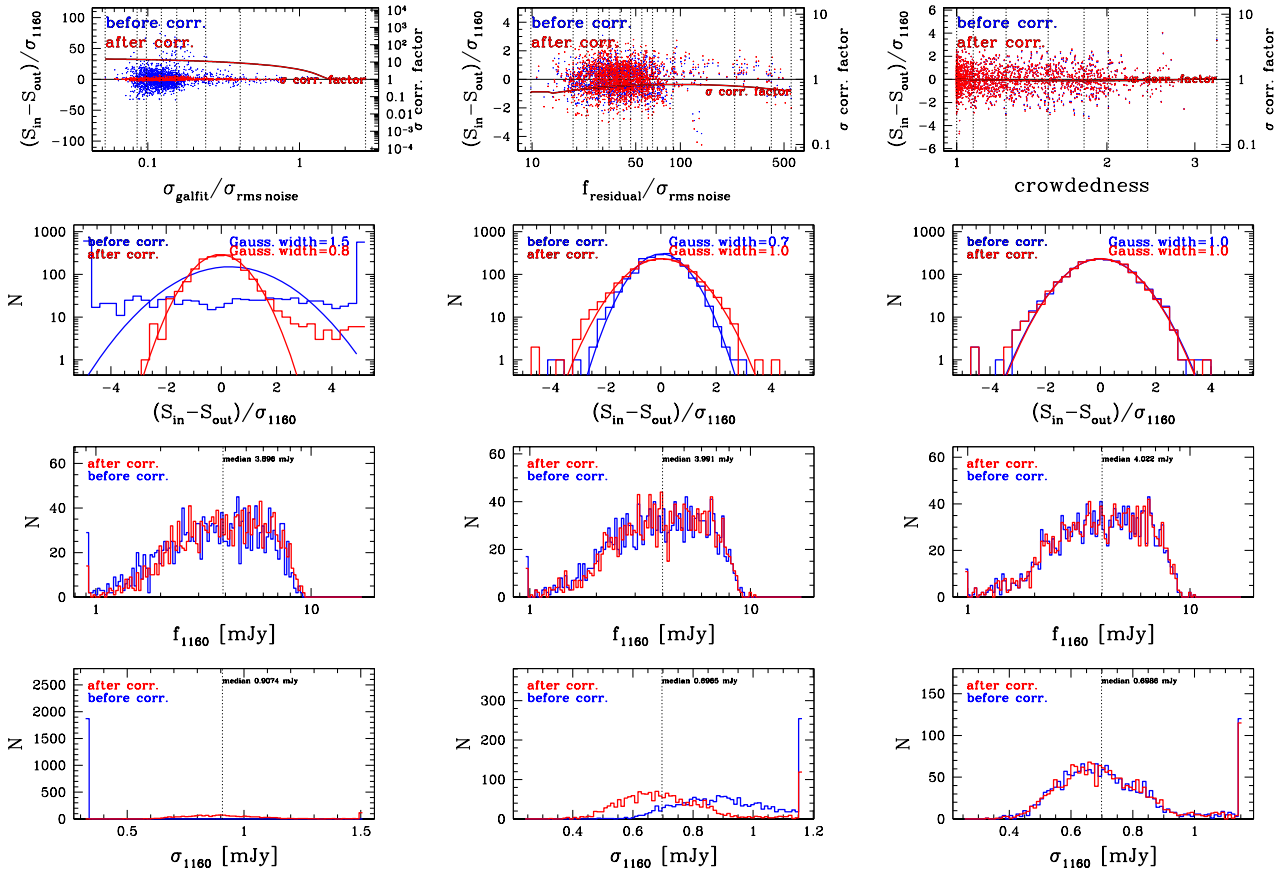

FIG. C48.—: Simulation correction analyses at 1.16 mm. See descriptions in text.

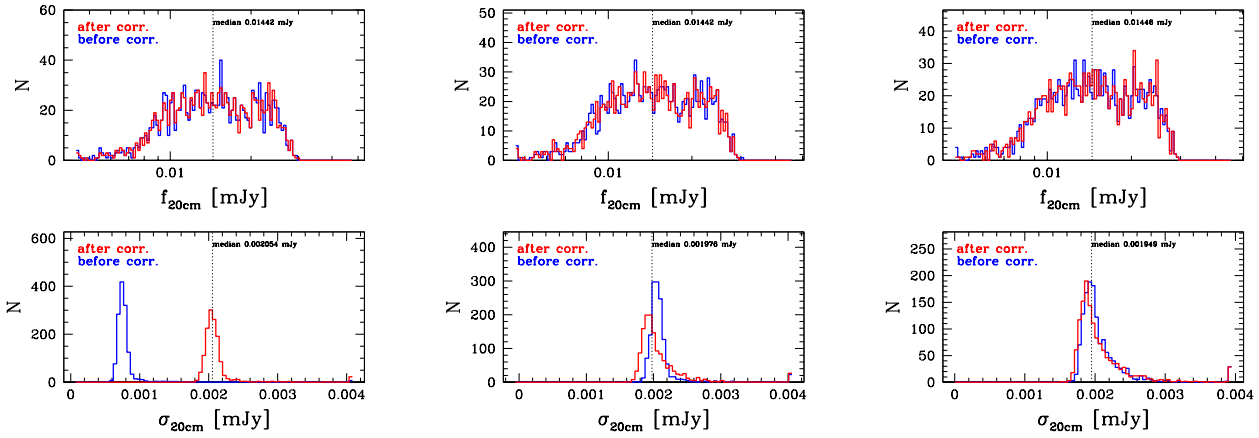

FIG. C49.—: Simulation correction analyses at 20 cm. See descriptions in text.

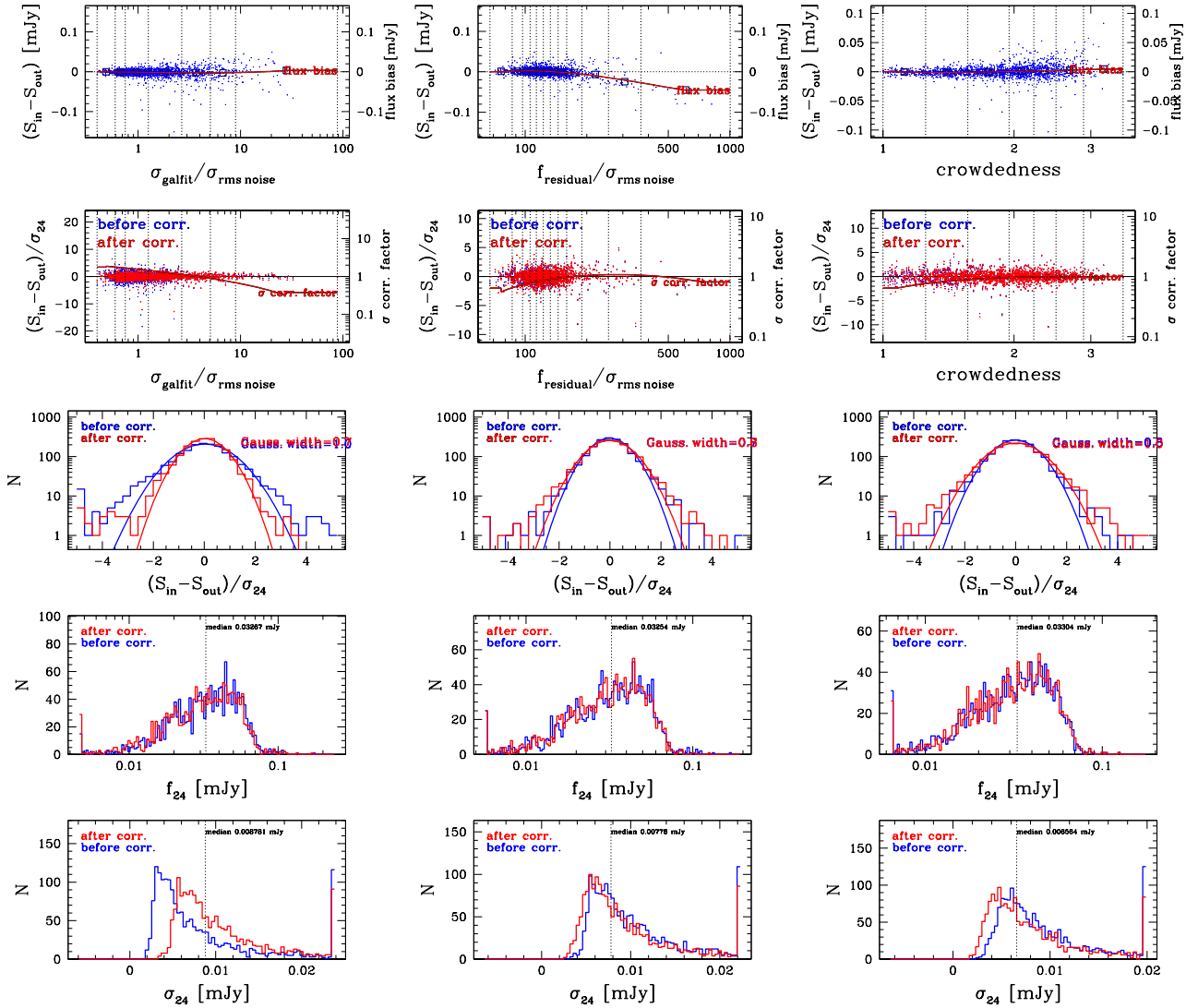

FIG. C50.—: Simulation correction analyses at 24 μm. See descriptions in text.

THE COSMIC SFR DENSITY COMPLETENESS ESTIMATION USING SMF-CONVERTED SFR HISTOGRAMS

In this work, due to the high and non-uniform incompleteness of our FIR+mm sample at all redshifts, we do not use the method of fitting Schechter functions to derive IR luminosity function or SFR function, but use a new method of fitting empirical SMFs to estimate the completeness of our FIR+mm sample to the cosmic SFR density. We compute the SMF-converted SFR histograms as described in Section 8.2, then fit the normalization of SMF-converted SFR histograms to the observed SFR histograms (we fit only the massive end where the stellar mass histogram has a $> 50\%$ completeness in number). The re-normalized SMF-converted SFR histograms are shown in Fig. D51.

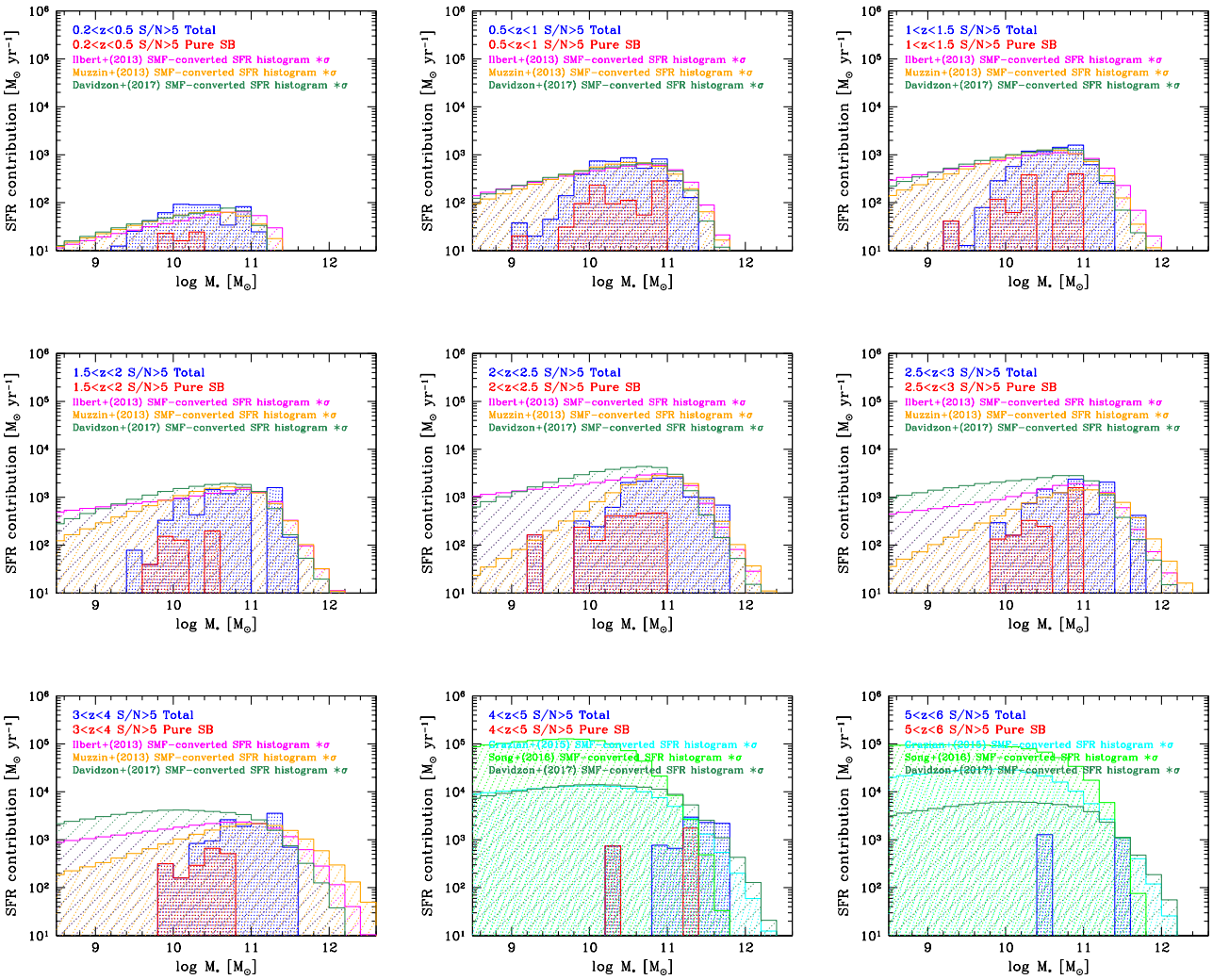

FIG. D51.—: The fitted SMF-converted SFR histograms which are used to estimate the completeness of our sample to the cosmic SFR density (Fig. 27). See text in Section 8.6.

REFERENCES

Abramson, L. E., Gladders, M. D., Dressler, A., et al. 2016, ApJ, 832, 7
Ashby, M. L. N., Willner, S. P., Fazio, G. G., et al. 2013, ApJ, 769, 80
—. 2015, ApJS, 218, 33
Avni, Y. 1976, ApJ, 210, 642
Avni, Y., Soltan, A., Tananbaum, H., & Zamorani, G. 1980, ApJ, 238, 800
Barger, A. J., Cowie, L. L., Brandt, W. N., et al. 2002, AJ, 124, 1839
Barger, A. J., Cowie, L. L., & Wang, W.-H. 2008, ApJ, 689, 687
Bertin, E., & Arnouts, S. 1996, A&AS, 117, 393
Béthermin, M., Dole, H., Beelen, A., & Aussel, H. 2010a, A&A, 512, A78
Béthermin, M., Dole, H., Cousin, M., & Bavouzet, N. 2010b, A&A, 516, A43
Béthermin, M., Le Floc'h, E., Ilbert, O., et al. 2012, A&A, 542, A58
Béthermin, M., Daddi, E., Magdis, G., et al. 2015, A&A, 573, A113
Bloomfield, J. K., Face, S. H. P., Guth, A. H., et al. 2016, ArXiv e-prints, arXiv:1612.03890
Bourne, N., Dunlop, J. S., Merlin, E., et al. 2017, MNRAS, arXiv:1607.04283
Bouwens, R. J., Illingworth, G. D., Oesch, P. A., et al. 2012, ApJ, 754, 83
Bruzual, G., & Charlot, S. 2003, MNRAS, 344, 1000
Casey, C. M., Berta, S., Béthermin, M., et al. 2012a, ApJ, 761, 140
—. 2012b, ApJ, 761, 140
Chabrier, G. 2003, PASP, 115, 763
Chapin, E. L., Pope, A., Scott, D., et al. 2009, MNRAS, 398, 1793
Ciesla, L., Boquien, M., Boselli, A., et al. 2014, A&A, 565, A128
Cohen, J. G., Hogg, D. W., Blandford, R., et al. 2000, ApJ, 538, 29
Condon, J. J. 1992, ARA&A, 30, 575
Conselice, C. J. 2014, ARA&A, 52, 291
Cowie, L. L., Barger, A. J., Hsu, L.-Y., et al. 2017, ArXiv e-prints, arXiv:1702.03002
Daddi, E., Dickinson, M., Morrison, G., et al. 2007, ApJ, 670, 156
Daddi, E., Dannerbauer, H., Stern, D., et al. 2009, ApJ, 694, 1517
Daddi, E., Elbaz, D., Walter, F., et al. 2010, ApJ, 714, L118
Davidzon, I., Ilbert, O., Laigle, C., et al. 2017, ArXiv e-prints, arXiv:1701.02734
Dickinson, M., Stern, D., Giavalisco, M., et al. 2004, ApJ, 600, L99
Dole, H., Lagache, G., & Puget, J.-L. 2003, ApJ, 585, 617
Draine, B. T. 2003, ARA&A, 41, 241
Draine, B. T., & Li, A. 2007, ApJ, 657, 810
Draine, B. T., Dale, D. A., Bendo, G., et al. 2007, ApJ, 663, 866
Dunlop, J. S., McLure, R. J., Biggs, A. D., et al. 2017, MNRAS, 466, 861
Elbaz, D., Daddi, E., Le Borgne, D., et al. 2007, A&A, 468, 33
Elbaz, D., Dickinson, M., Hwang, H. S., et al. 2011, A&A, 533, A119
—. 2013, VizieR Online Data Catalog, 353
Fazio, G. G., Hora, J. L., Allen, L. E., et al. 2004, ApJS, 154, 10
Frayer, D. T., Huynh, M. T., Chary, R., et al. 2006, ApJ, 647, L9
Frayer, D. T., Sanders, D. B., Surace, J. A., et al. 2009, AJ, 138, 1261
Gail, H.-P., Zhukovska, S. V., Hoppe, P., & Trieloff, M. 2009, ApJ, 698, 1136
Geach, J. E., Dunlop, J. S., Halpern, M., et al. 2017, MNRAS, 465, 1789
Giavalisco, M., Dickinson, M., Ferguson, H. C., et al. 2004, ApJ, 600, L103
Gladders, M. D., Oemler, A., Dressler, A., et al. 2013, ApJ, 770, 64
Grazian, A., Fontana, A., Santini, P., et al. 2015, A&A, 575, A96
Greve, T. R., Pope, A., Scott, D., et al. 2008, MNRAS, 389, 1489
Griffin, M. J., Abergel, A., Abreu, A., et al. 2010, A&A, 518, L3
Gruppioni, C., Pozzi, F., Rodighiero, G., et al. 2013, MNRAS, 432, 23
Helou, G., Soifer, B. T., & Rowan-Robinson, M. 1985, ApJ, 298, L7
Hurley, P. D., Oliver, S., Betancourt, M., et al. 2017, MNRAS, 464, 885
Ilbert, O., McCracken, H. J., Le Fèvre, O., et al. 2013, A&A, 556, A55
Ivison, R. J., Magnelli, B., Ibar, E., et al. 2010, A&A, 518, L31
Kajisawa, M., Ichikawa, T., Tanaka, I., et al. 2011, PASJ, 63, 379
Karim, A., Schinnerer, E., Martínez-Sansigre, A., et al. 2011, ApJ, 730, 61
Karim, A., Swinbank, A. M., Hodge, J. A., et al. 2013, MNRAS, 432, 2
Kellermann, K. I., & Owen, F. N. 1988, Radio galaxies and quasars, ed. K. I. Kellermann & G. L. Verschuur, 563–602
Kimball, A. E., & Ivezić, Ž. 2008, AJ, 136, 684
Kriek, M., Shapley, A. E., Reddy, N. A., et al. 2015, ApJS, 218, 15
Kroupa, P. 2002, Science, 295, 82
Lampton, M., Margon, B., & Bowyer, S. 1976, ApJ, 208, 177
Le Floc'h, E., Papovich, C., Dole, H., et al. 2005, ApJ, 632, 169
Le Floc'h, E., Aussel, H., Ilbert, O., et al. 2009, ApJ, 703, 222
Lee, N., Sanders, D. B., Casey, C. M., et al. 2013, ApJ, 778, 131
Madau, P., & Dickinson, M. 2014, ARA&A, 52, 415
Magdis, G. E., Elbaz, D., Dickinson, M., et al. 2011, A&A, 534, A15
Magdis, G. E., Daddi, E., Béthermin, M., et al. 2012, ApJ, 760, 6
Magnelli, B., Elbaz, D., Chary, R. R., et al. 2009, A&A, 496, 57
—. 2011, A&A, 528, A35
Magnelli, B., Popesso, P., Berta, S., et al. 2013, A&A, 553, A132
Magnelli, B., Ivison, R. J., Lutz, D., et al. 2015, A&A, 573, A45
Marvil, J., Owen, F., & Eilek, J. 2015, AJ, 149, 32
Morrison, G. E., Owen, F. N., Dickinson, M., Ivison, R. J., & Ibar, E. 2010, ApJS, 188, 178
Mullaney, J. R., Alexander, D. M., Goulding, A. D., & Hickox, R. C. 2011, MNRAS, 414, 1082
Muzzin, A., Marchesini, D., Stefanon, M., et al. 2013, ApJ, 777, 18
Noeske, K. G., Weiner, B. J., Faber, S. M., et al. 2007, ApJ, 660, L43
Oliver, S. J., Bock, J., Altieri, B., et al. 2012, MNRAS, 424, 1614
Pannella, M., Carilli, C. L., Daddi, E., et al. 2009, ApJ, 698, L116
Pannella, M., Elbaz, D., Daddi, E., et al. 2015, ApJ, 807, 141
Peng, C. Y., Ho, L. C., Impey, C. D., & Rix, H.-W. 2002, AJ, 124, 266
—. 2010, AJ, 139, 2097
Penner, K., Pope, A., Chapin, E. L., et al. 2011, MNRAS, 410, 2749
Perera, T. A., Chapin, E. L., Austermann, J. E., et al. 2008, MNRAS, 391, 1227
Pilbratt, G. L., Riedinger, J. R., Passvogel, T., et al. 2010, A&A, 518, L1
Poglitsch, A., Waelkens, C., Geis, N., et al. 2010, A&A, 518, L2
Pope, A., Scott, D., Dickinson, M., et al. 2006, MNRAS, 370, 1185
Popesso, P., Magnelli, B., Buttiglione, S., et al. 2012, ArXiv e-prints, arXiv:1211.4257
Pozzetti, L., Cimatti, A., Zamorani, G., et al. 2003, A&A, 402, 837
Press, W. H., Teukolsky, S. A., Vetterling, W. T., & Flannery, B. P. 1992, Numerical recipes in C. The art of scientific computing
Reddy, N. A., Steidel, C. C., Erb, D. K., Shapley, A. E., & Pettini, M. 2006, ApJ, 653, 1004
Rieke, G. H., Young, E. T., Engelbracht, C. W., et al. 2004, ApJS, 154, 25
Rodighiero, G., Cimatti, A., Gruppioni, C., et al. 2010, A&A, 518, L25
Rodighiero, G., Daddi, E., Baronchelli, I., et al. 2011, ApJ, 739, L40
Roseboom, I. G., Oliver, S. J., Kunz, M., et al. 2010, MNRAS, 409, 48
Roseboom, I. G., Ivison, R. J., Greve, T. R., et al. 2012, MNRAS, 419, 2758
Rowan-Robinson, M., Oliver, S., Wang, L., et al. 2016, MNRAS, 461, 1100
Safarzadeh, M., Ferguson, H. C., Lu, Y., Inami, H., & Somerville, R. S. 2015, ApJ, 798, 91
Salpeter, E. E. 1955, ApJ, 121, 161
Sargent, M. T., Schinnerer, E., Murphy, E., et al. 2010, ApJ, 714, L190
Sargent, M. T., Daddi, E., Béthermin, M., et al. 2014, ApJ, 793, 19
Schmidt, M. 1968, ApJ, 151, 393
Schreiber, C., Pannella, M., Elbaz, D., et al. 2015, A&A, 575, A74
Scudder, J. M., Oliver, S., Hurley, P. D., et al. 2016, MNRAS, 460, 1119
Shu, X. W., Elbaz, D., Bourne, N., et al. 2016, ApJS, 222, 4
Skelton, R. E., Whitaker, K. E., Momcheva, I. G., et al. 2014, ApJS, 214, 24
Song, M., Finkelstein, S. L., Ashby, M. L. N., et al. 2016, ApJ, 825, 5
Stark, D. P., Ellis, R. S., Bunker, A., et al. 2009, ApJ, 697, 1493
Tan, Q., Daddi, E., Magdis, G., et al. 2014, A&A, 569, A98
Teplitz, H. I., Chary, R., Elbaz, D., et al. 2011, AJ, 141, 1
Vanzella, E., Giavalisco, M., Dickinson, M., et al. 2009, ApJ, 695, 1163
Walter, F., Decarli, R., Carilli, C., et al. 2012, Nature, 486, 233
Wang, T., Elbaz, D., Schreiber, C., et al. 2016, ApJ, 816, 84
Werner, M. W., Roellig, T. L., Low, F. J., et al. 2004, ApJS, 154, 1
Wirth, G. D., Willmer, C. N. A., Amico, P., et al. 2004, AJ, 127, 3121
Wirth, G. D., Trump, J. R., Barro, G., et al. 2015, AJ, 150, 153
Yan, H., Stefanon, M., Ma, Z., et al. 2014, ApJS, 213, 2
Zhukovska, S., & Henning, T. 2013, A&A, 555, A99